Numerical investigation of multiphase Darcy-Forchheimer flow and contaminant transport during SO_2 co-injection with CO_2 in deep saline aquifers

A Thesis
Presented to
The Academic Faculty

by

Andi Zhang

In Partial Fulfillment
Of the Requirements for the Degree
Doctor of Philosophy in Environmental Engineering
School of Civil and Environmental Engineering

Georgia Institute of Technology
August 2013

Numerical investigation of multiphase Darcy-Forchheimer flow and contaminant transport during SO_2 co-injection with CO_2 in deep saline aquifers

Approved by:

Dr. Mustafa M. Aral, Advisor
School of Civil and Environmental Engineering
Georgia Institute of Technology

Dr. Jiabao Guan
School of Civil and Environmental Engineering
Georgia Institute of Technology

Dr. Marc Stieglitz
School of Civil and Environmental Engineering
Georgia Institute of Technology

Dr. Turgay Uzer
School of Physics
Georgia Institute of Technology

Dr. Jian Luo
School of Civil and Environmental Engineering
Georgia Institute of Technology

Date Approved: June 6, 2013

To my family for their endless love and unconditional support

ACKNOWLEDGMENTS

First and foremost, I would like to express my sincere appreciation and gratitude to Dr. Mustafa M. Aral, my advisor at Multimedia Environmental Simulations Laboratory (MESL), for his continuous support, invaluable guidance and encouragement. I greatly appreciate all his contributions of time, ideas, patience, and funding to make my Ph.D. study possible. During the past several years I have learned a lot from Dr. Aral, which is much more than doing research and will benefit me a lot in the future.

I am deeply indebted to my committee member Dr. Jiabao Guan for his inspiring ideas and kind encouragement. Special thanks should also go to my committee members Dr. Marc Stieglitz, Dr. Jian Luo, and Dr. Turgay Uzer for their time and effort in reviewing this work and for their valuable comments and insightful suggestions.

I would like to express my sincere appreciation to the MESL members Dr. Wonyong Jang, Dr. Scott Rogers, Dr. Recep Kaya Goktas, Dr. Ilker T. Telci, Mr. Biao Chang, and Mr. William Morgan for their professional support, friendship and valuable comments and suggestions during MESL seminars.

On a more personal level, I would like to give my deepest gratitude to my parents Xinxing and Meiying, my parents-in-law Jinhua and Qiuhong, my wife Wendy, my sister Xiumei and my brother Zhigang. Without their endless love and unconditional support, I could not have persevered to finish my doctoral work by overcoming many challenges during the journey.

TABLE OF CONTENTS

LIST OF TABLES

LIST OF FIGURES

SUMMARY

The global climate change is generally believed to occur as a result of the anthropogenic emission of greenhouse gases (GHG). Of all the strategies to reduce carbon emissions, storage of anthropogenic carbon dioxide (CO_2) within geologic reservoirs is an immediately available option for mitigating the global environmental impact of CO_2 by removing large amounts of the gas from the atmosphere. In this thesis, first a generalized Darcy-Forchheimer multiphase flow model is developed and used to investigate the transition behavior between Darcy and Forchheimer flows during CO_2 injection into deep saline aquifers. The second part of this thesis focuses on the investigation of the kinetic mass transfer of sulfur dioxide (SO_2) and CO_2 from CO_2 stream to the saline and the resultant brine acidification and induced porosity and permeability changes due to SO_2 co-injection with CO_2 in deep saline aquifers by using numerical models for multiphase flow, contaminant transport and geochemistry with the coupling between the changes of porosity and permeability and the multiphase fluid flow.

In the first part of this thesis, a convenient definition of the Forchheimer number is proposed to derive a generalized Darcy-Forchheimer model for multiphase flows. The generalized mathematical model is then discretized and solved using control volume finite difference method to simulate two-phase inertial immiscible and incompressible flow in non-deformable homogeneous porous media. The numerical tool is validated by comparing the results to those obtained using a semi-analytical solution to the Buckley-Leverett problem with Forchheimer effects. In addition, this thesis proposes a new method to determine the critical Forchheimer number for the transition between Darcy flow and Forchheimer flow for both single and multiple phases and obtains the critical values for both water and CO_2 by using experimental data in the literature. The critical Forchheimer numbers and the multiphase flow model are then used to analyze the application problem involving the injection of CO_2 into deep saline aquifers. The results show that the Forchheimer effect, compounded by the buoyancy effect caused by the density difference between the injected CO_2 and the saline, would result in higher

displacement efficiency with a magnitude of more than 50% in the Forchheimer regime than that for Darcy flow, which could increase the storage capacity for the same injection rate and volume of a site. Another merit for the incorporation of Forchheimer effect is that more CO_2 would be accumulated in the lower half of the domain and lower pressure would be imposed on the lower boundary of the cap-rock due to the stronger vertical resistance as a result of the combination of the buoyancy effects and Forchheimer effects. However, as a price for the advantages mentioned above, the injection pressure required in Forchheimer flow would be higher than that for Darcy flow, which would expose the formation near the injecting area to a higher pressure and might increase the risk of fracturing the domain and CO_2 leakage into the atmosphere.

In the second part of the study, we first develop a multiphase flow, contaminant transport and geochemical model which incorporates the kinetic mass transfer of SO_2 and CO_2 into deep saline aquifers and the coupling between the fluid flow and the induced porosity and permeability changes caused by the brine acidification. Then the model is used to analyze the brine acidification and the resultant mineral dissolution and precipitation which would further cause the changes in porosity and permeability due to SO_2 co-injection with CO_2 into deep saline aquifers. The results show that the co-injection of SO_2 with CO_2 would lead to a substantially acid zone near the injecting well and it is important to include the kinetic dissolution of SO_2 from the CO_2 stream to the water phase into the simulation models because the accumulated difference in the saline acidification and the induced porosity and permeability changes between kinetic and equilibrium dissolution of SO_2 is considerable and can not be neglected.

Chapter 1 Introduction

1.1 Background

1.1.1 Darcy-Forchheimer flow

Fluid flow through porous media is an important aspect of many applications in petroleum engineering, environmental hydrogeology and more recently in applications such as Carbon Dioxide (CO_2) sequestration and storage in deep saline aquifers. For the successful design and operation of these projects, it is essential to accurately describe the behavior of fluid flow through porous media. In general this behavior is commonly characterized by Darcy's law. According to Darcy's law, the pressure gradient is linearly proportional to the fluid velocity in the porous media.

In certain applications deviations of fluid flow behavior from Darcy's law have long been observed (Chilton et al., 1931; Green et al., 1951; Ergun, 1952; Tek et al., 1962; Scheidegger, 1972; Katz and Lee, 1990; Andrade et al., 1999; Zeng and Grigg, 2006). To describe these cases various terms, such as non-Darcy flow, turbulent flow, inertial flow, high velocity flow, nonlinear flow, etc., have been used (Firoozabadi and Katz, 1979). In the literature we see several attempts to redefine the Darcy equation for these cases. For example, Forchheimer (1901) added a second order velocity term to represent the microscopic inertial effect, and modified the Darcy equation into the Forchheimer equation. The so called Forchheimer flow is widely considered to describe the inertial effects due to additional friction observed for high velocity flow. Theoretical, field and experimental studies performed on non-Darcy flows in porous media have focused mostly on single-phase-flow conditions in the oil and gas industry (Swift and Kiel, 1962; Tek et al., 1962; Lee et al., 1987). More recently, several studies are reported in the literature that extend the Forchheimer equation to multiphase flow and provide the governing equations for correlating non-Darcy flow coefficients under multiphase conditions (Evans et al., 1987; Evans and Evans, 1988; Liu et al., 1995; Wu, 2002; Ahmadi et al., 2010; Zhang and Xing, 2012). The Forchheimer flow condition commonly occurs in near-wellbore area due to high injection rates and thus high flow velocity. However, currently the Forchheimer effect has not been well accounted for in the

numerical simulation of multiphase flows, especially in the process of CO_2 storage in deep saline aquifers. Recently, Mijic and Laforce (2010) studied the salt precipitation during CO_2 injection for an inertial flow regime and concluded that it is necessary to include nonlinear flow behavior in near-wellbore area.

The transition between Darcy flow and Forchheimer flow is described in terms of two different criteria: (i) the use of the Reynolds number (Type-I) defined by Equation (1.1); and, (ii) the use of the Forchheimer number (Type-II) expressed as Equation (1.2),

$$\mathrm{Re} = \frac{\rho d v}{\mu} \tag{1.1}$$

$$f = \frac{\rho k \beta v}{\mu} \tag{1.2}$$

where d is the diameter of particles and β is the Forchheimer coefficient. The Type-I criterion has been applied mainly in columns of packed particles in which characteristic length, usually chosen as the representative particle diameter, is available, and the Type-II criterion has been used mainly in numerical models. A detailed review of the criteria used for the transition between Darcy flow and Forchheimer flow for single phase case can be found in Zeng and Grigg (2006). In a recent study on the transition between Darcy and Forchheimer flow for single phase case by Zhang et al. (2012), non-Darcy flow behavior is described using the Forchheimer equation, and the Forchheimer number is used to determine if the flow is of Darcy or Forchheimer. The results show that when Forchheimer flow in the near-well region is considered, both the fluid velocity and the wellbore pressure are much different than the Darcy flow velocity and pressure conditions. Except this study, to our knowledge, there are no other studies in the literature that incorporate the transition between Darcy flow and Forchheimer flow in applications especially for multiphase flows in two dimensional applications. Because of lack of detailed studies in this area, as well as the mathematical difficulty of handling highly nonlinear Forchheimer flow terms in multiphase flow equations, our understanding of Forchheimer flow behavior through porous media is currently very limited.

1.1.2 Effects of co-injected impurities on CO_2 geologic storage

Geological sequestration of carbon dioxide is emerging as a promising process to diminish, if not prevent, the further increasing levels of carbon dioxide in the atmosphere. Of all the candidate deep geologic formations which include aquifers in sedimentary formations, structural traps in depleted oil and gas fields and deep un-mineable coal seams, sequestration in deep saline aquifers is an especially appealing option due to the great abundance of injection sites, huge potential storage capacity and technical feasibility (Bruant et al., 2002; Bachu, 2008; Benson and Cole, 2008).

Since CO_2 originates from a variety of sources, such as coal-fired power plants, gas plants, refineries, steel and cement plants, the CO_2 stream contains various impurities, such as Nitrogen gas (N_2), dioxygen (O_2), argon (Ar), sulfur oxide (SO_x), nitrogen oxide (NO_x), hydrogen sulfide (H_2S), etc., in various concentrations. The co-injection of these impurities with CO_2 in geologic sequestration also has economic incentives. On one hand, the purity level of CO_2 stream comes with the cost of energy and money. As is pointed out in a research by Mckinsey & Company (2008), the costs of separation and compression of CO_2 from point sources constitute the largest part of the total cost of carbon capture and sequestration. This is partially due to the fact that CO_2 captured from a point source is never a pure stream. To increase the purity of the stream and decrease the level of impurities, it requires an exponential increase in the money and energy needed if the purity increases from lower levels to higher and higher levels. Permitting a less pure stream for injection would decrease the total cost, although the impurities in the stream might have negative impacts on the transport pipelines and long term storage in the deep saline aquifers. On the other hand, different industrial sectors spend billions of dollars on controlling the emissions of SO_x, NO_x and H_2S. For example, every year, the electric power industry, the largest point sources from which CO_2 will be captured, collectively spends more than $5 billion on permits for the right to emit SO_2 (USEPA, 2009). Therefore, it may be economically advantageous to co-inject SO_x, NO_x and H_2S with CO_2 into deep saline aquifers.

However, it is vitally necessary to investigate the potential effects of these impurities before impurities like SO_x, NO_x and H_2S can be safely disposed with CO_2. In general, the effects of impurities on (short- and long-term) geological storage can be categorized into

physical effect and chemical effect. The physical effect is related to the storage capacity reduction due to non-condensable impurities such as O_2, Ar, N_2 and H_2 which are less dense than CO_2 and hence take greater volumes. The chemical effect is about the induced porosity and permeability changes caused by the mineral dissolution and subsequent precipitation associate with the dissolution into and reaction with water of SO_2, H_2S and NO_x.

A primary issue concerning geologic CO_2 sequestration is the potential for brine acidification. Injection of pure CO_2 will result in the formation of carbonic acid and lead to brine acidification, which would bring about acid-catalyzed mineral dissolution and precipitation (Gunter and Perkins, 1993; Baines and Worden, 2004; Xu et al., 2004; Giammar et al., 2005; Li et al., 2006; Zerai et al., 2006; Gaus et al., 2008; Peters, 2009). These reactions will change the permeability and porosity and may endanger the formation integrity (Kaszuba et al., 2005). However, mineral dissolution may also cause pH buffering as was observed in the CO_2 injection into the Frio formation (Kharaka et al., 2006). If the buffering capacity provided by the formation mineralogy is insufficient, the acidified brine may degrade cements of nearby abandoned wells or weaken the integrity of the caprock, thereby enhancing the probability of CO_2 leakage to the surface (Gaus et al., 2005; Nordbotten et al., 2005; Carey et al., 2007; Duguid et al., 2007; Gherardi et al., 2007; Kutchko et al., 2007). The presence of impurities, such as SO_2 and H_2S, may lead to further brine acidification due to the formation of stronger acids. Both SO_2 and H_2S have been previously studied as co-injectants with CO_2 (Gunter et al., 2000; Knauss et al., 2005; Palandri and Kharaka, 2005; Xu et al., 2007). Knauss et al. (2005) predicted that co-injection of even a small amount of SO_2 (10^{-6} bar partial pressure) would result in a brine pH of unity and increased mineral dissolution due to the formation of sulfuric acid. Xu et al. (2007) provided extra evidence for extreme brine acidification due to co-injection of SO_2 by demonstrating that SO_2 co-injection would result in near-zero pH values within a radial distance exceeding 100 m from the point of injection.

However, these previous modeling studies (Knauss et. al, 2005; Xu et. al, 2007) of co-injection of SO_2 with CO_2 assume sustained phase equilibrium between all the supercritical CO_2 ($scCO_2$) and brine. Only the extreme case for no limitation on the contact of SO_2 with the brine was considered. The kinetic mass transfer of SO_2 and CO_2

into the water phase was ignored in almost all the current geochemical models which deal with the potential effects of impurities of $scCO_2$. This could result in overestimation of the actual acidity during CO_2 injection into deep saline aquifer and thus could produce inaccurate estimate of the induced changes in the porosity and permeability. Therefore there is a need to estimate the flux of SO_2 from the injected CO_2 to the bulk brine phase. Moreover, such kinetic mechanisms need to be integrated into numerical models. Only until recently did Ellis et al. (2010) acknowledge the importance of mass transfer limitations for SO_2 through two-phase boundary to the brine acidification and resultant mineral dissolution and precipitation. Based on their simplified model, they concluded that the magnitude, onset, and spatial extent of brine acidification may not be significant if the dissolution rate of the injected SO_2 was considered. However, the simplified geometry of their model and the neglecting of two-phase flows entail their model to be only valid after the injection period when CO_2 flow can be negligible. So far, in the modeling research on geologic CO_2 sequestration, there is no multiphase flow and transport model which incorporates the kinetic dissolution of SO_2 and CO_2. This could be attributed to the lack of kinetic data and the requirement of high performance computing.

Another important aspect during the multiphase flow and transport modeling research on geologic CO_2 sequestration is to incorporate the changes of porosity and permeability into the multiphase flow model. However, previously, almost all the multiphase and transport models coupled with geochemical reaction models only monitor the changes of porosity and permeability induced by mineral and precipitation (Knauss et. al, 2005; Xu et. al, 2007). To our knowledge, there is no research in the literature that has fully coupled the changes of porosity and permeability with multiphase flow models for geologic CO_2 sequestration. Therefore, the impact of the non-coupling between fluid flow and porosity and permeability change is largely unknown. Furthermore, it is of great significance to account for the interaction between the fluid flow and changes in porosity and permeability since the phase pressure is very sensitive to the changes of porosity and permeability and it is the injection pressure that would have significant impact on the cost of injection and the probability of safely storing CO_2 in the deep aquifers.

1.2 Motivation and objective

From the introduction in Section 1.1, we can conclude that there is few, if not at all, studies that incorporate the transition between Darcy flow and Forchheimer flow for multiphase flow cases and our understanding of Forchheimer flow behavior through porous media is currently very limited, although accurate characterization of the fluid flow in the porous media is one of the most important aspects for many applications in petroleum engineering, environmental hydrogeology and more recently CO_2 geologic sequestration and storage in deep saline aquifers. We can also find out that the kinetic mass transfer of SO_2 and CO_2 from CO_2 stream to the saline and the fully coupling between the changes of porosity and permeability and multiphase flow are two significant dimensions to investigate the brine acidification and the induced porosity and permeability changes due to SO_2 co-injection with scCO_2.

Therefore, the objectives of this thesis is: (i) to investigate the transition behavior between Darcy flow and Forchheimer flow for multiphase cases, especially for the applications in CO_2 geologic storage; and, (ii) to gain a more thorough understanding of the magnitude and time scale of brine acidification and the induced porosity and permeability changes for the case of SO_2 co-injection during geologic carbon sequestration in deep saline formations with the incorporation of the kinetic mass transfer of SO_2 and CO_2 from CO_2 stream to the water and the fully coupling between the changes of porosity and permeability and multiphase flow.

1.3 Organization of the thesis

The thesis includes six chapters. The introduction is given in this chapter.

A comprehensive literature review of the research topics relevant to this study is presented in Chapter 2. These topics include an overview of Carbon Capture and Storage (CCS), flow regimes and flow transition criterion in porous media, the corrections of the Forchheimer coefficient, non-Darcy flow modeling, effects of co-injected impurities on CO_2 geological storage, and geochemical modeling.

In Chapter 3, the governing equations for multiphase flow are developed, and the numerical methods used to solve the equations are given. Then the model is validated with a semi-analytical solution. In addition, a new method to determine the critical

Forchheimer number for single and multiphase flow is proposed. Finally, the developed multiphase model and the critical Forchheimer number (used to identify the transition between Darcy and Forchheimer flow regions) are used in the analysis of CO_2 injection into a deep saline aquifer (2-D domain).

In Chapter 4, the governing equations for multiphase contaminant transport and the geochemical model are developed, and the numerical methods used to solve the equations are given. The developed model in this chapter is coupled with the multiphase flow model presented in Chapter 3 with the incorporation of the fully coupling between the changes of porosity and permeability and multiphase flow. Then the complete model is used to investigate the brine acidification and the induced porosity and permeability changes due to co-injection with $scCO_2$ including the kinetic mass transfer of SO_2 and CO_2 from CO_2 stream to the water for a 1-D domain with the assumption of Darcy flow.

Chapter 5 focuses on the investigation of the transition behavior between Darcy and Forchheimer flow and the kinetic dissolution of SO_2 and its resultant brine acidification and induced porosity and permeability changes during SO_2 co-injection with CO_2 into a deep saline aquifer (a 2-D large domain).

Finally, in Chapter 6, conclusions and recommendations for further research are given.

Chapter 2 Literature review

In this chapter, a comprehensive literature review of the research topics relevant to this study is presented, including an overview of Carbon Capture and Storage (CCS), flow regimes and flow transition criterion in porous media, the corrections of the Forchheimer coefficient, non-Darcy flow modeling, effects of co-injected impurities on carbon dioxide (CO_2) geological storage, and geochemical modeling.

2.1 An overview of CCS and mechanisms for geologic storage of CO_2

2.1.1 An overview of CCS

Carbon capture and storage (CCS), is the process of separating carbon dioxide (CO_2) from large industrial point sources, such as large fossil fuel, biomass energy, and industrial facilities, transporting it to an injection site, and storing it underground for geologically significant periods of time.

The first step in CO_2 sequestration is to accumulate concentrated CO_2 gas for transport and storage. Typically, CO_2 from large-scale industrial facilities or power plants is conventionally captured in three different processes: (1) pre-combustion, which is designed to remove CO_2 from gas mixture produced typically by gasification (gasification of the fossil fuel with oxygen generates a synthesis gas---a gas mixture of H_2 and CO_2) prior to its combustion; (2) post-combustion, which separates the diluted CO_2 emitted from the flue gas mixture due to the combustion of fossil fuels or biomass; and (3) oxy-fuel combustion, which uses pure oxygen instead of air for combustion, producing flue gases that consist mostly of CO_2 and water from which the CO_2 is more readily separated.

Following separation, CO_2 is compressed to increase its density and make it easier and cheaper to transport. In the end, CO_2 has to be transported to suitable storage sites through various options of overland transport. Feasible methods include truck, train, ship, and pipeline (Parfomak et al., 2008). The cost-effective mode of transport can depend on the locations of capture and storage, distance from source to storage, and the quantities of CO_2 being transported, but the quantity to be transported is the most important factor

(Metz et al., 2005). Transports by truck, train, and ship are applicable options for small to medium volumes of CO_2 over very long distances. For large volumes of CO_2, pipeline is the most practical option for overland transport because at least 2 to 3 million metric tons (Mt) per year of CO_2 are generally required to be transported from a single fossil fuel power plant (Metz et al., 2005). Pipelines are currently the most common approach to transport large amounts of compressed CO_2 over long distances because they are the cheapest type of transport. CO_2 pipelines operate at ambient temperature and at a pressure of more than 74 bars to maintain the supercritical state of CO_2, with primary compressor units placed where CO_2 is injected, and booster compressors located as needed further along the pipeline (Parfomak et al., 2008).

As for CO_2 storage, various sequestration methods have been considered. Carbon dioxide sequestration involves the injection of CO_2 into various formations: (1) geological storage, providing that the CO_2 is injected into underground with a depth at least 800-1000 meters in order to maintain a supercritical state of CO_2; (2) ocean storage, where the CO_2 is injected deep into the ocean below approximately 3,000 meter depths.

1) Geological storage

The proposal of geological storage of anthropogenic CO_2 as a greenhouse gas mitigation option was inspired from the engineered injection of CO_2 into subsurface geological formations for enhanced oil recovery (EOR) which was first undertaken in Texas, USA, in the early 1970s. After that, little research was done until the early 1990s, when the proposal became more and more feasible through the work of individuals and research groups (Marchetti, 1977; Baes et al., 1980; Kaarstad, 1992; Koide et al., 1992; van der Meer, 1992; Gunter et al., 1993; Holloway and Savage, 1993; Bachu et al., 1994; Korbol and Kaddour, 1994; Holloway, S., 2001; Shaw et al., 2002).

Currently, ideal candidate geological formations suitable for geologic storage of CO_2 are believed to include depleted oil and gas reservoirs, deep unmineable coal seams and deep saline aquifers (Metz et al., 2005).

Depleted oil and gas reservoirs are attractive candidates for CO_2 storage because of three reasons. First, the geological structure and physical properties of hydrocarbon reservoirs are generally well understood with computer models available to predict the displacement behavior and trapping of hydrocarbons; second, those fields have been

confirmed to have adequate integrity and safety to trap CO_2 (as well as gas or oil before); third, storage costs may be partly or totally compensated by the saving of using some of the existing infrastructure and wells for handling CO_2 storage operations and by the sale of the additional oil or gas recovered in the case of enhanced oil or gas recovery. However, geographic distribution and capacity is limited. In addition, plugging of abandoned wells in many mature fields began many decades ago when wells were simply filled with a mud-laden fluid. Therefore, the condition of wells penetrating the caprock must be assessed (Winter and Bergman, 1993) if CO_2 is considered to be injected.

When it comes to deep coal seams, the storage of CO_2 is realized by that coal has a higher affinity to adsorb gaseous CO_2 than methane and thus the injected CO_2 in coal seams can displace methane, at the same time enhancing Coalbed methane (CBM) recovery. However, most CBM-producing wells in the world are less than 1000 m deep (Metz et al., 2005).

Saline formations are deep sedimentary rocks saturated with formation waters or highly mineralized brines which have a relatively high affinity for CO_2. Those aquifers with a confining layer that serves as a cap-rock exist in many places. Their storage capacities are significantly higher than those of oil and gas reservoirs and they are more likely to be found close to large CO_2 point sources. However, these sites are still relatively poorly understood regarding their properties and characteristics compared to oil and gas fields and thus, the risk of encountering unknown faults or fractures is higher than that in oil and gas reservoirs which have been previously exploited. Therefore, additional research is required.

The IPCC report suggests that CO_2 could be isolated for millions of years in optimized managed geological storage sites, and the sites are likely to retain over 99% of the injected CO_2 over 1,000 years (Metz et al., 2005). Furthermore, about 6,000 square miles of suitable rock formations in the U.S. have been mapped and they could be used to store 500 years worth of U.S. CO_2 emissions.

2) Ocean storage

Another possible option of the disposal of CO_2 is storing it in the deep oceans. The ocean is the largest reservoir for carbon and the largest part being in the form of deep carbonate sediments. The captured CO_2 would be injected into the deep ocean through

pipeline. Various methods have been proposed including (Brewer et al., 1999; Metz et al., 2005), directly depositing CO_2 onto the sea floor at depths greater than 3,000 meters where CO_2 is denser than sea water to form a lake of liquid CO_2 on the seabed, converting CO_2 to bicarbonates with the use of limestone, and storing CO_2 in solid clathrate hydrates structures, which already exist on the ocean floor, implying permanent CO_2 storage.

Numerical models of the ocean indicate that placing CO_2 in the deep ocean would isolate most of the CO_2 from the atmosphere for several centuries, but over longer times the ocean and atmosphere would equilibrate. Relative to atmospheric release, direct injection of CO_2 into the ocean could reduce maximum amounts and rates of atmospheric CO_2 increase over the next several centuries. Direct injection of CO_2 in the ocean would not reduce atmospheric CO_2 content on the millennial time scale (Hoffert et al., 1979; Kheshgi et al., 1994).

The likely environmental impact of oceanic storage is not well understood, but it is generally considered to have negative effects because large concentrations of CO_2 could kill ocean organisms and because dissolved CO_2 would eventually interact with the atmosphere due to a leakage issue. Moreover, carbonates of CO_2 as H_2CO_3 also cause an increase in the acidity of ocean water, which might have significant negative impact on the nearby ecosystems.

2.1.2 Mechanisms for geologic storage of CO_2

Carbon dioxide can be retained in geologic formations by the following four mechanisms (Hitchon, 1996; Dooley, 2006; Mazumder et al., 2006): first, CO_2 can be trapped as a supercritical fluid under a low permeability caprock. This process is commonly called hydrodynamic trapping and relied on the physical displacement of pore fluids. Second, CO_2 can dissolve into the fluids present in the formation, referred to as solubility trapping. Third, CO_2 can react directly or indirectly with the brine and minerals in the geologic formation leading to the precipitation of secondary carbonate minerals referred to as mineral trapping. Fourth, in coal seams, methane molecules are sorbed within the coal matrix; however, since the chemical bond between the coal and CO_2 is favorable, CO_2 will replace methane when it is injected into a coal layer. This mechanism

is referred to as CO_2 sorption on coal. Sorption of CO_2 causes coal swelling and can have a detrimental effect on its permeability (Mazumder et al., 2006). The first three mechanisms are highly related to CO_2 storage in deep saline aquifers and thus are described below in more detail.

Hydrodynamic trapping refers to storage of free CO_2 in the pore spaces of sedimentary layers and the transport of that CO_2 away from the surface by regional groundwater flow (Bachu et al., 1994). Free CO_2 is the main form of storage during injection, which can last 30-50 years. The injected CO_2 is subject to injection-related hydrodynamic gradients and to buoyancy forces. The latter may cause CO_2 to form a rising and laterally-spreading plume until it meets a confining layer that hinders its vertical rising. Provided a near horizontal confining layer and relatively small density difference between the brine and CO_2, the CO_2 will travel with regional groundwater flow (Bachu et al., 1994), unless faults or other high permeability zones in the stratigraphical cap-rock provide escape routes to the surface. The increasing pressure required for reasonable rates of CO_2 injection and buoyancy forces can widen small fractures, increasing the risk for CO_2 escape (Saripalli and McGrail, 2002; Klusman, 2003).

Solubility trapping refers to the CO_2 that dissolves into the brine. The CO_2-brine solution has a density greater than brine alone preventing buoyant flow of the CO_2 toward the surface, even along high permeability vertical pathways such as faults. Most models of solubility trapping assume instantaneous equilibrium between the brine and free CO_2. The solubility of CO_2 varies as a function of pressure, temperature, and salinity. Numerous models for CO_2 solubility in aqueous solutions have been published to describe this relationship (Pruess and Garcia, 2002; Duan and Sun, 2003; Spycher et al., 2003; Xu et al., 2004b; and McPherson and Cole, 2005), though few deal with high ionic strength, multi-component brines.

The extent to which CO_2 dissolves into the brine is influenced by the migration of the CO_2 front and by the rate of dispersion and diffusion of CO_2. Viscous fingering and buoyancy flow, which tend to limit the storage of free CO_2, may increase solubility trapping by increasing the surface area of the brine-CO_2 contact, allowing more rapid solution. In addition, diffusion of CO_2 into the brine can set up reverse density gradients

that lead to convective mixing and increased rate of dissolution of free CO_2 (Lindeberg & Wessel-Berg, 1997).

Through these processes, dissolved CO_2 becomes the dominant form of CO_2 storage in aquifers over periods of tens to hundreds of years following injection (Weir, 1995). Over these timescales the CO_2 disperses (Law & Bachu, 1996) by dispersion and diffusion, and dissolution into the brine (Lindeberg & Wessel-Berg, 1997). Continued migration and dispersion drive both free and dissolved CO_2 toward zero (McPherson & Cole 2000).

Mineral trapping is the fixing of CO_2 in carbonate minerals due to geochemical reactions among aquifer brines, formation minerals, and aqueous species of CO_2. The mass of CO_2 sequestered as carbonate minerals is sensitive to formation mineral and aquifer brine composition, pressure, temperature, and brine-rock ratio. Time is also important because mineral trapping reactions take hundreds to thousands of years and more to complete (Gunter et al., 1997).

Dissolution of carbonate minerals does not lead to mineral trapping of CO_2 (Gunter 1993). However, carbonate dissolution, and other mineral precipitation and dissolution reactions can affect sequestration capacity by altering the permeability of the aquifer near the injection site.

2.1.3 Why saline aquifers?

Deep saline aquifers provide no economic return for CO_2 injection, but CO_2 sequestration in deep saline aquifers is an especially appealing option due to closed structural traps, the great abundance of injection sites, huge potential storage capacity, close proximity to power-plant sources of CO_2, and technical feasibility (Hitchon et al. 1996; Bruant et al., 2002; Bachu, 2003; Bachu, 2008; Benson and Cole, 2008). Deep aquifers potentially have CO_2-storage capacities sufficient to hold many decades worth of CO_2 emissions. In the United States, deep saline aquifers have a larger potential storage capacity than any other type of sedimentary formation, with estimates as high as 3630 Gt of CO_2 storage. Table 2.1 summarizes the range of capacity estimates and the main trapping mechanisms and storage safety and environmental risk for different geological sequestration methods of CO_2.

Table 2.1 Summary of storage capacity and main trapping mechanisms for different storage options

Formation	Trapping mechanisms	The US (Gt CO2)	Worldwide (Gt CO2)	Storage integrity	Environmental risk
Saline Aquifers	Hydrodynamic, dissolution, mineralization	3630	9500	Average	Average
Depleted Oil + Gas Reservoirs	Hydrodynamic, dissolution, mineralization	12+35	120+700	High	Low
Deep Unmineable Coal Seams	Primarily chemical adsorption	30	140	Average	Average
Deep Saline Filled Basalts Formations	Hydrodynamic, dissolution, mineralization	240	NA	Average	Average
Ocean	Dissolution, mineralization	NA	1000–10,000	Medium	High

Source: Adapted from Dooley, J. J. (2006) and Shukla et al. (2010)

Sleipner is the world's first and largest deep saline formation storage project. This project has captured and stored approximately one million tonnes of CO_2 per year since 1996. At Sleipner, the CO_2 is compressed and injected into the 250 m thick aquifer 800 m below the seabed. There are currently two other large storage sites in deep saline formations: In Salah, Algeria (since 2004), and Snøhvit, Barents Sea (since 2008). The Gorgon project in Australia is expected to start operation in 2015 and last for approximately 40 years and is so far known as the largest CO_2 storage project in the near future. CO_2 will be injected to a depth of approximately 2.3 km into a deep saline formation below Barrow Island, with an injection rate of 3.4 million tonnes of CO_2 per year.

However, these existing projects are small by comparison with the size of projects required to store gigatonnes of CO_2 within a decade (Haszeldine, 2009). Full-scale projects are anticipated to be five-to-ten million tonnes or more per year per site. The summary of the projects is shown in Table 2.2.

2.2 Flow regimes in porous media

Due to the wide distribution of pore sizes and shapes in any naturally occurring porous media, the difference in fluid properties, and the huge variations in the flow rates, several different flow patterns can be distinguished for the fluid flow in porous media. Analogous to flow in pipes and conduits, several researchers (Holditch et al., 1976; Basak, 1977; Dybbs and Edwards, 1984; Seguin et al., 1998; Yazdchi et al., 2010) have tried to define a flow pattern map in porous media to distinguish different flow behaviors and to predict the onset and termination of certain flow type. Typically for flow in pipes and conduits, the Reynolds number is used to delineate flow regimes. Laminar flow occurs when Reynolds number is less than 2300 implies, while a greater number implies the onset of turbulent flow. Due to previous belief that non-Darcy flow in porous media was similar to turbulent flow in a conduit, the Reynolds number for identifying turbulent flow in conduits was adapted to describe non-Darcy flow in porous media. In porous media however, there is no clear Reynolds number that defines the transitions between different flow patterns. The non-linearity experienced in non-Darcy flow is a result of inertia effects instead of turbulent effects. Therefore, non-Darcy flow is known to occur at a much more lower Reynolds number in porous media. The Reynolds number in porous media is given by

$$\mathrm{Re} = \frac{\rho d v}{\mu} \tag{2.1}$$

where d is the average grain diameter of the grains in the porous media, ρ is the fluid density, μ is the viscosity and v is the Darcy velocity. Since the Reynolds number is commonly associated with the difficulty to define and determine the characteristic length used, especially for porous media with complex soil matrix structure, a new Reynolds-number-based Forchheimer number is proposed (Green et al., 1951; Ma et al., 1993; Andrade et al., 1999;) for media with Forchheimer flow and expressed as

$$f = \frac{\rho k \beta v}{\mu} \tag{2.2}$$

This equation is essentially another Reynolds number with the characteristic length defined as βk, which is equivalent to the diameter d in Equation 2.1.

In the literature, different flow patterns have been observed (Holditch et al., 1976; Basak, 1977; Dybbs and Edwards, 1984; Seguin et al., 1998; Yazdchi et al., 2010) because of the difference in the flow velocity and in the nature of the porous media. Therefore, different versions of flow pattern maps can be found in the literature. For example, four major flow regimes were distinguished for the fluid flow in porous media, proposed by Dybbs and Edwards (1984) using laser anemometry and visualization technique and described as follows.

Table 2.2 Summary of operating (or soon to be operating) commercial CO_2 projects for deep saline aquifers

Project/Location	**Operator**	**Injection Start Date**	**Annual Injection Rate**	**Total Planned Storage**
SLIEPNER/ North sea	StatoilHydro	1996	1 Mt/yr	20 Mt
IN SALAH /Algeria	Sonatrach, BP,StatoilHydro	2004	1.2 Mt/yr	17 Mt
SNOHVIT /Norway	StatoilHydro	2008	0.7 Mt/yr	23 Mt
Weyburn / Canada	EnCana, IEA	2000	1 Mt/yr	20 Mt
LEUCADIA /Louisiana	Leucadia Energy	2014	4.5 Mt/yr	-
BELCHATOW/ Poland	PGE Elektrownia and Alstom	2014-2015	1.8 Mt/yr	-
FORT NELSON/Canada	Plains CO2 Reduction (PCOR) Partnership	2013-2015	1.2 Mt/yr	6 Mt
GORGON / Australia	Spectra Energy Chevron	2015	3.4 Mt/yr	125 Mt
QUEST / Canada	Shell Canada	2015	1.2 Mt/yr	-

i. Darcy flow

Darcy or laminar flow where the flow is dominated by viscous forces and the pressure gradient varies strictly linearly with the flow velocity. The Reynolds number for this flow pattern is less than 1.

ii. Forchheimer flow

At increasing Reynolds number, a transition zone is observed leading to flow dominated by inertia effects. This flow regime begins in the range Re=1~10. This laminar inertia flow dominated region persists up to a Reynolds number of ~150.

iii. Forcheheimer-turbulent transition flow

An unsteady laminar flow regime for Re =150 ~ 300 is characterized by occurrence of wake oscillations and development of vortices in the flow profile.

iv. Turbulent flow

A highly unsteady and chaotic flow regime for Re > 300, it resembles turbulent flow in pipes and is dominated by eddies and high head losses.

Another version of flow pattern map was proposed by Basak (1977), who included a pre-Darcy zone but removed the Forchheimer-turbulent transition flow regime from his flow pattern map, as can be seen from the diagrammatic representation of the flow regimes in a porous media in Figure 2.1.

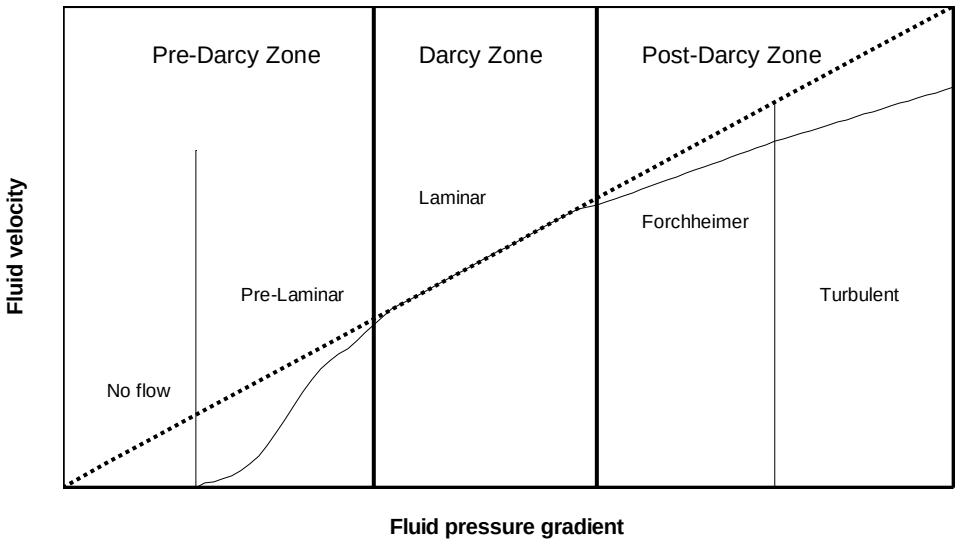

Figure 2.1 Flow regimes in porous media (Re-plotted after Basak (1977))

2.3 Flow transition criterion

Fluid flow through porous media is an important aspect of many applications in petroleum engineering, environmental hydrogeology and more recently in applications such as CO_2 sequestration and storage. For the successful design and operation of projects in these areas, it is essential to accurately describe the behavior of fluid flow through porous media. In general this behavior is characterized by Darcy's law. According to Darcy's law, the pressure gradient is linearly proportional to the fluid velocity in the porous media. For this condition the one-dimensional Darcy equation can be written as

$$-\nabla \phi = \frac{\mu v}{k} \tag{2.3}$$

where ϕ is the flow potential, μ is the viscosity, v is the Darcy velocity, and k is the intrinsic permeability.

In certain applications deviations of fluid flow behavior from Darcy's law have long been observed (Chilton et al., 1931; Green et al., 1951; Ergun, 1952; Tek et al., 1962; Scheidegger, 1972; Katz and Lee, 1990; Andrade et al., 1999; Zeng and Grigg, 2006). To describe these cases various terms, such as non-Darcy flow, turbulent flow, inertial flow, high velocity flow, nonlinear flow, etc., have been used (Firoozabadi and Katz, 1979). In the literature we see many attempts to redefine the Darcy equation for these cases. For example, Forchheimer (1901) added a second order velocity term to represent the microscopic inertial effect, and modified the Darcy equation into the Forchheimer equation,

$$-\nabla\phi = \frac{\mu v}{k} + \beta\rho v|v| \tag{2.4}$$

where ρ is the fluid density, β is the Forchheimer coefficient which may appear under other identifiers such as the Forchheimer coefficient, the inertial coefficient, the non-Darcy coefficient, the velocity coefficient and the turbulence factor.

The criterion for the transition between Darcy flow and Forchheimer flow is described in terms of two different criteria: (i) one of which uses the Reynolds number (Type-I) defined by Equation (2.1); and, (ii) the other is the Forchheimer number (Type-II) expressed as Equation (2.2). The Type-I criterion has been applied mainly in columns of packed particles in which characteristic length, usually the representative particle diameter, is available, while the Type-II criterion has been used mainly in numerical models. When compared with the Reynolds number, the critical merit of the Forchheimer number is the consistent definition and the physical meaning of the variables involved while the Reynolds number is commonly associated with the difficulty to define and determine the characteristic length used, especially for porous media with complex matrix structure.

The earliest work on the criterion for non-Darcy flow behavior in porous media was done by Chilton and Colburn (1931), who conducted fluid flow experiments on packed particles, and first defined the Reynolds number in porous media as Equation

(2.1). Their experiments show that the critical Reynolds number for non-Darcy flow to become significant is in the range of 40–80.

Fancher and Lewis (1933) flowed crude oil, water, and air through unconsolidated sands, lead shot, and consolidated sandstones and showed that non-Darcy flow occurs at Re=10-1000 in unconsolidated porous media and at 0.4−3 in loosely consolidated rocks by using Chilton and Colburn's definition of the Reynolds number. By including porosity, Ergun (1952) modified Chilton and Colburn's definition and determined a critical value of Re=3–10 from their experiments with gas flow through packed particles.

Realizing the difficulty of determining the particle diameter, Green and Duwez (1951) conducted nitrogen gas flow experiments through four different porous metal samples, first proposed the Forchheimer number expressed in Equation (2.2) and observed that non-Darcy behavior started when the Forchheimer number is 0.1-0.2.

Since the late 1980s, numerical modeling on this topic has increased rapidly. Blick and Civan (1988) used a capillary–orifice model to simulate fluid flow in porous media and concluded that the critical Reynolds number defined in Equation (2.1) for non-Darcy behavior is 100. Du Plessis and Masliyah (1988) used a representative unit cell to model fluid flow in porous media and derived a relationship between porosity and tortuosity, which further led to a correlation between Reynolds number and tortuosity. Their results show that a critical Reynolds number can be from 3 to 17.

Ma and Ruth (1993) numerically simulated non-Darcy behavior using a diverging–converging model. After defining both the Reynolds and Forchheimer number, they found that the critical Reynolds number is 3–10 while the corresponding Forchheimer number is 0.005–0.02. Andrade et al. (1998) modeled fluid flow in a disordered porous media. Following the definition of Equation (2.2), they showed that the critical Forchheimer number is 0.01–0.1.Thauvin and Mohanty (1998) used a network model to simulate the porous media, whose result shows that critical Reynolds number is 0.11.

In summary, critical values for non-Darcy flow vary from 1 to 100 for the Type-I criterion, and from 0.005 to 0.2 for the Type-II criterion. A more detail summary of the single phase transition criterion between Darcy flow and Forchheimer flow can be found in the literature (e.g., Chilton et al., 1931; Green et al., 1951; Ergun, 1952; Ma et al., 1993; Andrade et al., 1999; Zeng and Grigg, 2006) while there is very few discussion on

the criterion for multiphase transition. The determination of the critical value for the transition is usually based on experimental data, with some based on theoretical derivation for single phase flows (Ahmed et al., 1969; Ma et al., 1993; Andrade et al., 1999). Most of the experimental data are from gas flooding experiments (e.g., Chilton et al., 1931; Green et al., 1951) with few from water flooding experiments (e.g., Sobieski and Trykozko, 2012). During the procedure, usually a curve for the friction factor (the formulas is dependent of the physical phases of the fluid) versus the Forchheimer (or Reynolds) number is plotted and the critical value for the transition between Darcy and Forchheimer flows is selected based on the Forchheimer (or Reynolds) number when the linear relationship between the two variables begins to deviate.

2.4 The Forchheimer coefficient β, its measurement and correlations

Due to diversity in experimental procedure, fluids used for the experiments, geological formations and pore geometry of porous media matrix, there is variability in the definitions and correction formulas used for the Forchheimer coefficient β in the literature. Both theoretical and empirical corrections of the Forchheimer coefficient will be reviewed. Since no theoretical equations for multiphase have been found so far, the review on the theoretical equations will be focused on single phase only while the review on the empirical equations will be divided into two parts, one for single phase and the other for multiphase case.

2.4.1 Theoretical equations

The theoretical corrections of the Forchheimer coefficient are based on the method using capillaric models to describe fluid flow through porous media, for which a detail summary can be found in Scheidegger (1953, 1974) and Bear (1988). Those capillaric models can be further divided into parallel and serial models. In the parallel model, the porous medium is assumed to be made up of a bundle of straight, parallel capillaries of uniform diameter. Based on the work of Ergun et al. (1949) and Polubarinova-kochina (1952), Li and Engler (2001) derived an equation for the Forchheimer coefficient for a parallel model given by

$$\beta = \frac{C}{K^{0.5}\theta^{1.5}} \tag{2.5}$$

where C is a constant and K and θ are intrinsic permeability and porosity, respectively. In serial type model, the pore space is assumed to be serially lined up and capillaries of different pore diameter are set to be aligned in series. Li et al. (2001) also proposed a correction for a series model based on the work of Scheidegger expresses as

$$\beta = \frac{C'\tau}{K\theta} \tag{2.6}$$

where C' is a constant and τ is the tortuosity of the medium.

2.4.2 Empirical equations

1) single phase

Despite the great diversity in the correction formulas for the Forchheimer coefficient, permeability is the key parameter in all the corrections while porosity and tortuosity are the main parameters and may be included in the formulas as well. Therefore all the empirical equations for the Forchheimer coefficient can be summarized in a general expression as described by

$$\beta = \frac{a\tau^{d}}{K^{b}\theta^{c}} \tag{2.7}$$

where a, b, c and d parameters vary with different formulas. Table 2.3 shows a summary of correction formulas based on Equation (2.7) from the literature. It needs to be noted that this is not an exhaustive listing and the corrections listed here are only the important ones. A more detailed review of this subject can be found in Li and Engler (2001) and Lopez-hernandez et al. (2004).

2) multiple phases

As for the multiphase flow, Geertsma (1974) is the first to develop an expression for the Forchheimer coefficient for two-phase flow, by stating that the permeability used in single phase flow should be replaced by the effective permeability for two-phase flow and the porosity used in single phase flow should be modified to be the product of porosity and the corresponding phase saturation with the equation for non-wetting phase Forchheimer coefficient given as,

$$\beta_n = \frac{0.005}{\left(kk_r^n\right)^{0.5}\left(\theta(1-S_w)\right)^{5.5}} = \frac{0.005}{\left(kk_r^n\right)^{0.5}\left(\theta S_n\right)^{5.5}} \tag{2.8}$$

From equation (2.8), we can see that the Forchheimer coefficient for the non-wetting phase increases when the water saturation increases. Several other authors (Wong, 1970; Coles and Hartman, 1998; Grigg and Hwang, 1998; Evans et al., 1987; Evans and Evans, 1988) also found that the Forchheimer coefficient for non-wetting phase increased with increased wetting phase saturation.

Table 2.3 A list of correction formulas for the Forchheimer coefficient

Equation	a	b	c	d	Unit/ β	Unit/ K	Source
Jones	6.15E+10	1.55	0	0	1/ft	md*	Jones, 1987
Pascal et al.	4.8E+12	1.18	0	0	1/m	md	Pascal et al., 1980
Cooke_sand 8/12	5.38E+11	1.24	0	0	1/ft	md	Cooke, 1973
Cooke_sand 10/20	8.51E+11	1.34	0	0	1/ft	md	Cooke, 1973
Cooke_sand 20/40	3.41E+12	1.54	0	0	1/ft	md	Cooke, 1973
Cooke_sand 40/60	2.14E+12	1.60	0	0	1/ft	md	Cooke, 1973
Martins et al.	8.32E+09	1.04	0	0	1/ft	md	Martins et al., 1990
Ergun	4.24E+04	0.50	1.50	0	1/m	md	Ergun et al., 1949
Janicek and Katz	1.82E+08	1.25	0.75	0	1/m	md	Janicek et al., 1955
Geertsma	5.00E-03	0.50	5.50	0	1/cm	cm^2	Geerstma, 1974
Coles et al.	2.49E+11	1.79	-0.54	0	1/ft	md	Coles et al., 1998
Li et al.	1.39E+07	0.85	1.15	0	1/cm	md	Li et al., 2001
Tek et al.	5.50E+09	1.25	0.75	0	1/m	md	Tek et al.,1962
Macdonald et al.	4.52E+04	0.50	1.50	0	1/m	md	Macdonald et al., 1979
Cooper et al.	5.62E-04	1.02	0	1.94	1/cm	cm^2	Cooper et al., 1999
Thauvin et al.	1.55E+04	0.98	0.29	3.35	1/cm	D	Thauvin et al., 1998
Liu et al.	8.91E+08	1	1	1	1/ft	md	Liu et al., 1995

*millidarcy

Based on experimental and analytical investigations, Kutasov (1993) proposed the following equation to estimate β for gas phase for both situations: with a mobile liquid saturation and with an immobile liquid saturation, expressed as

$$\beta_n = \frac{1432.6}{\left(k_g\right)^{0.5}\left(\theta(1-S_w)\right)^{1.5}} \tag{2.9}$$

where β is in 1/cm, K_g is gas effective permeability in Darcy, and S_w is water saturation. It needs to be noted that the effective permeability is the product of the relative permeability and absolute permeability.

Graves (1994) obtained 407 data points from their experiments and the data obtained by Cornell and Katz (1953), Geertsma (1974) and Evans et al. (1987) and found the following empirical correlation for β

$$\beta_g = \frac{2.11\times10^{10}}{\left(k_g\right)^{1.55}\left(\theta(1-S_w)\right)} \tag{2.10}$$

where is in 1/ft and K_g is gas effective permeability in millidarcy (md).

Recently, Ahmadi et al. (2010) further adapted Liu's equation to two-phase conditions yielding,

$$\beta_\alpha = \frac{2.923*10^{-6}\tau}{\left(kk_r^\alpha\right)\left(\theta\right)} \quad ;\ \alpha = w,\ n \tag{2.11}$$

More recently, Zhang and Aral (2013) argued that it is necessary and more physically sound to include the saturation term in the denominator of the correction equation, as Equation (2.8), (2.9) and (2.10) do. Otherwise, the direct change in the Forchheimer flow coefficient due to saturation difference cannot be precisely described if one uses an equation like Equation (2.11). Therefore, they adopt a correction based on the following equation which incorporates the direct impact of saturation on the Forchheimer flow coefficient to analyze the Darcy-Forchheimer flow behavior near the well-bore area during CO_2 injection into deep saline aquifers

$$\beta_\alpha = \frac{C_\beta\tau}{\left(kk_r^\alpha\right)\left(\theta S_\alpha\right)} \quad ;\ \alpha = w,\ n \tag{2.12}$$

where C_β is a numerical constant having the unit of a length (e.g., m).

2.5 Non-Darcy flow modeling

Numerical modeling of non-Darcy flows began in the 1960s; some of the pioneer workers include Smith (1961) and Ramey (1965), who investigated the effects of gas flow on well testing. Researchers in recent times are looking for newer and better ways of modeling fluid flow in porous media while integrating the non-Darcy effects into the numerical models. The non-Darcy flow is also referred to Forchheimer flow in the literature (Civan and Evans, 1993; Ewing et al., 1999; Barree and Conway, 2004, 2005, 2007). Recently, realizing the importance of the non-Darcy flow in industrial applications,

many authors (Bennethum et al., 1997; Ewing et al., 1999; Belhaj et al. 2003; Schmidt, 2004; Su (2004); Jamiolahmady et al. (2006); Barree and Conway, 2007; Ahmadi and Arani, 2008; Wu et al., 2011; Zhang et al., 2012; Zhang and Aral, 2013) have come up with different modeling approaches, especially for modeling multiphase non-Darcy flow.

Hassanizadeh and Gray (1987) first derived the Forchheimer equation for single-phase flow using hybrid mixture theory, and discussed the origin of the onset of such nonlinearity. A decade later, Bennethum and Giorgi (1997) derived a Forchheimer-type equation for two-phase flow through an isotropic porous medium using hybrid mixture. Ewing et al. (1999) developed a numerical model for the description of the non-Darcy multiphase flow through isotropic porous media including well equations for high velocity flow described by the Forchheimer equation. The equations can be used for the case of isotropic porous material and fully penetrating vertical wells. Belhaj et al. (2003) derived a new expression for the diffusivity equation based on the Darcy-Forchheimer equation (e.g., Equation (2.4)) in two dimensions and compared the numerical simulation to their experimental results. Based on the comparison, they concluded that the Forchheimer model gave more realistic result for all ranges of pressure gradients, flow rates, permeabilities, porosities, viscosity and fluid density.

Barree and Conway (2004) performed an experimental analysis of the non-Darcy flow through porous media and represented the Forchheimer equation in a form similar to the Darcy equation as given by

$$v = -\frac{k}{\mu}\frac{\nabla\phi}{1+\frac{\beta\rho k}{\mu}|v|} \tag{2.13}$$

Su (2004) in his publication detailed how non-Darcy flow modeling can be integrated into a reservoir simulator, especially for multiphase flow modeling. His model also proposed the Darcy-Forchheimer equation for each phase flowing in the reservoir; his phase based non-Darcy flow equation is given as

$$-\nabla\phi_\alpha = \frac{\mu_\alpha v_\alpha}{k\, k_r^\alpha} + \beta_\alpha \rho_\alpha v_\alpha |v_\alpha| \quad ; \ \alpha = w,\ n \tag{2.14}$$

In the study, he used a cell-to-cell non-Darcy flow resistance flux factor to multiply the Darcy flow flux term. Su applied his model to both oil and gas well, based on the result

of his simulations he pointed out that Darcy-Forchhiemer can be applied to a multiphase system and the model can be easily integrated with a full blown numerical simulator.

Jamiolahmady et al. (2006), when modeling flow in a crushed perforated rock, developed a mathematical model based on Equation (2.4). From the equation, they obtained the same expression for the velocity as Equation (2.13).The expression was solved based on the finite element method used in the Femlab (COMSOL Multiphysics) mathematical modeling software.

Barree and Conway (2007) extended Equation (2.13) to multiphase flow conditions and proposed a new Forchheimer type equation for the description of non-Darcy flow for a even higher flow velocity. Wu et al. (2011) supported and discussed the Barree-Conway approach for modeling multiphase non-Darcy flow through porous media.

Lasseux et al. (2008) derived the macroscopic model for two-phase, incompressible, Newtonian fluid flow with the inertial effects (non-Darcy effects) through homogenous porous media from the continuity and Navier–Stokes equations using the method of volume averaging. In a later study by Ahmadi et al. (2010), non-Darcy inertial two-phase incompressible and non-stationary flow in heterogeneous porous media is analyzed using numerical simulations and saturation fields are shown to have a structure markedly different from the classical case without inertia effects.

In a recent study by Zhang et al. (2012), non-Darcy flow behavior for single phase is described using the Forchheimer equation, and the Forchheimer number is used to determine if the flow is of Darcy or Forchheimer. The results show that when Forchheimer flow in the near-well region is considered, both the fluid velocity and the wellbore pressure are much different than the Darcy flow velocity and pressure conditions.

More recently, in a study by Zhang and Aral (2013), a generalized Darcy-Forchheimer multiphase flow model is used for the analysis of two-phase fluid flow where flow characteristics may transition between Darcy and Forchheimer flow behavior by comparing the Forchheimer number to the critical Forchheimer number for each phase. The proposed approach is demonstrated for a problem in which the injection of CO_2 into a deep saline aquifer is analyzed. The simulation results show that the proper identification of Forchheimer flow domain can improve the characterization of

displacement efficiency of the immiscible fluid. This in turn improves the proper identification of the storage capacity of saline aquifers for the same injection rate and volume at a site.

2.6 Effects of co-injected impurities on CO_2 geological storage

From Table 2.4 it can be seen that the impurities vary with the sources and separation methods of CO_2 streams. The data are provided by IEA GHG, based on CO_2 quality recommended for the evaluation under the COORETEC study for fossil-fueled power plants (Kather, 2009). Reductive impurities such as H_2, H_2S and CH_4 are present in pre-combustion streams while oxide impurities, including nitrogen oxides (NO_x) and sulfur oxides (SO_x), are present in oxyfuel and post-combustion streams. Although the composition spectra may vary, the types of impurities in the other scenarios would be largely the same, as long as the CO_2 is from burning fossil fuels (IEAGHG. 2011).

Table 2.4 Compositions of CO_2 streams (Kather, 2009)

Component	Pre-combustion		Post-combustion			Oxyfuel		
	Selexol	Rectisol	Comp. 1	Comp. 2	Comp. 3	Comp. 1	Comp. 2	Comp. 3
CO_2 (vol %)	97.95	99.7	99.93	99.92	99.81	85.0	98.0	99.94
O_2 (vol %)	-	-	0.015	0.015	0.03	4.70	0.67	0.01
N_2 (vol %)	0.9	0.21	0.045*	0.045*	0.09*	5.80	0.71	0.01
Ar (vol %)	0.03	0.15				4.47	0.59	0.01
H_2O (ppmv)	600	10	100	100	600	100	100	100
NOx (ppmv)	-	-	20	20	20	100	100	100
SO_2 (ppmv)	-	-	10**	10**	20**	50	50	50
SO_3 (ppmv)	-	-				20	20	20
CO (ppmv)	400	400	10	10	20	50	50	50
H_2S+COS(ppmv)	100	100	-	-	-	-	-	-
H_2	1 vol%	20 ppm	-	-	-	-	-	-
CH_4 (ppmv)	100	100	-	-	-	-	-	-
NH_3 (ppmv)	-	-	-	50	-	-	-	-
CH_3OH (ppmv)	-	200	-	-	-	-	-	-

*Total concentration of N_2 + Ar

**Total concentration of SO_2 + SO_3

When it comes to the effects of the impurities on pipeline transport, Seevam et al. (2007) discussed the potential effects of impurities on pipeline transport, in terms of recompression distance, flow assurance, and phase equilibrium. Oosterkamp and Ramsen (2008) gave an overview for offshore pipelines and summarized a number of uncertainties related to impurities, including corrosion, degrading of non-steel materials, lack of measurement data, water solubility, modeling, chemical reactions between impurities, and allowable impurity levels for pipeline transport. Regarding the allowable impurity levels, there have been recommendations by the European project DYNAMIS on CO_2 quality for transporting of CO_2 streams from pre-combustion and post-combustion processes (de Visser et al., 2008; 2009). The considerations for setting the concentration limits are also given based on both technical and safety perspectives from the transport point of view. The impurity levels considered by IEA GHG are within or lower than the limits recommended by DYNAMIS, except for the levels of O_2, N_2 and Ar from oxyfuel combustion.

With regard to the subsurface side, the impact of H_2S co-injected with CO_2 has been successfully carried out for years (see, e.g., Bachu and Gunter, 2004; Bachu, 2008), with a major conclusion that H_2S is less reactive than SO_x and NO_x because of its lower acidity and low concentration level. Therefore, even relatively large amounts of co-injected H_2S prove not to be problematic for a CO_2 injection process. Besides, H_2S is not present in CO_2 streams from oxyfuel combustion.

Numerical studies on the effect of SO_2 on CO_2 injectivity have been performed by Palandri and Kharaka, (2005), Knauss et al.(2005), Xu et al. (2007), Bacon et al. (2009), Jacquemet *et al*. (2009), and Ellis et al. (2010). For example, Palandri and Kharaka (2005) presented simulation results for the effect of co-injected H_2S and SO_2 on CO_2 sequestration and concluded that, with an excess of sulfur relative to CO_2, the iron can be transformed almost entirely into siderite while the sulfur is converted predominantly into H_2SO_4. The applicability of this study, however, depends on the availability of the ferric iron in the formations. Brine acidification induced by SO_2 co-injected with CO_2 has been predicted based on numerical simulations (Ellis et al., 2010), where 1% SO_2 is predicted to decrease the pH of the brine from 4.6 in the case of

CO_2 alone to 1 – 2.5, depending on reaction and rate-limiting mechanisms. However, the effect of mineral buffering is not considered in the prediction.

Through these studies SO_2 is shown to result in dissolution of minerals in the injection zone and precipitation downstream, causing significant decrease of rock porosity and hence CO_2 injectivity (Xu et al., 2007). However, SO_2 is far less reactive when it is dry and the impact of SO_2 on the reduction of rock porosity and injectivity appears much smaller than previously thought (IEAGHG. 2011), because its contact with water is limited due to the formation of a desiccation or dry-out zone (*e.g.*, Gaus *et al.*, 2008; Pruess and Müller, 2009; Pruess, 2009) resulting from the injection operations where SO_2 migrates with CO_2 in an immiscible plume. IEAGHG (2011) also concluded that NO_x would also promote dissolution of minerals, but would not cause precipitations and reduction of rock porosity and that SO_x and NO_x increase dissolution of carbonate rocks and aluminosilicate rocks but the impact on the caprock integrity would not be significant since the concentration levels are relatively small.

Bachu et al. (2009 a, b) investigated chromatographic partitioning of impurities under CO_2 injection conditions. Although O_2 and Ar have not been investigated with regard to the partitioning phenomenon, IEAGHG (2011) proposed that Ar impurity may serve as a trace species for monitoring CO_2 leakage because noble gases including Ar have long been used in volcanic gas monitoring (e.g., Magro and Pennisi, 1991).

Sass et al. (2009) discussed a number of issues concerning storage of flue gas from oxy-fuel combustion, where CO_2 content is below 80%, including reduction of storage capacity and permeability by non-condensable gases, increase of injection pressure, reduction of injection lifetime due to precipitation of solids such as calcium sulphate, etc. However, no quantitative results are presented.

de Visser et al. (2009) pointed out that the presence of impurities in the CO_2 lowers the density of the CO_2 stream, and thus decreases the amount of CO_2 stored per unit volume of storage space. As a consequence, the storage efficiency decreases. IEAGHG (2011) quantitatively estimated that there is a maximum reduction of the storage capacity in a certain pressure range, where the capacity can drop to below 50% of the pure CO_2 cases. However, due to the compensation by increased viscosity the reduction of injectivity is smaller than that of storage capacity. IEAGHG (2011) also stated that the

higher buoyancy of impure CO_2 streams would reduce the efficiency of CO_2 dissolution in formation water and CO_2 trapping in rock pores, and thus reduce the security of CO_2 storage in the near to medium terms. The adverse effects on storage efficiency and security may be alleviated by increasing the depth of injection and storage.

Several other effects of various impurities on CO_2 include corrosion of well materials, hazardousness in the event of leakage, etc. Interested readers can refer to IEAGHG (2011) for a detail investigation about the effects of impurities on geological storage of CO_2.

To summarize, the most important effects of impurities on CO_2 geological storage are as follows.

First, the presence of non-condensable gases such as hydrogen (H_2), argon (Ar), N_2 and O_2 can significantly reduce the density of the CO_2 stream. Therefore, the low density of the injected CO_2 stream would lead to the inefficient utilization of pore space, reducing the amount of CO_2 that can be stored at a particular storage location.

Second, the presence of certain impurities such as hydrogen sulfide (H_2S), NO_x and SO_x can reduce the pH of the formation water and consequently affect porosity and permeability of the geological formations, which might impact CO_2 injectivity and caprock integrity.

2.7 Geochemical modeling

Carbon dioxide storage in a deep saline aquifer may lead to a variety of geochemical reactions concerning the injected CO_2 and impurities and the original brine and rock minerals (Kaszuba et al., 2003, 2005; Xu et al., 2004a; Gaus et al., 2005; Giammar et al., 2005; Knauss et al., 2005; Kharaka et al., 2006; Andre et al., 2007). Investigating these reactions in the laboratory is both difficult and time consuming because of the high temperatures and pressures required to replicate natural systems as well as the (often) slow reaction rates of minerals (Gunter et al., 1997; Kaszuba et al., 2003). Therefore, it is often more efficient to utilize computer modeling to investigate geochemical reactions.

Up to now, four kinds of models are basically available to simulate mineral-brine-CO_2 reactions: equilibrium, path of reaction, kinetic, and reactive transport models.

Mineral equilibrium models and path of reaction models are used to calculate equilibrium solid phases and solution compositions for a given set of reactants based on a data set of equilibrium constants and activity coefficients. Equilibrium models calculate only the final state. Path of reactions models also calculate transitional phases along the way. The reaction path is the course followed by the equilibrium system as it responds to changes in composition and temperature. The measure of reaction progress is the non-dimensional variable, which varies from zero to one from the beginning to end of the path. However, these models do not provide information on the amount of time it takes to reach equilibrium or transition states. In Kinetic models, the rates at which minerals dissolve into or precipitate from the equilibrium system are set by kinetic rate laws. In this class of models, reaction progress is measured in time. The rate of dissolution or precipitation in the calculation depends on the variables in the rate law: the reaction's rate constant, the mineral's surface area, the degree to which the mineral is under-saturated or supersaturated in the fluid, and the activities of any catalyzing and inhibiting species. Reactive transport models are a natural marriage (Rubin, 1983; Bahr and Rubin, 1987) of the local equilibrium and kinetic models with the mass transport models traditionally applied in hydrology and various fields of engineering (e.g., Bird et al., 1960; Bear, 1972). The model results reflect the kinetic rate constants taken to describe chemical reaction, as well as the hydrologic properties assumed for the medium.

Widely available geochemical modeling codes such as PATHARC (Hitchon 1996), PHREEQC (Parkhurst, 1995), SOLMINEQ (Kharaka et al. 1988), and Geochemists Workbench (Bethke 1996) have been used for equilibrium, path of reaction, and kinetic simulations of CO_2 storage in aquifers. Because these models have no transport components, these studies simulate closed-system batch conditions and do not take into account the migration of CO_2 through the aquifer (Gunter et al.1993, 1996, 1997). Studies using full-scale reactive transport codes to simulate the flow, dissolution, and reaction of CO_2 are just becoming available (e.g. Johnson et al. 2001; Xu et al. 2003). In addition, experimental studies are investigating the kinetics of mineral-brine-CO_2 reactions to refine and test model reliability (Kaszuba et al. 2003; Liu et al. 2003; Shao et al., 2010).

In terms of geochemical modeling related to CO_2 sequestration, various numerical investigations can be found in the literature. For example, Xu and Pruess (1998, 2001a); Xu et al. (2004b) have developed the Thermo-Hydraulic-Chemical (THC) code TOUGHREACT which combines geochemical reactions with multi-phase flow and used the simulator to investigate various kinds of issues related to CO_2 sequestration (Pruess, 2009; Puress et al., 2009; Xu et al., 2001a, 2003, 2004a, 2007). White et al. (2001) used reactive transport code CHEMTOUGH2 (White, 1995), a multi-component reactive flow code based on the porous media multi-phase mass and energy flow code TOUGH2 (Pruess, 1991) to evaluate mineral trapping of CO_2 in saline formations underlying the Colorado Plateau in the USA. They concluded that realistic estimates of the storage potential of such reservoirs can be obtained from these simulations.

A two-dimensional mathematical sedimentary basin of the Powder River Basin was used for the simulations to evaluate resident times in possible aquifer storage sites and migration patterns in the Powder River Basin of Wyoming (McPherson and Lichtner, 2001). These simulation results provided insight regarding the ultimate impact of permeability reductions versus permeability increases in the fracture zone associated with carbonate reactions. Gaus et al. (2003) performed PHREEQC 1D diffusive reactive transport simulations of dissolved CO_2 in the cap-rock of the Utsira aquifer (Sleipner project) and suggested a slight decrease in porosity at the lower section of the cap rock. Clauser (2003) and Kühn et al. (2006) developed the numerical simulator SHEMAT (i. e. a Simulator for HEat and MAss Transport) to address the different features of geothermal and geochemical problems such as dissolution of the species, reaction between the rock and the formation fluids, coupling of porosity and permeability.

Xu et al. (2004a) performed geochemical simulations with TOUGHREACT (Xu et al., 2004b) on three rock types to illustrate the mineral trapping capacity limitations. They concluded that mineral trapping can be comparable to the solubility trapping and the trapping capacity depends strongly on the mineral composition of the host rock. Furthermore, they found out that the addition of CO_2 mass as secondary carbonates to the solid matrix results in decreased porosity, which in turn adversely affects permeability and fluid flow in the aquifer.

Johnson et al. (2004) introduced a methodology using NUFT (Nitao, 1995), a simulator for non-isothermal, multi-component, multi-phase flow and reactive transport, to couple the geo-mechanical and geochemical effects on sequestration. They found out that intra-aquifer permeability structure controls the path of immiscible CO_2 migration by reducing vertical plume mobility and increasing it laterally, thus, enhancing the storage capacity. After 20 years, porosity and permeability have been reduced by 8 % and 22 %, respectively (due to magnesite precipitation).

The most relevant mineralogical transformations occurring in the cap rock were described by Gherardi et al. (2007) using batch simulations accompanied by 1D and 2D modeling. The effect of these geochemical processes on physical properties such as porosity was studied. The simulation results showed that the CO_2 leakage from the reservoir may have a strong influence on the geochemical evolution of the cap rock.

More recently, Fan (2010) developed an element-based formulation to include both equilibrium and kinetic reactions into the fully coupled system for reactive flow modeling. He also developed a new generic representation of reaction terms, allowing simultaneous modeling of homogeneous and heterogeneous reactions within or among phases (i.e., gas, liquid, water and solid phases). Gundogan et al. (2011) compared the three numerical codes, PHREEQC, GEM and TOUGHREACT with respect to brine-CO_2-rock reactions and concluded from their comparison that PHREEQC and GEM were generally in good agreement while TOUGHREACT gave diverging predictions on two models and attributed the discrepancies primarily to the differences in the thermodynamic databases and activity models. Thomas et al. (2012) investigated the sensitivity of the geochemical outcomes to several sub-models and suggested that the geochemical predictions are least sensitive to the choice of CO_2 activity coefficient sub-model, are moderately sensitive to the choice of CO_2 solubility sub-model, and are most sensitive to the choice of CO_2 fugacity coefficient sub-model. Wertz et al. (2012) developed a geochemical model for wellbore cement-caprock-reservoir interfaces and used the model to predict the mechanisms of cement chemical alteration due to its interaction with acid brine after the injection of supercritical CO_2 within reservoir rock and found that at the well-reservoir interface, the intrusion into the cement paste of acid brine accompanied by aqueous CO_2 leads to a moderate porosity decrease. Okuyama et al. (2013) used the TOUGHREACT

simulator to study the long-term geochemical change in a 2-dimensional, 2-layered model representing the underground geologic and hydrogeologic conditions of the Tokyo Bay area and found that the CO_2-water-rock interaction in the storage system (mainly in the reservoir) changes the properties of water in a mushroom-like CO_2 plume, which eventually leads to convective mixing driven by gravitational instability.

Other important modeling aspects of the long-term storage of CO_2 such as applicable equations of states (EOS), CO_2 solubility modules and effects of impurities, etc. are also investigated by various researchers such as Knauss et al. (2005), Zerai et al. (2006), Le Gallo et al. (2006), Worden (2006), Benezeth et al. (2007), Xu et al. (2007), Gaus et al. (2008), and Mito et al. (2008).

Chapter 3 Numerical simulation of multiphase Darcy-Forchheimer flow

In this chapter, first a new approach for the use of Type-II criterion for two-phase Forchheimer flow classification is proposed, and then a two-phase incompressible flow model in a non-deformable porous media is developed with the incorporation of the Forchheimer number to identify the transition between Darcy and Forchheimer flow regions. The proposed model is first validated with a semi-analytical solution (Wu, 2001) inspired from the Buckley-Leverett model with inertial effects. Then the model is used in the analysis of carbon dioxide (CO_2) injection into a deep saline aquifer.

3.1 Governing equations

Assuming the porous media is non-deformable with constant porosity θ and the fluid is incompressible, the conservation of mass for two-phase flow is expressed by the continuity equation as,

$$\frac{\partial(\theta\rho_\alpha S_\alpha)}{\partial t} = -\nabla\bullet(\rho_\alpha v_\alpha) + Q_\alpha \quad ; \ \alpha = w, n \tag{3.1}$$

where S_α is saturation for α phase, Q_α is source and sink term. In Equation (3.1) the wetting and non-wetting phases are distinguished by the subscripts "*w*" and "*n*" referring to water and oil (or CO_2 in this study), respectively. The relationship of fluid velocity v and pressure p for Forchheimer flow can be expressed as,

$$-\nabla\phi_\alpha = \frac{\mu_\alpha v_\alpha}{k\, k_r^\alpha} + \beta_\alpha\rho_\alpha v_\alpha |v_\alpha| \quad ; \ \alpha = w, n \tag{3.2}$$

where k_r^α is the relative permeability for α phase and k is the intrinsic permeability for the porous media. Inspired from the definition of the Forchheimer number, in this study we define the Forchheimer number for two-phase flow as,

$$f_\alpha = \frac{kk_r^\alpha}{\mu_\alpha}\beta_\alpha\rho_\alpha |v_\alpha| \quad ; \ \alpha = w, n \tag{3.3}$$

From Equations (3.2) and (3.3), we can obtain,

$$v_\alpha = -\left(\frac{k_r^\alpha k}{\mu_\alpha} \frac{1}{(1+f_\alpha)} (\nabla \phi_\alpha) \right) \quad ; \ \alpha = w, n \tag{3.4}$$

Combining Equations (3.1) and (3.4) we obtain,

$$\frac{\partial(\theta \rho_\alpha S_\alpha)}{\partial t} = \nabla \bullet (\rho_\alpha \frac{k_r^\alpha k}{\mu_\alpha} \frac{1}{1+f_\alpha} (\nabla \phi_\alpha)) + Q_\alpha \quad ; \quad \alpha = w, n \tag{3.5}$$

It can be seen from Equation (3.4) that Darcy flow is a special case of the Forchheimer flow Equation (3.5) where the Forchheimer number f_α is equal to zero. Therefore, the Forchheimer number in a flow domain can be compared to a critical Forchheimer number $(f_\alpha)_c$ to determine if the flow should be Darcy $\left(< (f_\alpha)_c\right)$ or Forchheimer $\left(\geq (f_\alpha)_c\right)$ flow. The Forchheimer coefficient in the Forchheimer number can be determined by experimental data through regression analysis based on Equation (2.4).

To solve Equation (3.5), three additional equations are needed as given below,

$$\begin{aligned} &S_w + S_n = 1 \\ &P_c = P_n - P_w \\ &P_c = P_c(S_w) \end{aligned} \tag{3.6}$$

where P_c is capillary pressure.

In this study, capillary pressure and relative permeabilities are assumed to depend on saturation only and these relations are expressed as,

$$\begin{aligned} &P_c = P_D S_{eff}^{-(1/\lambda)} \\ &k_r^w = \left(S_{eff}\right)^{(2+3\lambda)/\lambda} \\ &k_r^n = \left(1-S_{eff}\right)^2 \left(1-\left(S_{eff}\right)^{(2+\lambda)/\lambda}\right) \\ &S_{eff} = \frac{S_w - S_w^r}{1 - S_w^r - S_n^r} \end{aligned} \tag{3.7}$$

where P_D is the entry pressure, λ is pore size distribution index, S_{eff} is the effective saturation, S_w^r is irreducible saturation for water and S_n^r is irreducible saturation for non-wetting phase.

Due to diversity in geological formations and pore geometry of porous media matrix, there is variability in the definitions and correction formulas used for the

Forchheimer coefficient β for single phase analysis. A detailed review of this subject can be found in Li and Engler (2001) and Lopez-hernandez et al. (2004).

As for the multiphase flow, Geertsma (1974) is the first to develop an expression for the Forchheimer coefficient for two-phase flow, by stating that the permeability used in single phase flow should be replaced by the effective permeability for two-phase flow and the porosity used in single phase flow should be modified to be the product of porosity and the corresponding phase saturation with the equation for non-wetting phase Forchheimer coefficient given as,

$$\beta_n = \frac{0.005}{\left(kk_r^n\right)^{0.5}\left(\theta\left(1-S_w\right)\right)^{5.5}} = \frac{0.005}{\left(kk_r^n\right)^{0.5}\left(\theta S_n\right)^{5.5}} \tag{3.8}$$

Several authors (Cornell and Katz, 1953; Geertsma, 1974; Evans et al., 1987; Evans and Evans, 1988; Whitney, 1988) collected a large variety of single- and two-phase flow data to develop a more unified definition of Forchheimer flow coefficient. Based on these studies and realizing the importance of tortuosity τ, Liu et al. (1995) recommended a more satisfactory correlation described as,

$$\beta = \frac{2.923*10^{-6}\tau}{(k)(\theta)} \tag{3.9}$$

with β and k expressed in SI units.

Recently, Ahmadi et al. (2010) further adapted Liu's equation to two-phase conditions yielding,

$$\beta_\alpha = \frac{2.923*10^{-6}\tau}{\left(kk_r^\alpha\right)(\theta)} \quad ; \ \alpha = w,\ n \tag{3.10}$$

However, Equation (3.10) does not include a saturation term in the denominator, as Equation (3.8) does. Based on their experiments results, Evans and Evans (1988) concluded: "a small mobile liquid saturation, such as that occurring in a gas well that also produces water, may increase the non-Darcy flow coefficient by nearly an order of magnitude over that of the dry case." Therefore, it is necessary and physically sound to include the saturation term in the denominator of the correction equation, as Equation (3.8) does. Otherwise, the direct change in the Forchheimer flow coefficient due to saturation difference cannot be precisely described if one uses an equation such as

Equation (3.10). Therefore, in this study we adopt a correction based on the following equation which incorporates the direct impact of saturation on the Forchheimer flow coefficient

$$\beta_\alpha = \frac{C_\beta \tau}{\left(kk_r^\alpha\right)\left(\theta S_\alpha\right)} \qquad ;\ \alpha = w,\ n \tag{3.11}$$

where C_β is a numerical constant having the unit of a length (e.g., m) and τ is selected as 1.9, which is based on experimental data (Wahyudi et al., 2000). It must be emphasized that β_α is a user-defined site specific constant, but its choice does not impose any restrictions on the numerical solution that is developed here.

3.2 Determination of critical Forchheimer number

As for the criterion for single phase transition between Darcy flow and Forchheimer flow, a detailed discussion can be found in the literature (e.g., Chilton et al., 1931; Green et al., 1951; Ergun, 1952; Ma et al., 1993; Andrade et al., 1999; Zeng and Grigg, 2006); however, there is very few discussion on the criterion to be used for multiphase transition. The determination of the critical value for the transition is usually based on experimental data, with some based on theoretical derivation for single phase flows (Ahmed et al., 1969; Ma et al., 1993; Andrade et al., 1999). Most of the experimental data are from gas flooding experiments (e.g., Chilton et al., 1931; Green et al., 1951) with few from water flooding experiments (e.g., Sobieski and Trykozko, 2012). For typical evaluation of the transition usually a curve for the friction factor ($-\frac{(\nabla\phi)}{\beta\rho v|v|}$) versus the Forchheimer number (e.g., Equation (2.4)) is plotted and the critical value for the transition between Darcy and Forchheimer flows is selected based on the Forchheimer number when the linear relationship between the two variables begins to deviate.

Since Darcy flow behavior is characterized by Equation (2.3) and Forchheimer flow is characterized by Equation (2.4), if Equation (2.3) and (2.4) can be transformed to two separate formulas, each of which has a linear relationship between the independent variable (x) and the dependent variable (y) with the same definition for x and y, then

mathematically and physically, the intersection of the two lines would be the point where the flow behavior would begin to transition between the two flow regimes. In this study we propose a new approach to more accurately determine the critical value for single phase condition and then extend this approach to two-phase flows. The proposed method is based on the transformed form of Equation (2.3) and (2.4) expressed as,

$$\begin{aligned} Darcy: \quad & -\frac{(\nabla\phi)}{\beta\rho v|v|} = \frac{1}{f} \\ non-Darcy: \quad & -\frac{(\nabla\phi)}{\beta\rho v|v|} = \frac{1}{f} + 1 \end{aligned} \tag{3.12}$$

where f is described by Equation (2.2). One may argue that the Forchheimer coefficient β is not defined in the Darcy formula in Equation (3.12). However, the Forchheimer coefficient β is a measure of the properties of porous media and the fluid and it will be a constant given the specified porous media type and fluid type. More importantly, the introduction of the Forchheimer coefficient β will not change the characteristics of linear relationship between pressure gradient and flow velocity. Herein, the Forchheimer coefficient is introduced in order to have a consistent formula for both Darcian and Forchheimer flow as is shown in Equation (3.4) and (3.5). Furthermore, including β in the Darcy formula in Equation (3.12) ensures that the Forchheimer number in both Darcy and Forchheimer formulas have a comparable basis and the two formulas in Equation (3.12) can be used to determine the critical Forchheimer number. Actually, we can also multiply the two formulas in Equation (3.12) by a factor of β and use the resultant two formulas to determine the critical Forchheimer number. The resultant Darcy formula after the multiplication will not have the β term and be essentially the same as Equation (2.3). Thus the two formulas in Equation (3.12) have a linear relationship between the friction factor and the reciprocal of the Forchheimer number and the introduction of β into the Darcy formula for consistency and comparison would not change the flow behavior. So it can be used to determine the critical Forchheimer number.

According to Equation (3.12), when the experimental data are available, a regression curve can be plotted for the relation between friction factor and the Forchheimer number to obtain a rough critical value. Then we can fit a curve for the friction factor versus the reciprocal of the Forchheimer number with the intercept set to

be zero for the data within Darcy regime. For the data within Forchheimer regime, a linear regression is conducted for the friction factor versus the reciprocal of the Forchheimer number. The intersection of the two regression lines is the estimated point for the transition.

Equation (3.12) can be easily expanded to two-phase flow with all the variables replaced by the corresponding phase-based variables. The resulting equations are as follows,

$$\begin{aligned} Darcy: \quad & -\frac{(\nabla \phi_\alpha)}{\beta_\alpha \rho_\alpha \mathrm{v}_\alpha |\mathrm{v}_\alpha|} = \frac{1}{f_\alpha} \\ non-Darcy: \quad & -\frac{(\nabla \phi_\alpha)}{\beta_\alpha \rho_\alpha \mathrm{v}_\alpha |\mathrm{v}_\alpha|} = \frac{1}{f_\alpha} + 1 \end{aligned} \tag{3.13}$$

where f_α is described by Equation (3.3). We note that both β_α and f_α are functions of saturation for α phase. Therefore, in multiphase flow, for each phase there is a critical value for transition for a specific saturation.

With the method described above and the flooding data provided by Sobieski and Trykozko (2012), we determine the critical Forchheimer number for water at different saturation values. For example, based on Equation (3.13), a typical plot is shown in Figure 3.1, for the water phase whose saturation is 0.95, to determine the reciprocal of the Forchheimer number with a value of 4.825 (as is shown in the figure); therefore, the critical Forchheimer number $(f_w)_c$ is determined as 0.207. The same procedure can be used to determine the critical Forchheimer number for water at different saturation values and the only difference is to update both β_α and f_α with different saturation levels. As for the CO_2, since no flooding experiments have been done yet, the data for the velocity and pressure differences obtained by Sobieski and Trykozko (2012) are used to determine the critical Forchheimer number for CO_2 at different saturation values with the same procedure shown in Figure 3.1.

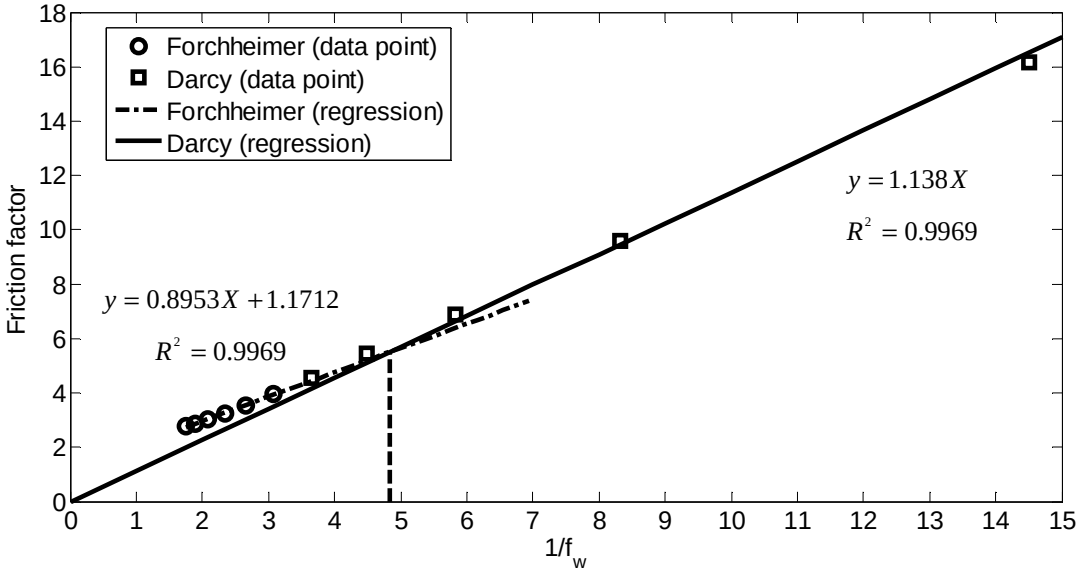

Figure 3.1 A typical plot to determine the critical Forchheimer number for the water phase whose saturation is 0.95 (in the figure, x axis represents the reciprocal of the Forchheimer number defined by Equation (3.3) while the y axis represents the Friction factor defined as $-\frac{(\nabla\phi)}{\beta\rho v|v|}$; circle and square represent the experiment data points for Forchheimer and Darcy flow, respectively; the dash dot line and solid line are the regression lines for Forchheimer and Darcy flow, respectively; the two lines intercept where 1/fw=4.825, thus $\left(f_w\right)_c$ is 1/4.825=0.207)

With the procedure proposed above, the critical Forchheimer numbers for water and CO_2 at several discrete saturation values are determined and shown in Figure 3.2 with water's critical Forchheimer number $\left(f_w\right)_c$ a range of (0.207, 0.532) and CO_2's a range of (2.743, 29.720). The critical Forchheimer number for water has a negative correlation with water saturation, which is physically reasonable because it would be more and more difficult for water to transport in a non-Darcian manner if there is less and less water in the control volume and vice versa. The same phenomenon holds for the CO_2 case, the lower the saturation, the higher the critical Forchheimer number and vice versa (it needs to be noted that CO_2 saturation S_n is equal to $(1-S_w)$ in Figure 3.2). Furthermore, it is important to emphasize that in this study the residual non-wetting phase saturation is set to be 0.05 and thus the maximal wetting phase saturation is 0.95. Therefore, the critical Forchheimer number for water phase with a saturation of 0.95 is equivalent to the critical Forchheimer number for saturated water in a single phase case. A comparison can

show that the critical Forchheimer number for water has a similar order of magnitude with the results provided by many researchers (Green et al., 1951; Ma et al., 1993; Andrade et al., 1999; Zeng and Grigg, 2006) whose results show that the critical Forchheimer number for a single saturated phase has a range of (0.005, 0.2). The wide range can be attributed to the difference in the methods (experimental or theoretical) and the type of porous media used (unconsolidated or consolidated; ordered or disordered).

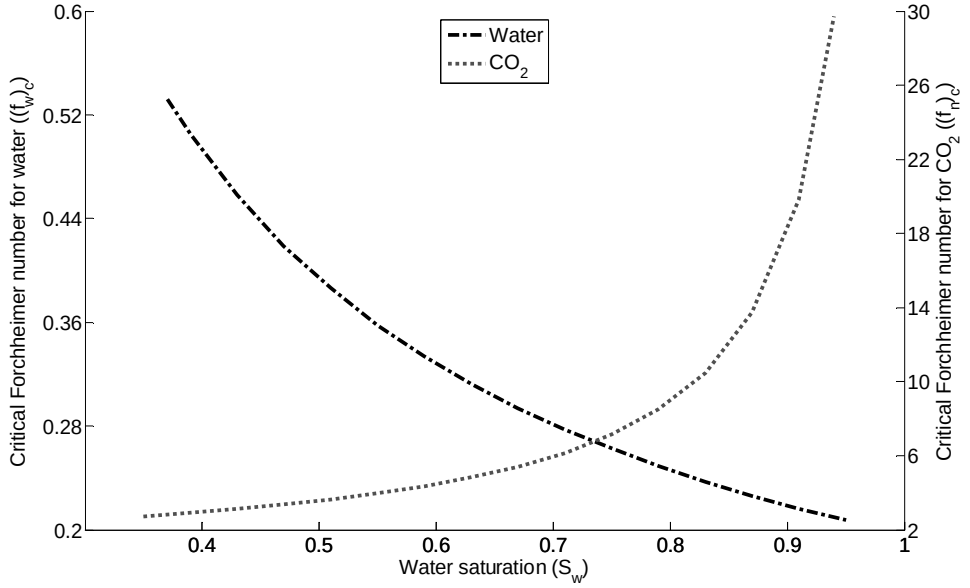

Figure 3.2 Critical Forchheimer number for H_2O and CO_2 at different saturation values

3.3 Numerical models

3.3.1 Control volume finite difference method (CVFD)

Equations (3.5) and (3.6), together with appropriate boundary and initial conditions, comprise a complete boundary value problem. Spatial discretization of this system of equations is realized using a control volume finite difference method (Abou-Kassem, 2006) and an upwind scheme to estimate the mobilities (defined as $kk_r^{\alpha} / \mu_{\alpha}$). Temporal discretization is performed employing a first-order backward differencing method. In order to incorporate the gravity effects and capillary effects, in this study following the definition proposed by Karimi-Fard and Firoozabadi (2003), we define a flow potential for each phase ϕ_{α} and the capillary pressure potential ϕ_c as:

$$\phi_\alpha = p_\alpha + \rho_\alpha gz \;\; ; \quad \alpha = w,\ n$$
$$\phi_c = \phi_n - \phi_w = p_c + (\rho_n - \rho_w)gz$$

where z is the elevation in the vertical direction (z being positive upward) and ϕ_c includes both the gravity and capillary effects. After that, we select S_n and ϕ_w as the primary variables, and for 1-D case, Equations (3.5) and (3.6) can be transformed into,

$$\begin{aligned}
&\theta S_n^{t+1} + a(\phi_{wi+1}^{t+1} - \phi_{wi}^{t+1}) - b(\phi_{wi}^{t+1} - \phi_{wi-1}^{t+1}) = \theta S_n^t - \left(\frac{Q_w}{\rho_w}\right)^t \Delta t \\
&\theta S_n^{t+1} - \left(c(\phi_{wi+1}^{t+1} - \phi_{wi}^{t+1}) - d(\phi_{wi}^{t+1} - \phi_{wi-1}^{t+1})\right) \\
&\quad - \left(\left(\frac{\partial \phi_c}{\partial S_n}\right)_{i+\frac{1}{2}} c(S_{ni+1}^{t+1} - S_{ni}^{t+1}) - \left(\frac{\partial \phi_c}{\partial S_n}\right)_{i-\frac{1}{2}} d(S_{ni}^{t+1} - S_{ni-1}^{t+1})\right) = \theta S_n^t + \left(\frac{Q_n}{\rho_n}\right)^t \Delta t
\end{aligned} \tag{3.14}$$

where $\left(\frac{\partial \phi_c}{\partial S_n}\right)_{i\pm\frac{1}{2}}$ is evaluated using an upwind scheme and coefficients a, b, c and d are expressed as

$$\begin{aligned}
a &= \left[\frac{\Delta t}{(\Delta x)^2}\frac{kk_r^w}{\mu_w}\frac{1}{1+f_w}\right]_{i+\frac{1}{2}} \qquad b = \left[\frac{\Delta t}{(\Delta x)^2}\frac{kk_r^w}{\mu_w}\frac{1}{1+f_w}\right]_{i-\frac{1}{2}} \\
c &= \left[\frac{\Delta t}{(\Delta x)^2}\frac{kk_r^n}{\mu_n}\frac{1}{1+f_n}\right]_{i+\frac{1}{2}} \qquad d = \left[\frac{\Delta t}{(\Delta x)^2}\frac{kk_r^n}{\mu_n}\frac{1}{1+f_n}\right]_{i-\frac{1}{2}}
\end{aligned} \tag{3.15}$$

With appropriate boundary conditions as defined later in Section 3.4 and the results known at time step t, from Equation (18), we can assemble a system of equations $\mathbf{AX} = B$, where x = $\left[S_{n1}^{t+1}, \cdots S_{ni}^{t+1}, \cdots S_{nm}^{t+1}, \phi_{w1}^{t+1} \cdots \phi_{wi}^{t+1}, \cdots \phi_{wm}^{t+1}\right]^T$, **B** is the right hand side of Equation (3.14), and **A** is a $(2m \times 2m)$ stiff matrix assembled from the left hand side with *m* as the number of nodes in the *x*-direction. If the axes can be aligned with the principal directions for the permeability tensor, then the above discretization method can be easily extended to 2- and 3-D cases.

3.3.2 Treatment of the nonlinearity

The nonlinearity in Equation (3.14) is induced by the Forchheimer number, the relative permeabilities and the derivative of capillary pressure potential over saturation.

This strong nonlinearity needs to be solved in an iterative manner. To deal with the nonlinearity, in this study we employ Picard iteration inside each time step. The Picard method is proved to be able to produce the most satisfactory results (Ahmadi et al., 2010).

Another important issue is the choice of the node position to estimate the relative permeability, the Forchheimer number and the derivative of capillary pressure potential over saturation during the assembly of the stiff matrix and during the evaluation of the velocities at the interface between two grid-blocks. In order to ensure physically meaningful results, classically an upwind scheme is used to evaluate the relative permeability, which involves estimating the relative permeabilities using the value of saturation on the node located upwind to the flow with regard to the interface. As for the Forchheimer number and the derivative of capillary pressure over saturation, a similar upwind technique should be adopted since both are dependent on saturation.

3.3.3 The algorithm

The system of nonlinear equations $\mathbf{AX} = B$ can be solved by an iterative procedure, such as the Picard method. The numerical algorithm shown in Figure 3.3 is employed to solve Equation (3.14). In this process several points need to be emphasized:

i. For the first iterative step of the current time step, **X** and other related variables in the last time step are used to update all the coefficients including a, b, c, d, $d\phi_c / dS_n$, f_w, f_n and all the elements in the right hand side **B;**

ii. For the second and thereafter iterations, **X** and other related variables in the last iterative step are used to update all the coefficients including a, b, c, d, $d\phi_c / dS_n$, f_w and f_n, but not the elements in **B** because the right hand side term **B** is based on the variables in the last time step and don't need to be updated except for the first iterative step.

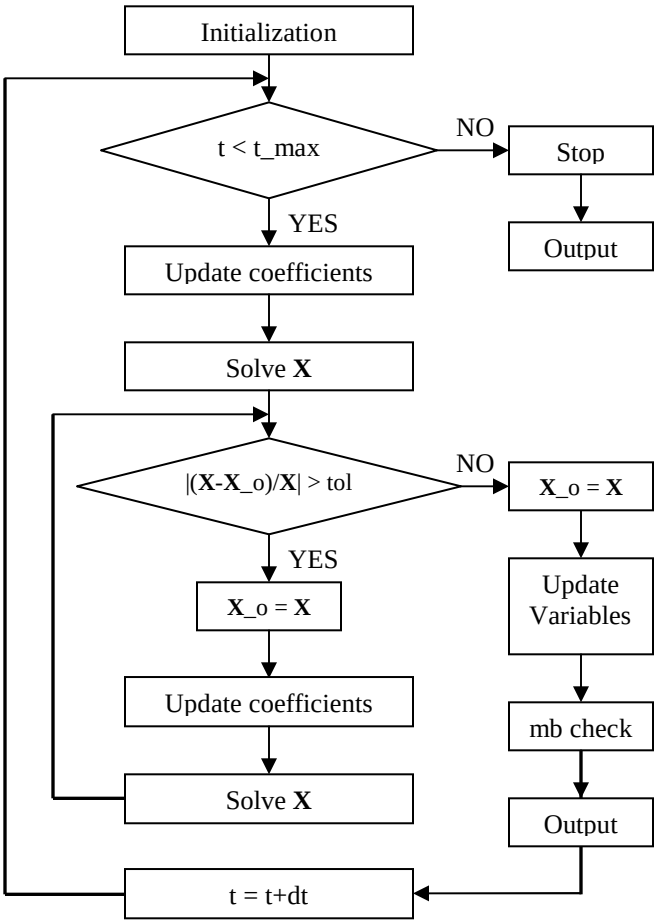

Figure 3.3 Flowchart for the numerical algorithm for Equation (3.14)

3.3.4 Mass balance analysis

In general, there are two mass balance checks, one of which is called the incremental mass balance check that is used to check the mass balance over a time step, and the other is called the cumulative mass balance check which is used to check the mass balance from the initial conditions up to the current time step. The latter check tends to smooth errors that occur over all the previous time steps; therefore, it is less accurate than the first one. Usually, a mass balance check is defined as the ratio of the accumulated mass to the net mass entering and leaving the domain boundaries, including wells. For CVFD methods, the equations for mass balance checks are

$$I_\alpha = \frac{\sum_{i=1}^{m} V_i \theta [S_{\alpha i}^{\ t} - S_{\alpha i}^{\ t-1}]}{\sum_{i=1}^{m} \Delta t_t (Q_{\alpha i}^{\ t} + \sum_{l \in \Gamma} q_{\alpha l,i}^{\ t})} \qquad ; \alpha = w,\ n$$

$$C_\alpha = \frac{\sum_{i=1}^{m} V_i \theta [S_{\alpha i}^{\ t} - S_{\alpha i}^{\ 0}]}{\sum_{j=1}^{t} \Delta t_j \sum_{i=1}^{m} (Q_{\alpha i}^{\ j} + \sum_{l \in \Gamma} q_{\alpha l,i}^{\ j})} \qquad ; \alpha = w,\ n \tag{3.16}$$

where Γ is the boundaries of the domain, *m* is the number of the nodes, *t* is the number of time steps, Q is discharge for pumping or injecting wells and q is the flow rate through the boundaries. For Q and q, they are set to be positive if entering the domain while negative if leaving the domain.

3.3.5 Darcy-Forchheimer flow

In this study Darcy-Forchheimer flow is defined as the flow incorporating the transition between Darcy and Forchheimer flows. The transition is realized by comparing the Forchheimer number in Equation (3.3) at each node for each phase relative to the critical Forchheimer number shown in Figure 3.2. If the Forchheimer number f_α at a specific point is less than the corresponding critical Forchheimer number $(f_\alpha)_c$ for the corresponding saturation, then the flow should be Darcian at this point. Therefore, f_α needs to be set to zero to account for the Darcy flow. In this case, an extra step after "update coefficients" in Figure 3.3 is needed to account for the transition between Darcy and Forchheimer flow. If the Forchheimer number f_α at a specific point is larger than the corresponding critical Forchheimer number $(f_\alpha)_c$ for the corresponding saturation, then f_α would remain the same value to account for the Forchheimer flow. The numerical treatment is described by the following equation:

$$f_\alpha = \begin{cases} 0\ , \text{ if } \ f_\alpha < (f_\alpha)_c & \text{Darcy flow} \\ f_\alpha, \text{ if } \ f_\alpha > (f_\alpha)_c & \text{Forchheimer flow} \end{cases}$$

Therefore, numerically, if f_α is positive, then the flow is of Forchheimer type; if f_α is zero, then the flow is Darcian.

3.4 Model verification

Validation of our model is realized by comparison with a semi-analytical solution of Buckley-Leverett problem as a special case. In fact, the classical Buckley-Leverett problem is for one-dimensional flow of two incompressible, immiscible fluids in homogeneous non-deformable porous media without considering the effect of capillary pressure in the Darcy regime. Its semi-analytical solution can be further extended to the case for which inertial effect is considered (Wu, 2001; Ahmadi et al., 2010).

3.4.1 Analytical solution for Forchheimer flow

For the derivation of the semi-analytical solution to Buckley-Leverett problem, the following flow conditions are assumed: (i) Both fluids are incompressible and the porous medium is non-deformable; (ii) Capillary pressure effect is negligible; (iii) Gravity effect is negligible; and, (iv) The flow is along 1-D homogeneous domain with a constant cross-sectional area (A).

The mass and momentum conservation equations are presented by Equations (3.1) and (3.2) without the source/sink term. In order to complete the mathematical description of the problem, initial and boundary conditions are specified as,

$$S_w|_{x=0}^{t=0} = S_{wi}; \quad v_n|_{x=0}^{t} = 0; \quad v_w|_{x=0}^{t} = q/A \tag{3.17}$$

The last condition states that the wetting fluid, such as water, is continuously injected at a known constant flow rate, q, at the inlet face (x=0).

To derive the semi-analytical solution, the concept of fractional flow is used to simply the governing equation (3.1) in terms of saturations only. The fractional flow can be written as

$$F_\alpha = \frac{v_\alpha}{v_w + v_n} = \frac{v_\alpha}{v_t} \qquad \alpha = w,\ n$$
$$v_t = v_w + v_n \tag{3.18}$$

With the condition P_c=0, substituting Equation (3.18) into Equation (3.2) leads to the following expression for the fractional flow for water phase

$$F_w = \frac{-a + (a^2 + 4v_t b(\frac{\mu_n}{k_r^n k} + \rho_n \beta_n v_t))^{0.5}}{2bv_t} \tag{3.19}$$

where $a = \frac{\mu_w}{k_r^w k} + \frac{\mu_n}{k_r^n k} + 2\rho_n \beta_n v_t ; \quad b = \rho_w \beta_w - \rho_n \beta_n$

From Equation (3.19), it can be seen that F_w is dependent on saturation only for a given injection rate (a constant total velocity) and given fluid properties. Therefore, the water phase mass balance equation can be transformed to,

$$\theta \frac{\partial (S_w)}{\partial t} = -\frac{\partial v_w}{\partial x} = -v_t \frac{\partial F_w}{\partial x} = -v_t \frac{dF_w}{dS_w} \frac{\partial S_w}{\partial x} = -\frac{q}{A} \frac{dF_w}{dS_w} \frac{\partial S_w}{\partial x} \qquad (3.20)$$

Equation (3.20) is the equation for non-Darcy immiscible two-phase displacement and has the same form as the classical Buckley-Leverett equation (Buckley and Leverett, 1942). Before solving the Buckley-Leverett equation, one could follow the movement of the saturation front into the column in any number of ways. If one decides to monitor the position of a particular unchanging value of saturation and is therefore interested in:

$$\frac{DS_w}{Dt} = \frac{\partial S_w}{\partial t} + \frac{dx}{dt} \frac{\partial S_w}{\partial x} = 0 \qquad (3.21)$$

A comparison of this equation with Equation (3.20) indicates that one can achieve this situation if one follows the value of saturation with a constant speed of,

$$\frac{dx}{dt} = \frac{q}{\theta A} \frac{dF_w}{dS_w} \qquad (3.22)$$

Actually, Equation (3.20) is a hyperbolic transport equation which is classically solved using the method of characteristics. To obtain a physically reasonable analytical solution, one must impose the requirement that there must be a shock front at which there is a discontinuity in the S_w function. Classically, the Welge tangent method (Welge, 1952) is used to determine the constant shock front saturation and its location. Upstream of the shock, the saturation profile is evolving according to Equation (3.22), while downstream of the shock the initial saturation profile is preserved.

3.4.2 Comparison with numerical simulations

The system of equations is solved numerically with the numerical method presented in Section 3.3 for a 1D homogeneous porous medium without considering capillary effects. Results are compared to those obtained analytically using the Buckley-Leverett approach presented in Section 3.4.1. The comparison was carried out with the

physical parameters of Table 3.1 and the constitutive equations presented in Section 3.1. The evolution of the water saturation profile obtained by direct simulation (using a one-dimensional version of the code with imposed flow rate at the inlet face) and by the analytical solution shows a very good agreement as indicated in Figure 3.4. This result validates our numerical model for the particular case of 1D two-phase inertial flow in homogeneous and incompressible porous media without capillary pressure.

Table 3.1 Parameters for inertial flow in 1D homogeneous porous media

k	C_β	λ	S_w^r	S_n^r	ρ_w	ρ_n	μ_w	μ_n	v_t	τ
(m^2)	(m)				(kg m^{-3})	(kg m^{-3})	(Pa s)	(Pa s)	(m s^{-1})	
2e-9	1.52e-5	3.86	0.2	0.2	994	479	1e-3	5e-3	5e-5	1.9

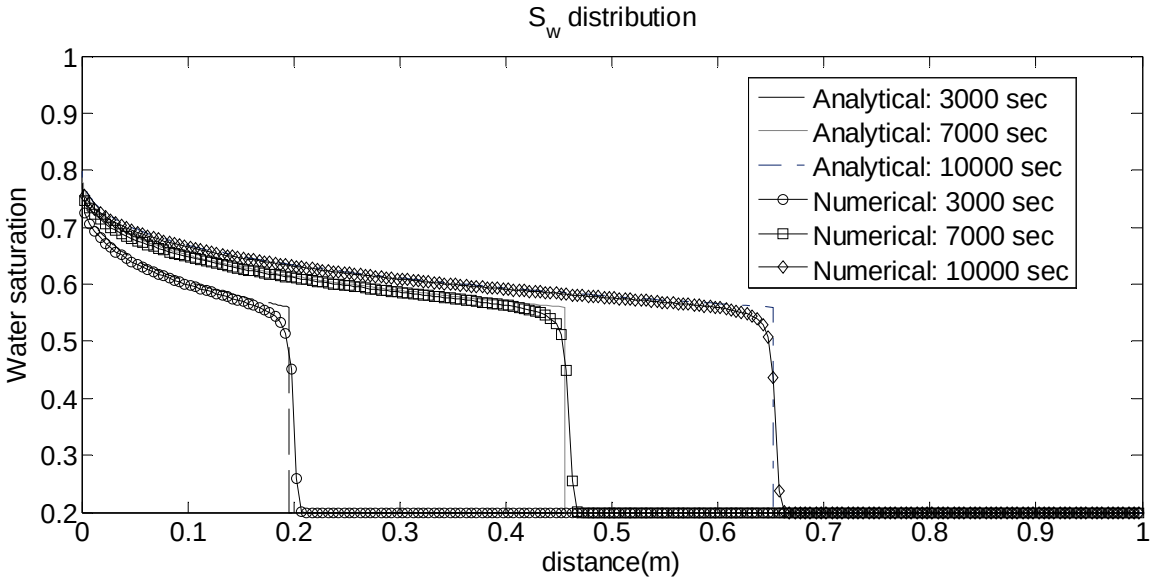

Figure 3.4 Comparison of saturation profiles of numerical solution with analytical solution

3.5 Application of Darcy-Forchheimer flow in a 2-D domain

The Forchheimer flow condition commonly occurs in near-wellbore area due to the smaller seepage area and high flow velocity. However, currently the Forchheimer effect has not been well accounted for in the numerical simulation of multiphase flow, especially in the process of CO_2 storage in deep saline aquifers. Recently, Mijic and Laforce (2010) studied the salt precipitation during CO_2 injection for an inertial flow regime and concluded that it is necessary to include nonlinear flow behavior in near-

wellbore area. Therefore, the model presented in Section 3.1 and 3.3 is applied to analyze the Forchheimer flow behavior due to CO_2 injection into a two-dimensional deep saline aquifer in this paper. During the analysis, the transition between Darcy and Forchheimer flows is achieved using the critical Forchheimer number presented in Figure 3.2 and the method proposed in Section 3.3.5. In addition, the fluids are assumed to be incompressible, immiscible while porous media non-deformable.

In the application problem, a constant flow rate of CO_2 (10^{-3} m^3/s per meter normal to the 2D domain) is continuously injected into the middle bottom (at the node with (x, z) equal to (16, 1)) of a deep saline aquifer with a depth of 800 m at the bottom boundary. The injection rate is determined by considering that a standard size 1,000-MW coal-fired power plant produces CO_2 at a rate approximately 350 kg/s (Hitchon, 1996), equivalent to 0.73 m^3/s CO_2. The CO_2 emitted would require a field about 730 meters in width (10^{-3} m^3/s per meter x 730 m =0.73 m^3/s). The domain and boundary conditions and parameter values used here are shown in Figure 3.5 and Table 3.2 and 3.3. During the simulation at the end of each time step before outputting the results, the incremental and cumulative mass are checked to make sure that the mass conserving ratios in Equation (3.16) are well under control (less than 0.1% for this study) for each phase. Since this study focuses on the Forchheimer effect of CO_2 near the wellbore area and the applicability of the method proposed here, the simulation time is in terms of hours, instead of years.

3.5.1 Results for Darcy-Forchheimer flow

Before presenting the results for Darcy-Forchheimer flow in 2D domain, it needs to be noted that there are four Forchheimer numbers when expanding Equation (3.14) to 2D case assuming the principal directions for the permeability can be aligned with the principal axes. These four numbers are noted as f_{wx} (for wetting phase in the x-axis direction), f_{nx} (for non-wetting phase in the x-axis direction), f_{wz} (for wetting phase in the z-axis direction) and f_{nz} (for non-wetting phase in the z-axis direction). Furthermore, it is important to note that all Forchheimer numbers and velocities are values evaluated at the individual interface between its two neighboring central nodes while all the other variables such as saturation and pressure are evaluated as values of central nodes. Since the node spaces in the x- and z-directions are both 1 meter, the node index is also the

distance from the two axes x and z, for example, the injecting node is in column 16 and row 1 and the distance from the injecting well to x and z axis happens to be 1 and 16 meters, respectively.

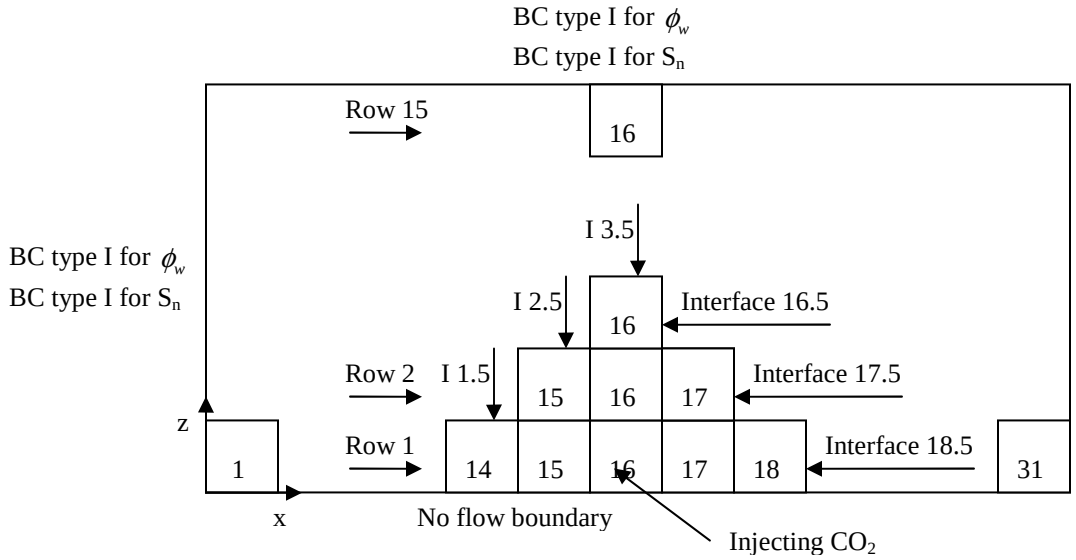

Figure 3.5 Model domain and boundary conditions (to represent a node, e.g., the injecting node (in Column 16 and Row 1) can be expressed as node (16, 1); for an interface, the east and north interfaces of the injecting node can be represented as (16.5, 1) and (16, 1.5), respectively)

Table 3.2 Parameters for inertial flow in 2D homogeneous porous media

k	C_β	λ	S_w^r	S_n^r	P_D	ρ_w	ρ_n	μ_w	μ_n	θ
(m^2)	(m)				(Pa)	(kg m^{-3})	(kg m^{-3})	(Pa s)	(Pa s)	
2e-9	1.52e-4	3.86	0.35	0.05	10000	994	479	7.43e-4	3.95e-5	0.37

CO_2 saturation profiles are shown in Figure 3.6, from which it can be seen that CO_2 spread to the right and left hand side in a symmetric way. Also, there is more CO_2 spread along the x direction than the vertical direction (gravitational effects). In addition, a high-saturation profile is observed near the injecting node (16, 1), which is due to the additional friction caused by the inertial effect near the injecting node. This point can be verified by analyzing the results for f_{nx} and f_{nz} demonstrated in Figures 3.6.

Table 3.3 Modeling parameters

Properties	***Values***	**Comment**	
Boundary condition			
Water potential at x=0.5 m	ϕ_w = 8 M Pa, BC Type I	Left boundary	
Water potential at x=31.5 m	ϕ_w = 8 M Pa, BC Type I	Right boundary	
Water potential at z=0.5 m	No flow boundary	Bottom boundary	
Water potential at z=15.5 m	ϕ_w = 8 M Pa, BC Type I	Top boundary	
CO_2 saturation at x=0.5 m	S_n = 0.1, BC Type I		
CO_2 saturation at x=31.5 m	S_n = 0.1, BC Type I		
CO_2 saturation at z=0.5 m	No flow boundary		
CO_2 saturation at z=15.5 m	S_n = 0.1, BC Type I		
CO_2 injecting rate @ (16,1)	$1*10^{-3}$ m^3/s	Per meter normal to the 2D domain	
Initial condition			
Water saturation	S_w = 0.9	Saturated with water initially	
NWP saturation	S_n = 0.1		
Water pressure	ϕ_w = 8 M Pa		
Space discretization		**Time discretization**	
Domain size, Length	L=31 m	Simulation time	T= 9000 s
Domain size, Depth	W=15 m	Time step size	dt=1 s
Domain size, Width	1 m		
Space step size	dx =dz=1 m		

It can be seen from Figure 3.6 that, the injecting node's eastern and western interfaces have a Forchheimer number larger than the critical Forchheimer number (with the f_{nx} remaining positive to account for the Forchheimer flow) at time 500 seconds, which implies that CO_2 flowing out from the injecting node is of Forchheimer flow. At time 1000 seconds, the Forchheimer regime has expanded to the three neighboring nodes of node (16, 1). At time 4000 seconds this region has further expanded to an area covering seven nodes (each row has three nodes for the first two rows and one in the third row). As for the upper interface of each node, the transition behavior can be found in Figure 3.6 as well. The injecting node's upper interface has a vertical Forchheimer number (f_{nz}) larger than the critical Forchheimer number at time 500 seconds. The Forchheimer region continues to grow with time as well. It is also easy to observe that the region where CO_2 tend to accumulate matches well with the Forchheimer flow regime. From Figure 3.6, we can also observe that the Forchheimer region in the vertical direction expands in favor of the x direction over the vertical direction. This can be explained by that the buoyancy effects caused by the density difference between CO_2 and water would result in vertical CO_2 velocity larger than horizontal velocity, which would cause a larger

vertical Forchheimer number, indicating that the Forchheimer effect is stronger vertically than horizontally.

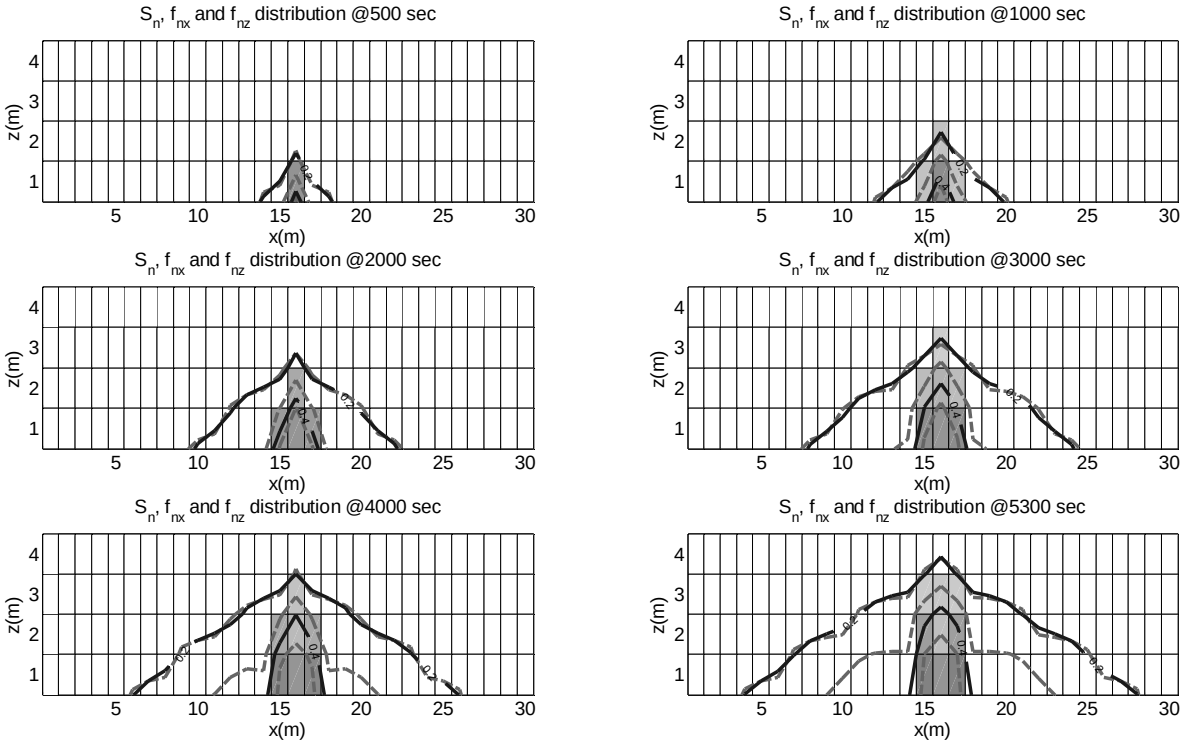

Figure 3.6 The distribution of CO_2 saturation, f_{nx} and f_{nz} over time for Darcy-Forchheimer flow (in all the graphs, solid lines are the contour line for CO_2 saturation with the values on the lines; grey and while rectangles represent Forchheimer and Darcy flow in the x dirction, respectively; the dash contour line is for f_{nz} where the most farther contour line from the injection node can be seen as the boundary between Forchhiemer and Darcy regimes in the z direction)

As is pointed out by Wu (2001) and Ahmadi et al. (2010), the displacement of the water by CO_2 is inhibited by inertial effects in Forchheimer flow. Therefore, it is clear that CO_2 spreading vertically is inhibited by the higher resistance, leading to CO_2 spreading in favor of the x direction (shown in Figure 3.6), and that the region where there is high CO_2 saturation matches the region for Forchheimer flow. As for the water phase, all the nodes' interfaces have a Forchheimer number less than the critical Forchheimer number (with all f_w set to be zero to account for the Darcian flow), which implies that water flow in the domain is Darcian with the specified injecting rate of CO_2. This could be attributed to the fact that water's movement is intrigued by the injection of

CO_2 and the velocities of water are far less than those of CO_2 so that the Forchheimer number is smaller than the critical values.

Since the flow is symmetric in the x-direction, as is shown in Figure 3.6, it is enough to analyze the evolution of important variables for the right hand side. The evolution of S_n, P_n, f_{nx}, v_{nx}, f_{nz} and v_{nz} for the bottom row in the non-Darcian region is shown in Figure 3.7. Initially, CO_2 in all the nodes in the transport domain is in a Darcian manner with the injection of CO_2 at node (16, 1). Its east interface (16.5) waits until 102 seconds to transition to Forchheimer flow. The transition results in faster accumulation of CO_2 due to inertial effect and requires a higher pressure difference to overcome this additional friction. Similarly, the east interface for node (17, 1) realizes the transition at time 738 seconds. The transition for the upper interfaces of each node would require less time when compared with the corresponding eastern and western interfaces of the specified node due to the buoyancy effect. Also, with the transition, there is a sharper increase in CO_2 saturation and pressure, as can be seen in the upper left graph, upper right and middle left graphs in Figure 3.7. As for the interface 17.5 in the bottom row, the higher pressure difference (momentum) required by the transition is realized by not only a sharp increase in the upstream pressure (Node 17), but also a little decrease in the downstream pressure (Node 18).

An interesting point which needs to be emphasized is that CO_2 saturation for Node 18 in the bottom row at time 738 sec experiences a decrease. The reason for this is that the west interface (17.5) for Node 18 is non-Darcian while the east interface (18.5) is still Darcian, which means that there is less CO_2 flow into Node 18 due to the additional friction. Another important point is that the sharper increase in CO_2 pressure for a node (e.g., Node 17) during the transition from Darcy flow to Forchheimer flow will slightly decrease the velocity and Forchheimer number of the interface in the upstream (e.g., Interface 16.5) because the CO_2 pressure difference on which the velocity is based would decrease if one of the pressure (Node 17) increases sharply while the other pressure (Node 16) keeps the same trend. It is plausible from a first look at the v_{nx} and v_{nz} history in the middle right and lower right graphs in Figure 3.7 that the velocities are oscillating. However, a careful observation would refute the argument. The sharp decrease in the velocity history is due to the fact that the velocity is based on Darcy flow before the

transition while the velocity is based on Forchheimer flow after the transition and the difference between the two regimes is by a factor of $(1+f_{nx})$. If the velocity after the transition (e.g., 738 seconds for Interface 17.5) is depicted as Darcy flow by multiplying a factor of $(1+f_{nx})$ with the f_{nx} larger than 10, then there would not be a sharp decrease in the absolute value of velocity. As for the small oscillation near 738 seconds for Interface 18.5, the reason for the oscillation is the slight decrease of CO_2 pressure for Node 18 required by the transition of Interface 17.5. In this discussion the analysis on water phase is skipped because the change in water phase is induced by the change in CO_2 and a complete analysis on CO_2 is adequate.

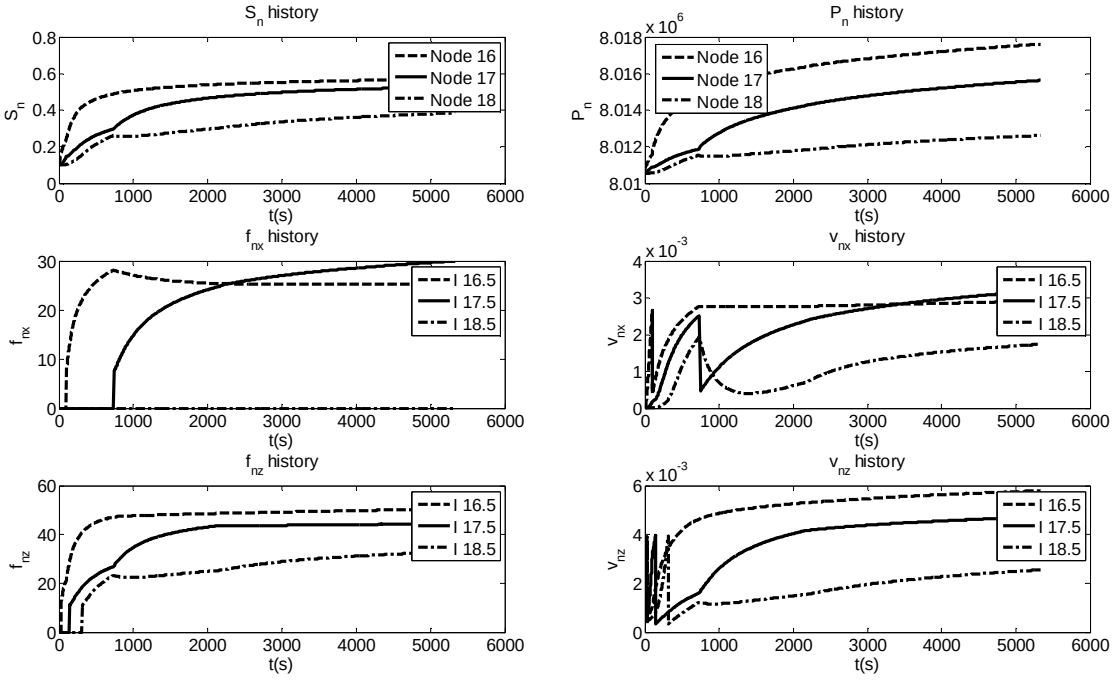

Figure 3.7 The evolution of important variables for Darcy-Forchheimer flow in the first row

3.5.2 Comparison with Darcy flow

To observe the contrast between the solutions, the application presented above is simulated again with the same parameter values except that all four Forchheimer numbers set to be zero to account for the complete Darcy flow condition in the domain. The CO_2 profiles are shown in Figure 3.8. From a comparison between Figure 3.6 and 3.8, we can conclude that CO_2 spread in a more evenly way in Darcy flow when compared to Darcy-

Forchheimer flow and a high-saturation profile in the Forchheimer region is observed and can be attributed to the additional friction caused by the inertial effect near the injecting node. It is clear that Forchheimer flow can result in higher displacement efficiency but this would require a higher injection pressure. This point can be further verified by comparing the results of Darcy flow and Darcy-Forchheimer flow. Figure 3.9 shows the comparison on the evolution of S_n, P_n, P_c and v_{nx} for Darcy flow and Darcy-Forchheimer flow. It is clear that CO_2 saturation in Forchheimer flow is much higher than that in Darcy flow. The same phenomena hold for CO_2 pressure and capillary pressure. As for the velocity, the velocity is based on Forchheimer flow after the transition for Darcy-Forchheimer flow, so its actual velocity is much larger than that of Darcy flow. To summarize, Forchheimer effect can improve displacement efficiency but at the expense of a higher injection pressure. It is important to consider the inertial effect in near-wellbore area otherwise significant errors can be introduced to the modeling.

3.5.3 Implications

The results from Darcy-Forchheimer flow and the comparison with Darcy flow have significant implications for CO_2 injection and storage in deep saline aquifers. First of all, it is important to incorporate Forchheimer effect into the numerical simulation of multiphase flow to properly characterize the additional friction caused by the high injection rate of CO_2. Neglecting the inertial effect which would require much larger injection pressure than Darcy flow does would definitely introduce considerable errors to the simulation results. If the injection operation is based on the Darcy flow assumption, then the injection pressure required in Darcy flow is not adequate to maintain the same injection rate since actually the flow is nonlinear and requires higher injection pressure, which indicates that the site selected could have stored more CO_2 if the Forchheimer effect is fully incorporated and the pressure built-up does not exceed the fracturing pressure of the porous media.

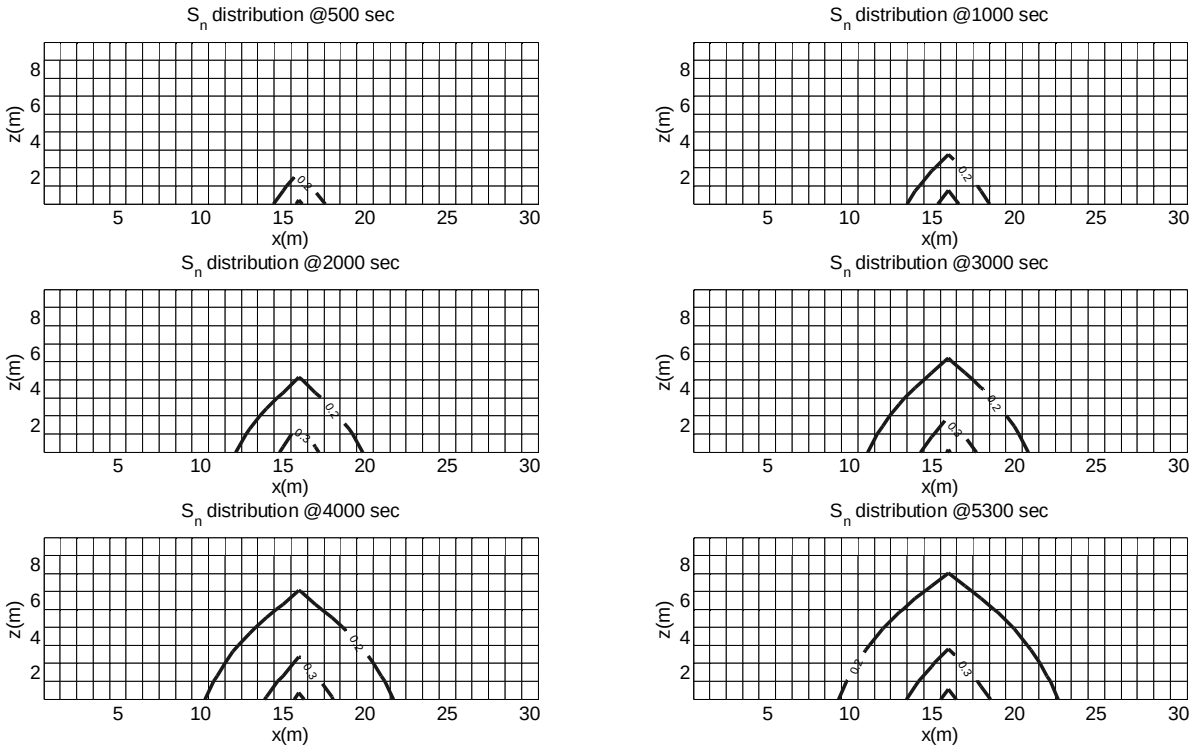

Figure 3.8 The contour lines of CO_2 saturation over time for Darcy flow with values shown on lines

Secondly, the proper way to determine the critical Forchheimer number for the transition between Darcy flow and Forchheimer flow can crucially affect the extent to which Forchheimer effect can influence the transport of CO_2 in deep saline aquifers. It is for sure that Forchheimer effect can never impact the complete domain in a large CO_2 injection field (e.g., kilometers in width and length), but it is essential to find out the region for Forchheimer flow near the injection point by applying the critical values for the transition since unacceptable errors would be induced if we neglect the nonlinear terms near the injection region. Since more severe pressure build-up would occur in the Forchheimer region, it is pivotal to monitor this pressure increase and the associated porosity and permeability change in the Forchheimer region while continuing the injection of CO_2. The location and profile of the Forchheimer zone can help decide the location and numbers of monitoring wells which can ensure the long-term safe injection and storage of CO_2 in the subsurface.

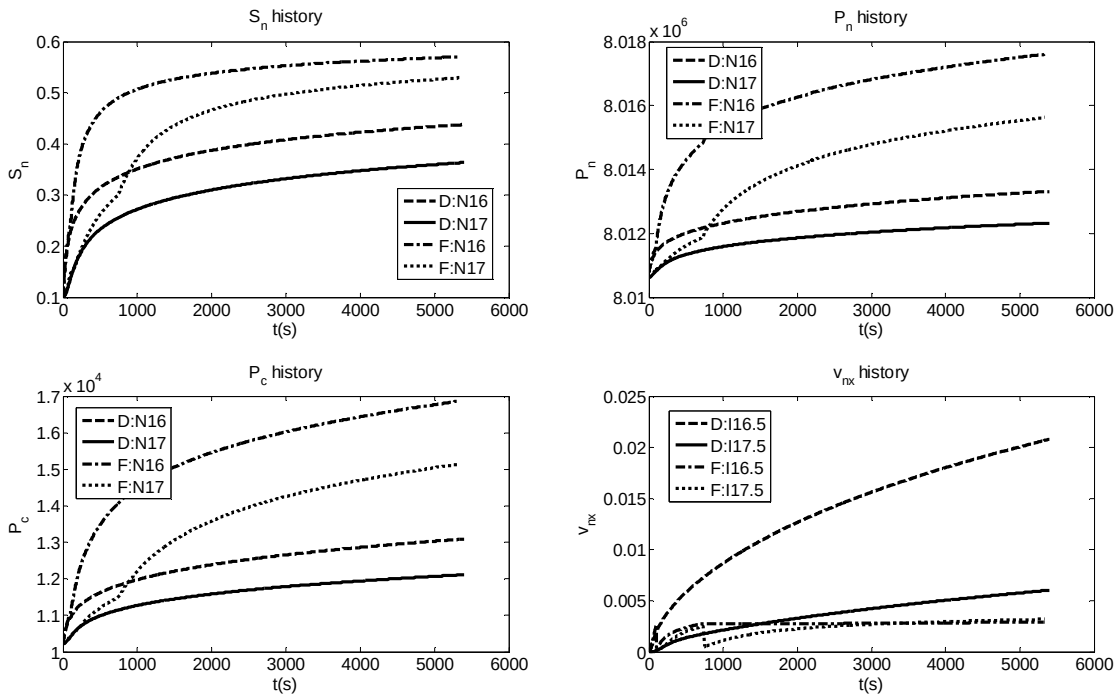

Figure 3.9 Comparison of the evolution of important variables for Darcy and Darcy-Forchheimer flows in the first row (in the graphs, D stands for Darcy flow while F is for Darcy-Forchheimer flow; N is for node and I is for interface)

Finally, the higher displacement efficiency by CO_2 is good news for CO_2 sequestration into deep saline aquifers. This means that for the same volume of porous media, more pore space can be occupied by CO_2 in Forchheimer flow than Darcy flow for the same injection rate and time. A comparison between Figure 3.6 and 3.8 would indicate that more CO_2 can be stored in Forchheimer regime than Darcy regime. When compared with Figure 3.8 where the saturation contour lines expand smoothly with time for Darcian flow, Figure 3.6 shows that higher CO_2 saturation would accumulate inside the Forchheimer regime, as we can see from Figure 3.6 that the region with high saturation matches well with the Forchheimer zone. A careful comparison of Figure 3.6 and 3.8 can show that the 0.4 saturation contour lines for Darcy flow lie inside the 0.4 saturation contour lines for Forchheimer flow at the same time. This means that more CO_2 can be stored in Forchheimer regime. In addition, if we can compare Figure 3.6 over 3.8, we can find that the low saturation contour lines (e.g., 0.2) for Darcy flow mostly lie outside of those for Darcy-Forchheimer flow for the same time. This can be explained by

the observation that Forchheimer flow accumulates more CO_2 in the Forchheimer regime due to the inertial effects but spreads out less CO_2 to the Darcy regime while Darcy flow has a more uniformly distribution of CO_2 all over the domain. This more thorough displacement of water by CO_2 in Forchheimer flow should be a significant merit if the cost associated with the screening and selection, injection well design and construction, and injection operation of a CO_2 sequestration site is considered.

We should also recognize that the higher injection pressure required in Forchheimer flow is problematic for CO_2 injection applications. Everything comes with a price. The price for higher displacement efficiency is a higher injection pressure. As is shown in Figure 3.10, even in a very short time span (hours), the pressure required by Forchheimer flow in the injecting node is more than 0.05% higher (more than 4000 Pa) than that for Darcy flow. If we double the simulation time, the pressure difference for the injecting node would increase to more than 0.06%, as can be seen in Figure 3.10. The higher pressure requirement would be more significant if one considers that the injection period would in general be more than 20 years. Higher pressure requirement would first entail more energy cost. What is more troublesome is that the pressure will continue to increase and might even exceed the litho-static stress, then there is an increasing risk for triggering fracturing or shear-slip at or near the injection point. Therefore, it is vital to monitor the hydro-mechanical behavior in the near-wellbore area while continuing the injection of CO_2. Furthermore, the tradeoff between the improved displacement efficiency and the increasing injection pressure should be well balanced in order to store as much CO_2 as possible while keeping the storage zone secure and safe. This point needs to be carefully analyzed for site specific cases especially for a more realistic injection domain and a larger time scales of injection period.

3.6 Summary

In this chapter the Forchheimer flow behavior using the Forchheimer equation is developed where a convenient definition of the Forchheimer number for multiphase flows is proposed to derive a generalized Darcy-Forchheimer model. The generalized mathematical model was then discretized into a numerical model and a numerical tool using control volume finite difference method was developed to simulate two-phase

inertial immiscible and incompressible flow in two-dimensional non-deformable homogeneous porous media. The strong nonlinearity induced by the Forchheimer number, the relative permeabilities and the derivative of capillary pressure over saturation was solved using a fixed point iteration method. The numerical tool was validated by comparing the results to those obtained using a semi-analytical solution to the Buckley-Leverett problem with inertial effects and the results show good agreement with the analytical solution.

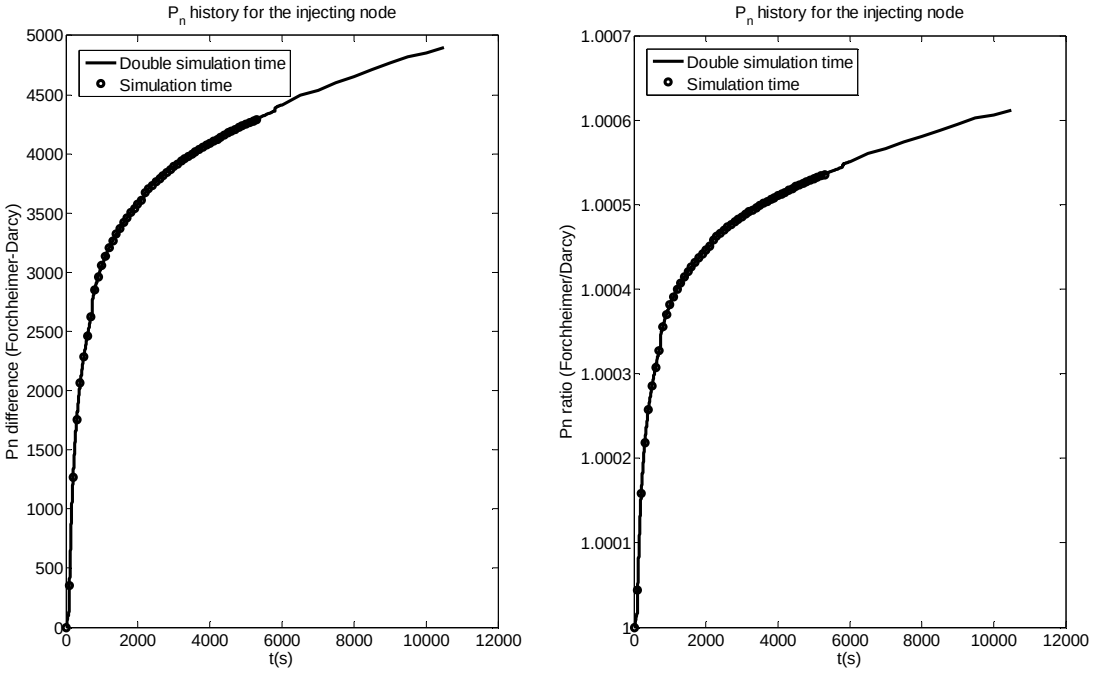

Figure 3.10 Comparison of CO_2 pressure between Forchheimer-Darcy and Darcy flow

In this study we also propose a new method to determine the critical Forchheimer number for the transition between Darcy flow and Forchheimer flow for both single phase and multiple phases and obtains the critical values for both water and CO_2 by using the new method and experimental data in the literature. The critical Forchheimer numbers were then used to analyze the application problem involving the injection of CO_2 into a deep saline aquifer. The main conclusions of this study are as follows:

i. Darcy flow is a special case of a generalized Darcy-Forchheimer flow Equation when the Forchheimer number f_α is equal to zero;

ii. Since both β_α and f_α are functions of saturation of α phase, there is a critical Forchheimer number for transition for a specific saturation for each phase in multiphase flow system;

iii. The good agreement between the numerical solution and the semi-analytical solution validates the numerical tool developed in this study;

iv. The Forchheimer flow indicates that the displacement efficiency is improved and this increases the storage capacity for the same injection rate and volume of a site;

v. The higher injection pressure required in Forchheimer flow is problematic for CO_2 injection applications because the pressure will continue to increase and might even exceed the litho-static stress and the risk for fracturing the porous media near the injection well would increase.

vi. The high vertical velocity resulting from the buoyancy effects would lead to higher Forchheimer number and thus inhibit CO_2 from spreading vertically due to the stronger resistance in the vertical direction.

These conclusions are only quantitatively dependent upon the choice of the capillary pressure curves and the Forchheimer coefficients that were determined here from experimental data provided in the literature. This study provides a useful tool for future analysis and comprehension of multiphase Darcy-Forchheimer flow and Forchheimer effects of CO_2 injection into deep saline aquifers. However, the conclusions for the application problem are preliminary because the study focuses on the applicability of the methods proposed in this study and the Forchheimer effects in the near-wellbore region and therefore the simulation time is only in terms of hours, instead of years. In order to obtain more realistic recommendations on the field operation of CO_2 sequestration site, it is necessary to conduct a thorough investigation which incorporates the transition between Darcy and Forchheimer flows on a larger domain (length scale: kilometers) for a longer time (time scale: tens of years) with higher injection rates, For such applications, although the time required for the computation would increase exponentially with the increase of domain size and time since the solution of a strong nonlinear problem is involved, these analysis should be performed prior to the injection and monitoring design at a specific site. For this analysis the procedure developed in this study can be employed.

Chapter 4 Modeling of the kinetic dissolution of SO_2 and the induced porosity and permeability changes due to SO_2 co-injection

In this chapter, we develop a multiphase flow and contaminant transport model which incorporates the kinetic mass transfer of sulfur dioxide (SO_2) and carbon dioxide (CO_2) into deep saline aquifers and the coupling between the fluid flow and the induced porosity and permeability changes caused by the brine acidification. Then the model is used to analyze the brine acidification and the resultant mineral dissolution and precipitation which would further cause the changes in porosity and permeability for a one-dimensional domain with SO_2 co-injection with CO_2 into deep saline aquifers under four model scenarios: two of them describing CO_2 and SO_2 mass transfer limitation from supercritical CO_2 ($scCO_2$)to the brine (with or without the coupling between the change in porosity and permeability and the fluid flow model) while the other two dealing with the case of SO_2 phase equilibrium between the entire volumes of $scCO_2$ and brine (with or without the coupling). To predict brine pH, we develop a geochemical model that simulates aqueous speciation and thermodynamic phase equilibrium of injected CO_2 and SO_2 with a typical saline aquifer. In addition, the sensitivity analysis of selected important kinetic parameters on the outcomes of the simulations is also conducted and covered.

4.1 Fluid flow and contaminant transport models

The flow and transport model developed is based on space discretization by means of control volume finite difference method. An implicit scheme is used for the individual components of the model, consisting of flow and transport. As for the multiphase flow applications, the readers may refer to Zhang and Aral (submitted) for more details. As for the contaminant transport model, in general, the governing equations for SO_2 transport in the water and $scCO_2$ phase and for CO_2 transport in the water phase can be expressed as

$$\frac{\partial(\theta S_w C_w)}{\partial t} = \nabla\bullet(\theta S_w D_w(\nabla C_w)) - \nabla(v_w C_w) + \theta S_w \chi(C_w^e - C_w) + q_w C_w^*$$
$$\frac{\partial(\theta S_n C_n)}{\partial t} = \nabla\bullet(\theta S_n D_n(\nabla C_n)) - \nabla(v_n C_n) - \theta S_w \chi(C_w^e - C_w) + q_n C_n^* \quad (4.1)$$
$$\frac{\partial(\theta S_w C_w^{CO_2})}{\partial t} = \nabla\bullet(\theta S_w D_w^{CO_2}(\nabla C_w^{CO_2})) - \nabla(v_w C_w^{CO_2}) + \theta S_w \chi^{CO_2}(C_w^{eCO_2} - C_w^{CO_2}) + q_w C_w^{*CO_2}$$

where C_w and C_n (M/L^3) are SO_2 concentrations in the water and $scCO_2$ phase, respectively, χ is the lumped mass transfer rate (T^{-1}) for SO_2, D_w and D_n (L^2/T) are SO_2 diffusion coefficient in the water and $scCO_2$ phase, respectively, θ is the porosity, S_w and S_n are saturations for water and CO_2, separately, v_w and v_n (L/T) are velocities for water and CO_2, separately, C_w^e (M/L^3) is the equilibrium concentration of SO_2 in saline phase corresponding to the concentration in the $scCO_2$, C_w^* and C_n^* (M/L^3) are specified concentrations at a source/sink in wetting and non-wetting phase with a flow rate q_w and q_n (/T), respectively.

Using control volume finite difference method, for 1D case, Equation (4.1) can be discretized as

$$\begin{aligned}
&\theta S_{wi}^{t+1} C_{wi}^{t+1} - \left(a(C_{wi+1}^{t+1} - C_{wi}^{t+1}) - b(C_{wi}^{t+1} - C_{wi-1}^{t+1})\right) + \frac{\Delta t}{\Delta x} v_{w_i}^{t+1}(C_{wi+1}^{t+1} - C_{wi}^{t+1}) \\
&\quad + \Delta t\theta S_w^{t+1}\chi C_{wi}^{t+1} = \Delta t\theta S_{wi}^{t+1}\chi C_{wi}^{et} + \Delta t q_w C_{wi}^{*t} \\
&\theta S_{ni}^{t+1} C_{ni}^{t+1} - \left(c(C_{ni+1}^{t+1} - C_{ni}^{t+1}) - d(C_{ni}^{t+1} - C_{ni-1}^{t+1})\right) + \frac{\Delta t}{\Delta x} v_{n_i}^{t+1}(C_{ni+1}^{t+1} - C_{ni}^{t+1}) \\
&\quad - \Delta t\theta S_w^{t+1}\chi C_{wi}^{t+1} = -\Delta t\theta S_{ni}^{t+1}\chi C_{wi}^{et} + \Delta t q_n C_{ni}^{*t} \\
&\theta S_{wi}^{t+1} C_w{}_i^{CO_2 t+1} - \left(e(C_w{}_{i+1}^{CO_2 t+1} - C_w{}_i^{CO_2 t+1}) - f(C_w{}_i^{CO_2 t+1} - C_w{}_{i-1}^{CO_2 t+1})\right) + \frac{\Delta t}{\Delta x} v_{w_i}^{t+1}(C_w{}_{i+1}^{CO_2 t+1} - C_w{}_i^{CO_2 t+1}) \\
&\quad + \Delta t\theta S_w^{t+1}\chi^{CO_2} C_w{}_i^{CO2 t+1} = \Delta t\theta S_{wi}^{t+1}\chi^{CO_2} C_w{}_i^{eCO_2 t} + \Delta t q_w C_w{}_i^{*CO_2 t}
\end{aligned} \quad (4.2)$$

where a, b, c, d, e, and f are defined as

$$a = \left[\frac{\Delta t}{(\Delta x)^2}\theta S_w D_w\right]_{i+\frac{1}{2}} \qquad b = \left[\frac{\Delta t}{(\Delta x)^2}\theta S_w D_w\right]_{i-\frac{1}{2}} \qquad c = \left[\frac{\Delta t}{(\Delta x)^2}\theta S_n D_n\right]_{i+\frac{1}{2}}$$
$$d = \left[\frac{\Delta t}{(\Delta x)^2}\theta S_n D_n\right]_{i-\frac{1}{2}} \qquad e = \left[\frac{\Delta t}{(\Delta x)^2}\theta S_w D_w^{CO_2}\right]_{i+\frac{1}{2}} \qquad f = \left[\frac{\Delta t}{(\Delta x)^2}\theta S_w D_w^{CO_2}\right]_{i-\frac{1}{2}} \quad (4.3)$$

We note that the advection terms in Equation (4.1) need to be discretized using upwind scheme based on the flow direction.

The equilibrium concentration of SO_2 in saline phase corresponding to the concentration in the $scCO_2$ phase C_w^e can be defined as

$$C_w^e = \phi_{SO_2} P_{SO_2} K_H \tag{4.4}$$

where ϕ_{SO_2} is the fugacity coefficient of SO_2 in the $scCO_2$ phase and K_H is the Henry's Law constant. Both the fugacity coefficient and Henry's Law constant need to be adjusted according to the temperature and pressure in the simulated domain. The SO_2 fugacity coefficient in the $scCO_2$ is determined from the reduced-virial-coefficient method in Tarakad and Danner (1977). The adjustment of the Henry's Law constant for high pressures was done by suing the Krichevsky-Ilinskaya equation (Prausnitz et al., 1986).

As to the equilibrium concentration of CO_2 in saline phase corresponding to the concentration in the $scCO_2$ phase, we adopt a correlation developed by Spycher and Reed (1988) to adjust the fugacity coefficient. The Henry's Law constant is corrected by using the equations developed by Battistelli et al. (1997).

The lumped mass transfer rate χ can be expressed as

$$\chi = k_d a_{wn} \tag{4.5}$$

where a_{wn} (L^2/L^3) is the area of wn-interface per unit volume of the porous medium and k_d (M/T) is the mass transfer rate coefficient. For CO_2, a_{wn} can be estimated by using the empirical correction proposed by Joekar-Niasar et al. (2008) with the equation as

$$a_{wn} = 849 + 3858S_w - 0.224P_c - 3992S_w^2 + 0.006S_w P_c + (1.283E-5)P_c^2 \tag{4.6}$$

where S_w and P_c are the saturation for water and the capillary pressure. As for SO_2, since the volume (mass) ratio of SO_2 to CO_2 is assumed to be constant, e.g., C, in this study, the following equation is used to adjust the a_{wn} for SO_2

$$\frac{V_{SO_2}}{V_{CO_2}} = C \qquad \frac{A_{SO_2}}{A_{CO_2}} = C^{2/3} \qquad \frac{(a_{wn})_{SO_2}}{(a_{wn})_{CO_2}} = C^{2/3} \tag{4.7}$$

Shindo et al. (1995) studied the kinetic dissolution of CO_2 into water from the surface of CO_2 hydrate at high pressure and estimated the mass transfer rate coefficient k_d for CO_2 to be $1.25e^{-6}$ m/s. This study used their experimental results to simulate the kinetic dissolution of CO_2 into water. As for SO_2, no applicable kinetic data can be found in the

literature. We adopt the definition for Sherwood number, Sh, for the mass transfer through the film around a spherical particle in a fluid, expressed as (Smith, 1970)

$$k_d = Sh\frac{D_m}{d} \tag{4.8}$$

where D_m and d are the diffusion coefficient in the film and droplet diameter. While Sh is correlated by Reynolds number, Re, and Schmidt number, Sc, by Ranz et al. (1952)

$$Sh = 2.0 + 0.6\,\mathrm{Re}^{0.5}\,Sc^{1/3} = 2.0 + 0.6(\frac{d\rho v}{\mu})^{0.5}(\frac{\mu}{\rho D_m})^{1/3} \tag{4.9}$$

where ρ, v and μ are the fluid density, the velocity of the surrounding stream and the viscosity of the fluid, respectively.

4.2 Geochemical models

In the geochemical model, an iterative process was used to compute aqueous speciation of carbonates, sulfates, and hydrogen sulfide grid by grid. All aqueous speciation reactions are assumed to be instantaneous and with equilibrium and are shown with their equilibrium constants in Table 4.1.

As for the water-rock reactions, this study simulates an infinitely well-stirred batch reactor, and thus reaction kinetics is strictly surface controlled. In this study, a general form of rate expression is used, which is based on transition state theory (TST) (Lasaga et al., 1994; Steefel and Lasaga, 1994):

$$\frac{\Delta M}{\Delta t} = r = kA[1 - (\frac{Q}{K_{eq}})^p]^q \tag{4.10}$$

where r (M/T) is kinetic rate, k (M/ L^2/T) is the rate constant, A (L^2) is the specific reactive surface area per kg water, Q is the reaction quotient and K_{eq} is the equilibrium constant. The parameter p and q must be determined by experiment, but are commonly set equal to unity when data are unavailable. For many minerals, the rate constant k can be summed from three mechanisms (Lasaga et al., 1994; Palandri and Kharaka, 2004):

$$k = k_n^{25}\exp\left[\frac{-E_n}{R}(\frac{1}{T} - \frac{1}{298.15})\right] + k_H^{25}\exp\left[\frac{-E_H}{R}(\frac{1}{T} - \frac{1}{298.15})\right]a_H^{n_H} + k_{OH}^{25}\exp\left[\frac{-E_{OH}}{R}(\frac{1}{T} - \frac{1}{298.15})\right]a_{OH}^{n_{OH}} \tag{4.11}$$

where subscripts n, H and OH represent neutral, acid and base mechanisms, respectively, E is the activation energy, k^{25} is the rate constant at 25 °C, R is gas constant, T is absolute temperature, a is the activity of the species, and n is power term (constant).

After the water-rock reactions at each time step, the induced changes in porosity are adjusted by the following equation for the change of minerals volume in each cell:

$$\frac{\Delta V}{V} = \frac{\sum_p n_p v_p^0 - \sum_R n_R v_R^0}{\sum_R n_R v_R^0} \tag{4.12}$$

where n_p and v_p^0 represent the moles and the molar volume of the product solid phase, n_R and v_R^0 represent the moles and the molar volume of the reactant solid phase. The changes of permeability caused by the porosity change can be described by the equation proposed by Xu et al. (2003)

$$\frac{k_n}{k_o} = \left(\frac{\theta_n}{\theta_o}\right)^3 \left(\frac{1-\theta_o}{1-\theta_n}\right)^2 \tag{4.13}$$

where subscripts o, and n represent the last and current time step, respectively, θ and k are the porosity and permeability, respectively.

Table 4.1 Aqueous reactions considered in this study

Reaction	$\log(K_{eq})$
$H_2CO_3 \Leftrightarrow HCO_3^- + H^+$	-6.27
$HCO_3^- \Leftrightarrow CO_3^{2-} + H^+$	-10.16
$H_2O \Leftrightarrow OH^- + H^+$	-13.49
$SO_{2(aq)} + H_2O \Leftrightarrow \frac{3}{4}HSO_4^- + \frac{3}{4}H^+ + \frac{1}{4}H_2S_{(aq)}$	5.68
$HSO_4^- \Leftrightarrow SO_4^{2-} + H^+$	-2.12
$H_2S_{(aq)} \Leftrightarrow HS_{(aq)}^- + H^+$	-7.04

The coupling of the three components (fluid flow model, mass transport model and geochemical model) can be solved by an iterative procedure. The numerical algorithm shown in Figure 4.1 is employed to solve the problem. During the process several points need to be emphasized:

i. For each time step, the velocities and saturations in the fluid flow model are used for contaminant transport model; the concentrations for SO_2 and CO_2 in the

transport model are used for geochemical model; and the changes in the mineral are used to correct the porosity and permeability;

ii. Since the changes in porosity and permeability are coupled with the fluid flow model, an inner iterative loop is needed inside the time incremental loop;

iii. In the inner loop, a criterion based on the change of X is used to determine whether the coupling between the porosity and permeability change and the fluid flow is convergent or not. The choice for the variable X could be saturation, pressure, porosity or permeability. Since CO_2 pressure is more sensitive to the change of porosity and permeability, in this study, X is selected as CO_2 pressure.

iv. Inside each component, there is also an iterative loop to solve for the primary variables, e.g., S_n and P_w for fluid flow model and C_w and C_n for mass transport model. So many loops can lead to a high requirement for computation.

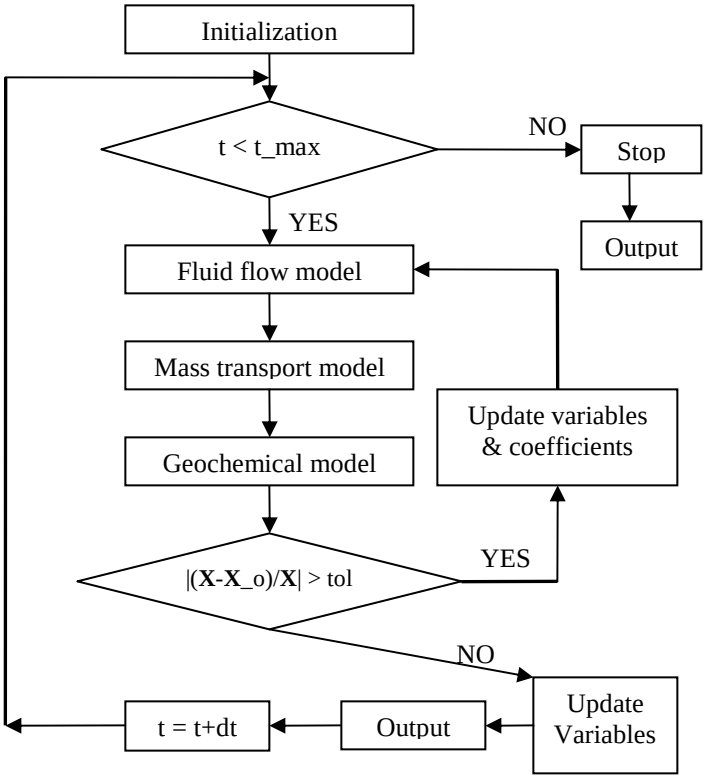

Figure 4.1 Flowchart for the numerical algorithm

4.3 Problem setup for application of kinetic dissolution of SO_2 in a 1-D domain

4.3.1 Fluid flow and contaminant transport conditions

A single-layer uniform formation with a thickness of 100 m and a depth of 800 m is considered in the present model (Figure 4.2). The formation is assumed to extend infinitely in the horizontal direction. In all scenarios, a constant flow rate of CO_2 with 1% of SO_2 in mass (10^{-6} m^3/s per square meter normal to the 1D domain) is continuously injected into the first left node. The injection rate is determined by considering that a standard size 1,000-MW coal-fired power plant produces CO_2 at a rate approximately 350 kg/s (Hitchon, 1996), equivalent to 0.73 m^3/s CO_2. The CO_2 emitted would require a field about 7300 meters in width and 100 meters in thickness. The domain and boundary conditions and parameter values used here are shown in Figure 4.2 and Table 4.2 and 4.3.

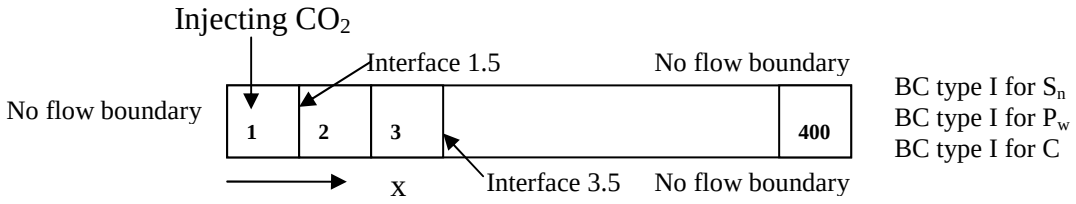

Figure 4.2 Model domain and boundary conditions (to represent a node, e.g., the injecting node (in Column 1) can be expressed as Node 1; for an interface, the east interface of the injecting node can be represented Interface 1.5 (or I 1.5))

Table 4.2 Parameters for the fluid flow and contaminant transport

Parameters for the fluid flow and contaminant transport in 1D homogeneous porous media

k	λ	S_w^r	S_n^r	Pd	ρ_w	ρ_n	μ_w	μ_n	Droplet diameter (d)
m^2	-	-	-	Pa	kg/m^3	kg/m^3	Pa s	Pa s	m
2e-13	3.86	0.35	0.05	10000	994	479	7.43e-4	3.95e-5	0.05

Depth	Aquifer temperature	Aquifer salinity	SO_2 mass ratio in scCO2 flow	Thick-ness	$D_{(CO_{2(aq)})}$	$D_{(SO_{2(scCO_2)})}$	$D_{(SO_{2(aq)})}$
m	°C	mol/L	percentage	m	m^2/s	m^2/s	m^2/s
800	60	1	1	100	2.73e-9	2.49e-8	2.31e-9

4.3.2 Geochemical conditions

As is pointed out by Palandri and Kharaka (2005), iron-bearing sediments have the merits of widespread geographic distribution, generally greater thickness, and higher porosity and permeability, compared with other sediments like plagioclase-bearing (Ca-bearing) and illitic (Mg-bearing) sediments. Furthermore, Blatt (1982) shows in his study that sediments globally have average iron contents of 4.8 and 2.4 wt% for mudrocks and sandstone, respectively. Therefore, these sediments have a significant potential to trap CO_2 and thus this study chooses the formation studied as iron-bearing sediment.

Table 4.3 Boundary and initial conditions and simulation parameters

Properties	***Values***	**Comment**	
Boundary conditions			
Water pressure at x=0 m	No flow boundary	Left boundary	
Water pressure at x=1600 m	P_w = 8 M Pa, BC Type I	Right boundary	
CO_2 saturation at x=0 m	No flow boundary	Left boundary	
CO_2 saturation at x=1600 m	S_n = 0.15, BC Type I	Right boundary	
SO_2/CO_2 concentration at x=0 m	No flow boundary	Left boundary	
SO_2/CO_2 concentration at x=1600 m	C = 0, BC Type I	Right boundary	
CO_2 injecting rate @ node 1	$1*10^{-6}$ m^3/s	Per square meter normal to the 1D domain	
Initial conditions			
CO_2 saturation	S_n = 0.15		
Water pressure	P_w = 8 M Pa		
SO_2/CO_2 concentration	0		
Space discretization		**Time discretization**	
Domain size, Length	L=1600 m	Simulation time	1 year
Space step size	dx =4 m	Time step size	dt=500 s

Since the multiphase flow and contaminant transport model proposed in this study involves solving two linear systems in two iterative processes (plus the iterative process for the coupling between fluid flow and porosity changes), which are computation-demanding, we simplify the geochemical model by assuming that the initial mineral composition of the formation is 100 wt% of hematite (Fe_2O_3) with a density of 5280 kg/m^3. This simplification can help to estimate the maximal possible impacts the kinetic mass transfer of SO_2 and CO_2 could have on the porosity and permeability changes.

Where sediments contain ferric iron, it must be first reduced before precipitation as iron sulfide. The reduction of ferric iron by sulfide can be realized by the following two reactions:

$$4Fe_2O_{3(s)} + HS^-_{(aq)} + 15H^+ \Leftrightarrow 8Fe^{2+} + SO_4^{2-} + 8H_2O \quad (4.14a)$$

$$8Fe^{3+} + HS^-_{(aq)} + 4H_2O \Leftrightarrow 8Fe^{2+} + SO_4^{2-} + 9H^+ \quad (4.14b)$$

In this study, we consider only hematite (Fe_2O_3), rather than Fe^{3+}, because the primary source of ferric iron is contained in minerals. After the reduction of ferric iron to ferrous iron, ferrous iron can react with sulfide by the following two reactions:

$$4Fe^{2+} + SO_4^{2-} + 7HS^-_{(aq)} + H^+ \Leftrightarrow 4FeS_{2(s)}(pyrite) + 4H_2O \quad (4.15a)$$

$$Fe^{2+} + HS^- = FeS(amorphous) + H^+ \quad (4.15b)$$

It needs to be noted that amorphous FeS is less stable and would be replaced by FeS_2 (with a density of 4800 kg/m^3) if additional sulfide is available after all iron precipitates in FeS, which is valid in this study. Therefore, we only consider Equation (15a) in this study. After the formation of pyrite, it might begin to dissolve into the water phase, but the dissolution of pyrite needs the presence of Fe^{3+}, as is shown in Table 4.4. Furthermore, there would be few, if not no, Fe^{3+} in the water phase in this study. Therefore, the dissolution of pyrite is negligible compared with the precipitation of pyrite.

Since the simulations considered herein are restricted to moderately to extremely acidic conditions, only the acid-catalyzed mechanism has a significant effect upon reaction rates, and the other two mechanisms are negligible in comparison and therefore are ignored herein. The mineral dissolution rate parameters are summarized in Table 4.4. Mineral precipitation rates were computed by dividing the dissolution rate by the equilibrium constant, based on the principle of microscopic reversibility (Lasaga, 1998).

Table 4.4 Rate equation parameters

Mineral	A (cm^2/g)	Rate constant (Log mol/m^2 s)	Activation energy (kJ/mol)	Reaction order w.r.t activity of H+	Reaction order w.r.t given species
Hematite	12.9	-9.39	66.2	1	0
Pyrite	12.9	-7.52	56.9	-0.5	0.5,Fe^{3+}

4.4 Results and discussion

Four model scenarios are analyzed in this study, with two of them describing CO_2 and SO_2 mass transfer limitation from $scCO_2$ to the brine (with or without the coupling between the change in porosity and permeability and the fluid flow model) while the

other two dealing with the case of SO_2 phase equilibrium between the entire volumes of $scCO_2$ and brine (with or without the coupling). To simplify the notation, 'Ki-cou' and 'Ki-non' denote the cases for the kinetic mass transfer of CO_2 and SO_2 with and without the coupling, separately; 'Equi-cou' and 'Equi-non' stand for the cases for equilibrium dissolution of CO_2 and SO_2 with and without the coupling, respectively. This simplified notation will be used throughout the paper.

In this section, the results for the base case with kinetic mass transfer and the coupling will be presented and discussed first. Then a comparison among the four cases will be conducted. In addition, parameter sensitivity analysis will also be covered after that.

4.4.1 Base case (Ki-cou)

The output for the simulations in this study is quite extensive, essentially consisting of three parts of information: (1) the multiphase flow pattern, (2) the aqueous phase composition, (3) the mineral distribution and the induced changes in the porosity and permeability. For convenience, we only present selected information closely related to the objectives of this study in graphical form as a function of the distance from the injecting well (Node 1), at several times as 2.5e6 seconds (4 weeks), 1.25e7 seconds (20 weeks), 2.25e6 seconds (37 weeks), and 3.15e7 seconds (52 weeks). Since this study is to investigate the effects that the kinetic mass transfer of CO_2 and SO_2 and the coupling between porosity change and fluid flow would have on the near well-bore area during the injection period, the evolution history of selected important information near the injecting node will be also presented. During the presentation, of the whole domain, only the part having distinguishable difference in the selected variables will be presented. For example, for CO_2 saturation, there is no major change for the right half domain (800-1600 meters), so only the left half domain is shown in the top left (TL) graph in Figure 4.3.

As we can see from the TL graph in Figure 4.3, CO_2 spread to the right continuously with time and the saturation in the injecting well also increases with time, as is expected. However, for CO_2 pressure shown in the TR graph, it seems that CO_2 pressure experiences a massive increase from the initial pressure 8 MPa to around 15 MPa. This can be attributed to the fact that the fluids can only move to the right hand side since all the other directions have no flow boundary and that the absolute permeability

($2x10^{-13}$ m^2) is small enough to intrigue a huge pressure increase. In addition, CO_2 pressure in the injecting well decreases by a smaller magnitude with time, which can be again verified in the TR graph in Figure 4.5. This can be explained by the fact that water pressure before the saturation front (e.g., the region for $x < 80$ meters at time 2500000 secs in the TL graph in Figure 4.3) will eventually undergo a decrease with time since less and less water is left to be replaced by CO_2, which will require a smaller and smaller water pressure to push the water to the right hand side. Furthermore, the decrease in the water pressure will be the dominant factor in the evolution of CO_2 pressure since the change of capillary pressure is in an order of 1000 Pa (shown in the LL graph in Figure 4.5) and the magnitude of water pressure is in an order of 10 MPa with the change of water pressure in an order much larger than that of capillary pressure. Therefore CO_2 pressure experiences a decrease with the decrease of water pressure, although the increase of capillary pressure with the increase of CO_2 saturation with time tries to increase the CO_2 pressure but fails due to the much smaller magnitude. When it comes to SO_2 concentration in the $scCO_2$, a constant mass ratio (a percent of SO_2 in the $scCO_2$) is assumed in the injecting well since SO_2 together with $scCO_2$ is continuously injected into the first node and the mass transfer for SO_2 from the $scCO_2$ to the water phase has proven not to be fast enough to deplete the SO_2 in the $scCO_2$ in the injecting node. As is shown in the ML graph in Figure 4.3, SO_2 in the $scCO_2$ moves to the right hand side with time, but in a pace much slower than the movement of CO_2 if a comparison between the TL and ML graphs. For example, for x=200 meters at 12500000 sec, CO_2 saturation is close to 0.25 but SO_2 concentration in the $scCO_2$ is zero, due to the mass transfer to the water phase and mass diffusion to its neighboring nodes. The SO_2 solubility in the water (MR graph in Figure 4.3) has a direct relationship with SO_2 concentration in the $scCO_2$, as is ruled by Henry's Law, so the profiles of SO_2 solubility in the water are similar to those for SO_2 concentration in the $scCO_2$. SO_2 concentration in the water (LL graph in Figure 4.3) has a time lag compared with the profiles of SO_2 solubility because of the mass transfer limitations, but has similar profiles with those for H^+ (LR graph in Figure 4.3) since the concentration of H^+ is highly dependent of SO_2 concentration in the water.

The dissolution of Hematite continues with time, as is shown in the TL graph in Figure 4.4, with a maximal decrease percentage of 0.24 in the first node at 3.15e7 sec.

With the dissolution of hematite and SO_2 into the water phase, pyrite will begin to precipitate over time (TR graph in Figure 4.4). The change of the composition of the mineral will have a volume change which can be described by Equation (4.12). The induced changes in the porosity and permeability by the mineral dissolution and precipitation are shown in the LL and LR graphs in Figure 4.4. The porosity experiences a maximal decrease percentage of 0.25 while the maximal decrease percentage for the permeability is 1.05 in the first node at 3.15e7 sec. This magnitude of change in the porosity and permeability could have significant impacts on the fluid flow, especially on the pressure since pressure is more sensitive to porosity and permeability. A detail comparison between the cases with and without the coupling of porosity and permeability change with fluid flow will be covered later in Section 4.4.2.

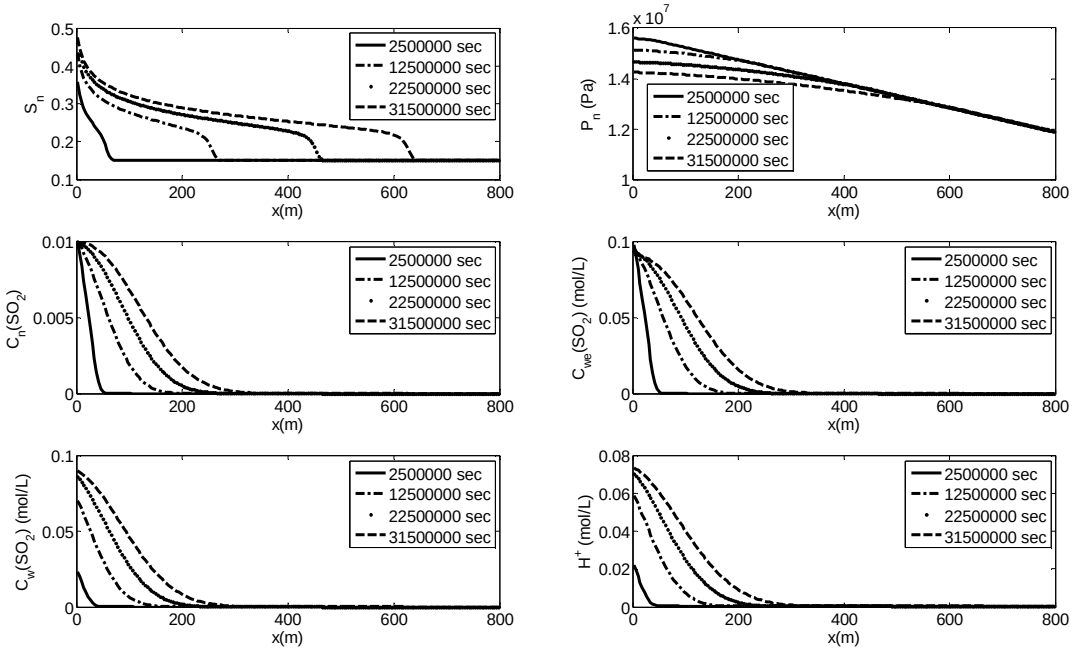

Figure 4.3 Distribution of selected variables at different times (the top left (TL), top right (TR), middle left (ML), middle right (MR), lower left (LL) and lower right (LR) graphs are for CO_2 saturation, CO_2 pressure, SO_2 concentration in the $scCO_2$, SO_2 solubility in the water, SO_2 concentration in the water, and H^+ concentration, respectively)

From the analysis above, we can see that the region near the injecting node is where most changes in the saturation, pressure, porosity and many other variables are expected.

Therefore, the evolution history of selected important information for the first three nodes (interfaces) will be presented next.

CO_2 saturation in the first node increases to a value larger than 0.3 in a very short time span due to the continuous injection of CO_2 in the first node, as is shown in the TL graph in Figure 4.5. As for the CO_2 pressure in the TR graph, the pressures for all the three nodes increase to a massively high pressure and undergo a smaller decrease over time due to the decrease in water pressure in a much larger magnitude than that for the increase in capillary pressure. The capillary pressures (LL graph) share a similar profile with that for CO_2 saturation because of its high dependence on the CO_2 saturation. When it comes to CO_2 flow velocity (LR graph), it goes through a short period of rapid increase before stabilizing with time.

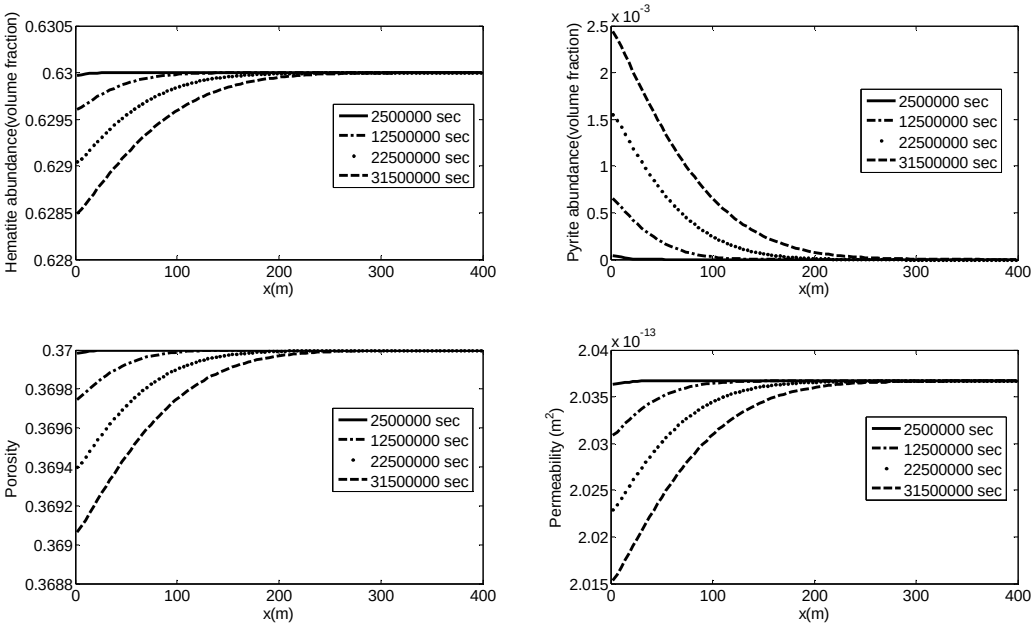

Figure 4.4 Distribution of selected variables at different times (TL, TR, LL and LR graphs are for Hematite and Pyrite abundance in each node, porosity and permeability, respectively)

It is more obvious to observe (in the TL and TR graphs in Figure 4.6) the time lag between SO_2 concentration in the water and SO_2 solubility in the water due to the mass transfer limitations from the $scCO_2$ to the water phase. As is expected, SO_2 concentration in the $scCO_2$ and SO_2 solubility in the water share almost the same profiles in the TR and

LL graphs because of Henry's Law. As for CO_2 concentration in the water in the LR graph, the time for CO_2 concentration in the first three nodes to hit its solubility limit is short. Actually, if we compare the TL graph in Figure 4.5 to the LR graph in Figure 4.6, we can find that CO_2 concentration in each of the three nodes reach its solubility limit almost at the same time when CO_2 saturation front is in the same node. It suggests that the role for the mass transfer limitations is insignificant if a simulation time larger than 1e7 seconds is considered. Therefore, it is not necessary to include the kinetic dissolution of CO_2 from the $scCO_2$ to the water phase into the simulation models unless the simulation time is very short (in terms of days or less).

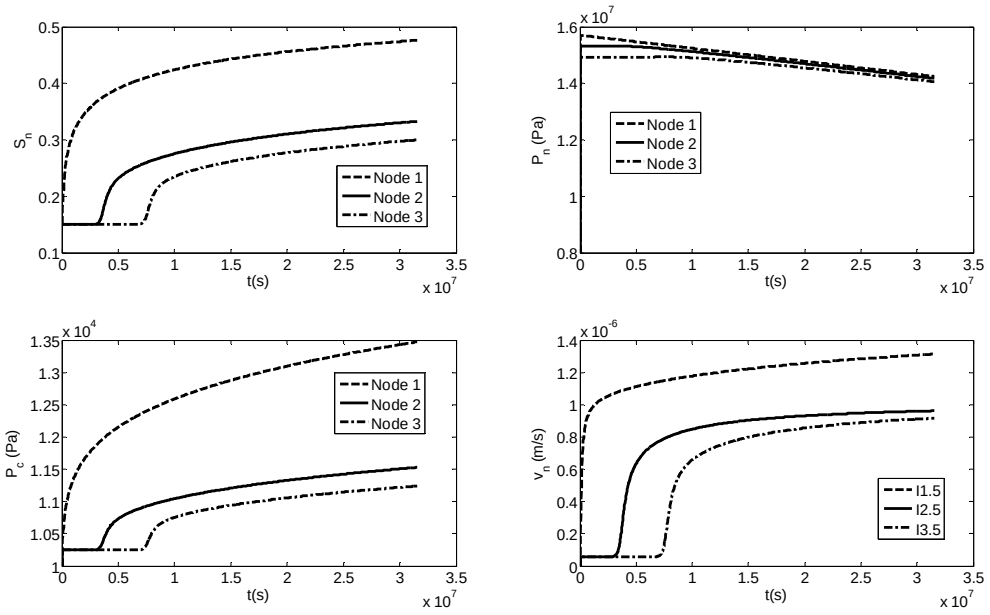

Figure 4.5 Evolution of selected variables for different nodes/interfaces (LL and LR graphs are for capillary pressure, CO_2 flow velocity for the first three nodes' east interfaces, respectively)

As for the evolution for H^+ concentration in the TL graph in Figure 4.7, a similar profile can be found for SO_2 concentration in the water phase in the TL graph in Figure 4.6 because the concentration of H^+ is highly dependent of SO_2 concentration in the water, although CO_2 in the water has a larger concentration and can also release H^+ to the water (but with a much lower ability since carbonic acid is a weak acid while sulfuric acid (a product of the reaction of SO_2 with H_2O) is a strong acid). At the end of one year, the porosity experiences a decrease percentage of 0.25, 0.09, and 0.02 for Node 1, 2, and 3,

respectively, as is shown in The TR graph in Figure 4.7. This magnitude in the changes of porosity would have corresponding decrease percentage for the permeability (LL graph in Figure 4.7) of 1.05, 0.38, and 0.08 for Node 1, 2, and 3, separately. The magnitude of the change for the second and third nodes might not be as significant as someone might expect, but the changes are for a simulation time of one year only. The changes would be much more significant if an injection period of more than 30 years is considered. In addition, the combination of these minor changes in the porosity and permeability, together with the changes in the first node, would have a collective impact that might be much more important than expected and therefore needs further investigations, especially on the water and CO_2 pressure because the pressures are very sensitive to the change of porosity and permeability and these pressures are very important operating parameters during CO_2 injection and storage.

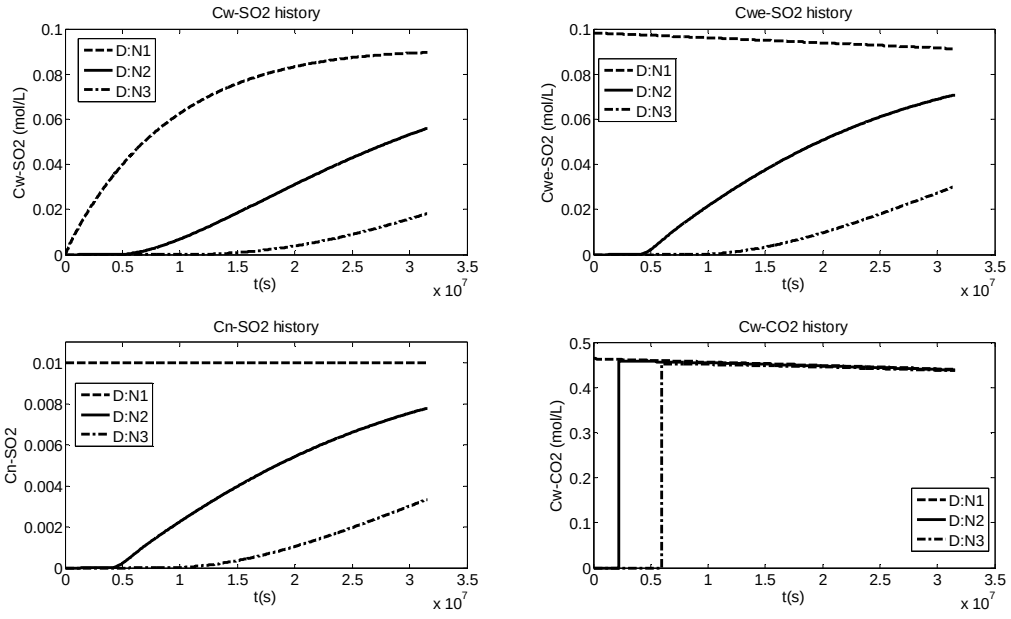

Figure 4.6 Evolution of selected variables for different nodes (LR graph is CO_2 concentration in the water phase)

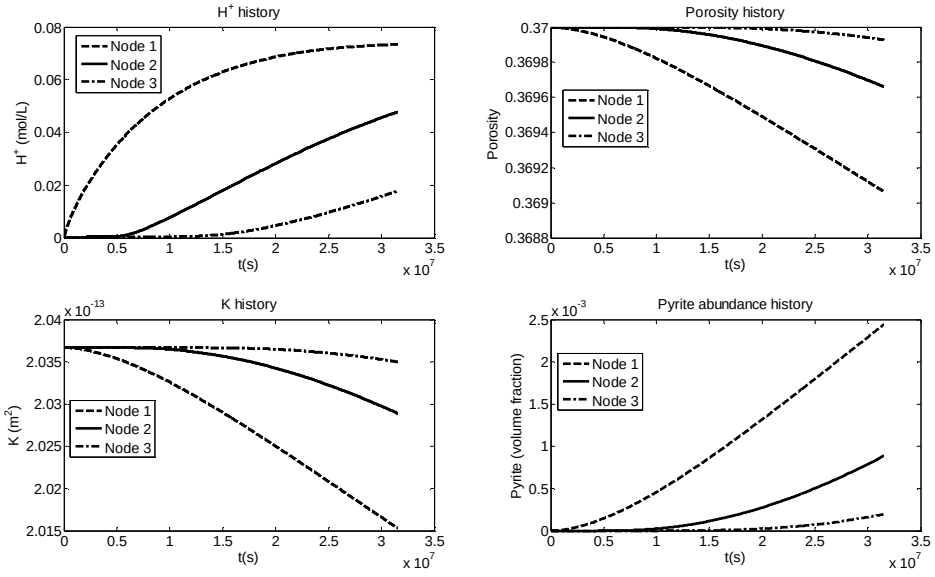

Figure 4.7 Evolution of selected variables for different nodes

4.4.2 Model comparison

From the top left graph in Figure 4.8, we can see that CO_2 saturation at 3.15e7 sec for all the scenarios is almost the same expect for some difference near the saturation front which can be easily observed in the low left graph in Figure 4.8. Since there is no impact of the changes in porosity and permeability on the fluid flow model in the cases 'Ki-non' and 'Equi-non', the two cases have overlapping saturation profiles even near the saturation front. But for the cases 'Ki-cou' and 'Equi-cou' where the interaction between the fluid flow and the changes in porosity and permeability is included, the porosity and permeability would experience a small percentage of decrease for both 'Ki-cou' and 'Equi-cou' and therefore the domain before the saturation front would have a slightly larger CO_2 saturation than the non-coupling cases do although the saturation values seem to have no noticeable difference from the non-coupling cases in the top graph. The domain before the saturation front has a decreased porosity and permeability, resulting in a higher pressure before the saturation front while no changes for porosity and permeability are expected after the saturation front (no SO_2 and CO_2 yet) and pressure changes after the saturation front would not be so significant. Therefore, the flow velocity near the saturation front would be much larger than those for non-coupling cases. That is why the saturation difference between the coupling and non-coupling cases become

noticeable near the saturation front. Therefore, CO_2 saturation in the case 'Ki-cou' has a higher value that those in the non-coupling cases at the same location near the saturation front while CO_2 saturation in the case 'Equi-cou' has an even higher value. The decrease in the porosity for 'Equi-cou' is a little larger than that for 'Ki-cou' due to the fact that more SO_2 for 'Equi-cou' would produce more H^+ in the water and both the dissolution of hematite and precipitation of pyrite are catalyzed by H^+, so CO_2 saturation has a even larger increase near the saturation front for 'Equi-cou'.

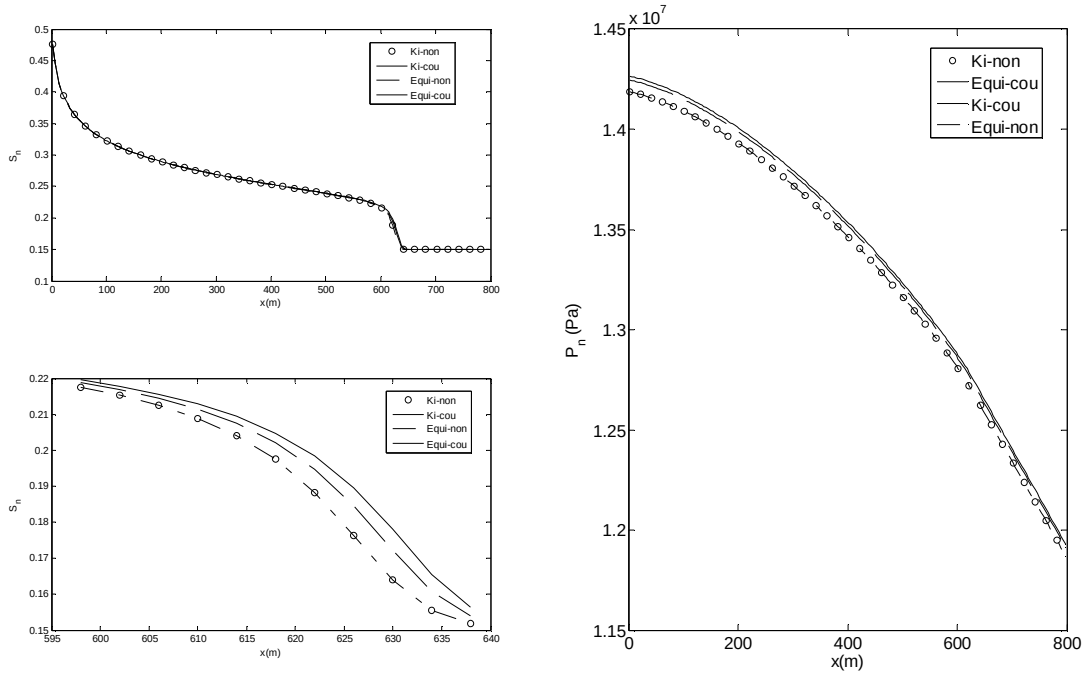

Figure 4.8 Comparison of the distribution for CO_2 saturation and pressure at 3.15e7 sec for different scenarios (in the legends, 'Ki' and 'Equi' are for kinetic and equilibrium mass transfer of SO_2 and CO_2 respectively; 'Cou' is for the case with the coupling between porosity change and fluid flow while 'Non' is without the coupling; the same legends are used throughout the paper)

When it comes to CO_2 pressure at 3.15e7 sec, no difference would be expected between 'Ki-non' and 'Equi-non' (shown in the right graph in Figure 4.8) because porosity and permeability changes are only monitored and not incorporated into the fluid flow model. As for the 'Ki-cou' case, a noticeable increase in CO_2 pressure over the non-coupling cases can be easily observed in the figure while 'Equi-cou' has an even larger

increase in the CO_2 pressure due to its larger magnitude of the decrease in porosity and permeability.

The major difference between the coupling and non-coupling cases is the pressure difference, which is in an order of less than 10^5 Pa, as is shown in Figure 4.8 and 4.10. Such magnitude of pressure difference would have minor direct impacts on the SO_2 solubility in the water phase and limited indirect impacts on the contaminant transport and geochemical model through the minor differences in the fluid flow velocity. Therefore, the impacts of the coupling between fluid flow and porosity change on the SO_2 and H^+ concentration in the aqueous phase would be insignificant, as can be seen in Figure 4.9. The H^+ concentration profiles for the coupling cases have no noticeable differences from those for the non-coupling cases, but the differences between kinetic and equilibrium mass transfer of SO_2 is obvious even after one year because more SO_2 dissolved into the water phase for the same time period can produce more H^+, although the difference is smaller and smaller as the time continues.

As we can see from Equation (4.14a) and (4.15a), the kinetic reactions for both the dissolution of hematite and the precipitation of pyrite can be accelerated by the presence of H^+ (the more of H^+, the faster for the reactions). Therefore, the magnitude for the changes in porosity and permeability for the case 'Equi' would be larger than that for 'Ki', as can be observed in Figure 4.9.

Since the injecting node (Node 1) is very important to CO_2 injection and storage, the evolution of several important variables will be presented and compared among the four scenarios. As to CO_2 saturation in the first node, no noticeable difference can be observed among the four scenarios, as can be seen in the TL graph in Figure 4.10, although the saturation for the coupling cases would be slightly larger than those for the non-coupling cases. When it comes to CO_2 pressure in Node 1, the difference is obvious (shown in the TR, LL and LR graphs). The pressure difference between the coupling and non-coupling cases is in an order of 10^4 Pa and the pressure for coupling cases would experience an increase of more than 0.1% over the non-coupling cases for most of the simulation time. At the end of one year, the case 'Equi-cou' has a pressure increase of 78119 Pa (0.55%) over the non-coupling cases while the increase for the case 'Ki-cou' is 58669 Pa (0.41%). From the comparison between 'Equi-cou' and 'Ki-cou', we can find

that the case with the kinetic mass transfer of SO_2 can save energy and money for the pressure difference of 19450 Pa over the case with equilibrium assumption at the end of one year.

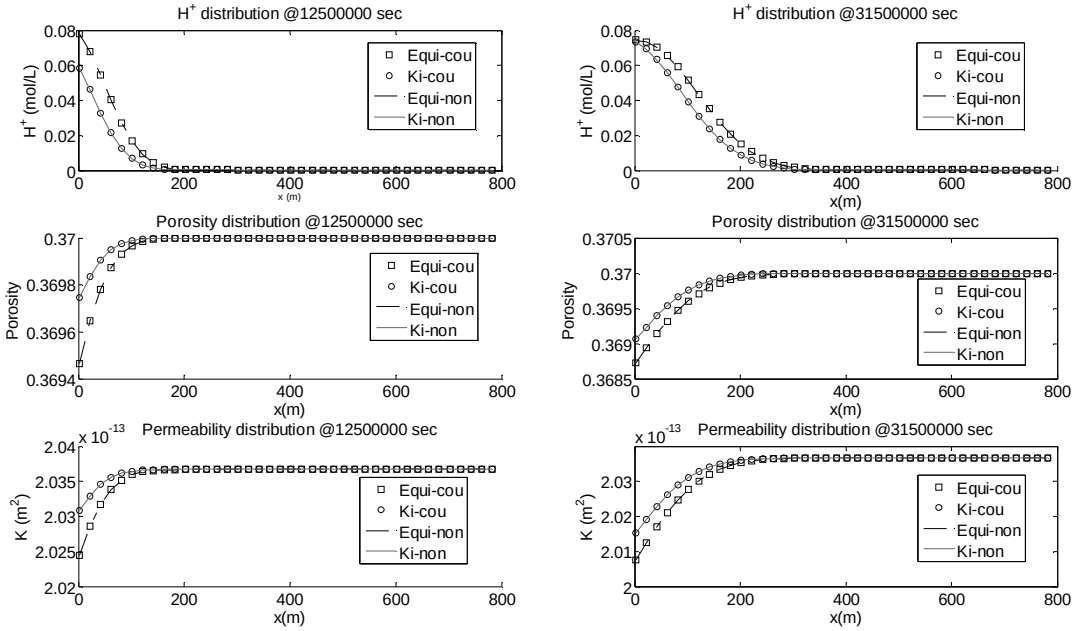

Figure 4.9 Comparison of the distribution for H^+ concentration, porosity and K changes for different scenarios

Higher pressure requirement would first demand more energy. Assuming that the pressure difference of the case 'Equi-cou' over the non-coupling cases continues to be 78119 Pa for the rest injection period (at least 20 years) and the CO_2 injection rate for the whole field is 0.73 m^3/s, there would be an additional power input requirement of 57 kilowatt to inject the same flow rate of CO_2 for the whole injection period, not even to mention that the pressure difference will definitely continue to increase if the porosity and permeability in the injection node continues to decrease. However, the assumption for the kinetic mass transfer of SO_2 can save this additional energy demand by about 25% because the magnitude of the decrease in the porosity and permeability would be smaller than that for the case with the assumption of equilibrium dissolution of SO_2 into the water phase.

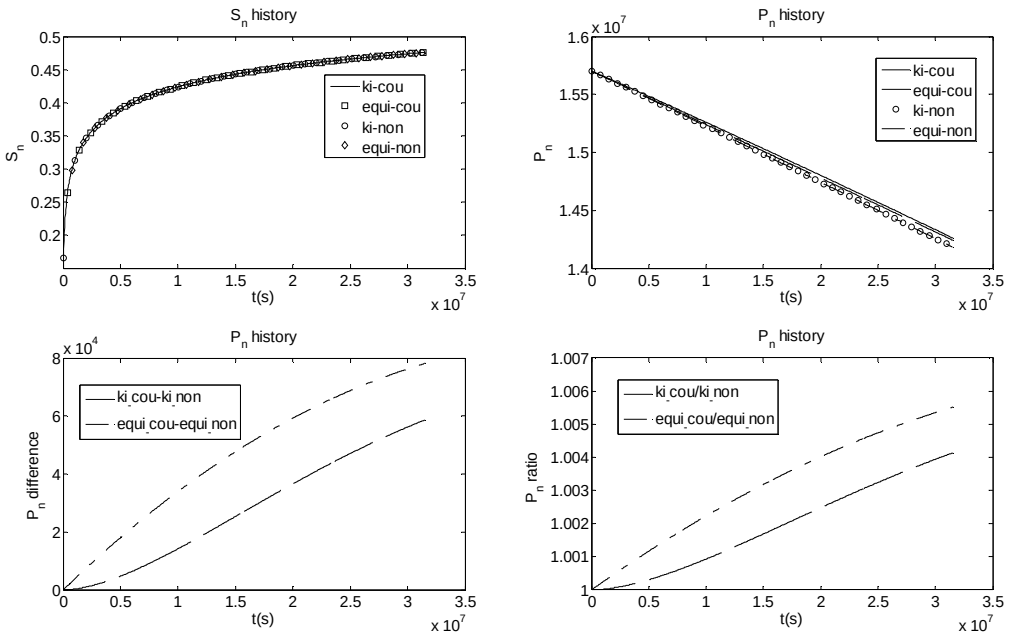

Figure 4.10 Comparison of the evolution for CO_2 saturation and pressure @ Node 1 (the LL graph shows CO_2 pressure difference between 'ki-cou' and 'ki-non', and between 'Equi-cou' and 'Equi-non' while the LR graph shows CO_2 pressure ratio of 'ki_cou' over 'ki_non', and of 'Equi-cou' over 'Equi-non')

As can be seen in the TL graph in Figure 4.11, the SO_2 concentration for the case 'Ki-cou' reaches its solubility limit at the end of one year, so is the H^+ concentration (TR graph in Figure 4.11). As we can find in the lower two graphs, the porosity experiences a maximal decrease percentage of 0.25 and 0.34 for the cases 'Ki' and 'Equi', respectively, while the maximal decrease percentage for the permeability is 1.05 and 1.43 for the cases 'Ki' and 'Equi', respectively, in the first node at 3.15e7 sec. Although the magnitude of the changes in the porosity and permeability seems to be small, they do have significant impact on the flow pattern, especially the pressure for the two phases, as is analyzed above.

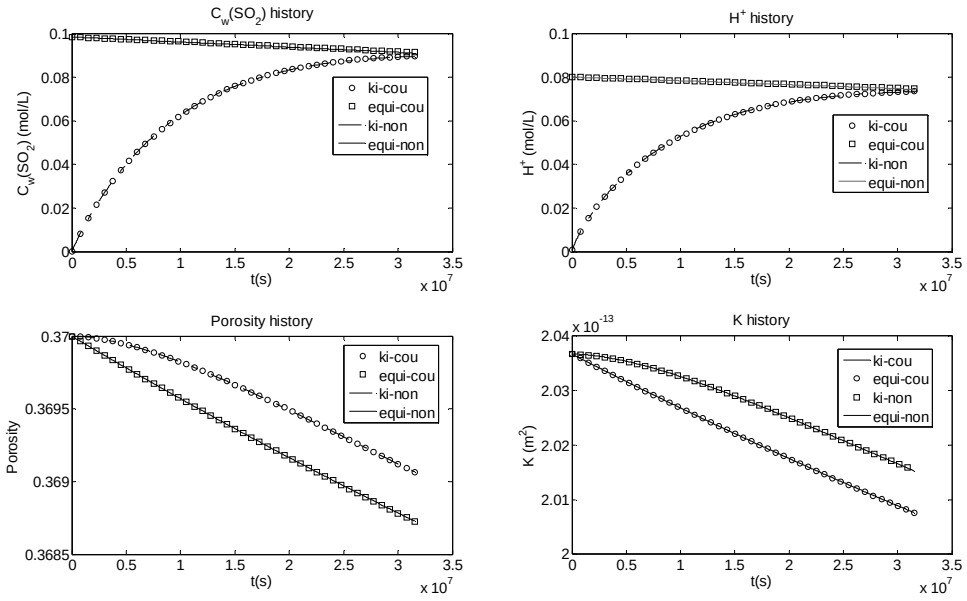

Figure 4.11 Comparison of the evolution for selected variables @ Node 1

4.4.3 Sensitivity analysis

The purpose of the sensitivity analysis is to assess how uncertainties in mineral dissolution rates and the dissolution rate of SO_2 into the aqueous phase affect the alteration pattern of the system including the changes of CO_2 pressure, aqueous concentration for SO_2 and H^+ , the dissolution and precipitation of minerals and the induced changes in the porosity and permeability. Therefore, two additional simulations are run for the sensitivity analysis, one with the dissolution rate of SO_2 decreasing by an order of magnitude; the other with the hematite dissolution rate decreasing by an order of magnitude. The two cases are denoted as 'Low K_he' and 'Low K_SO_2' for decreasing hematite and SO_2 dissolution rate, respectively. Results obtained from the two sensitivity simulations are compared to the base case detailed in Section 4.4.1. The comparison for selected important variables in the injecting node is shown in Figure 4.12 and 4.13.

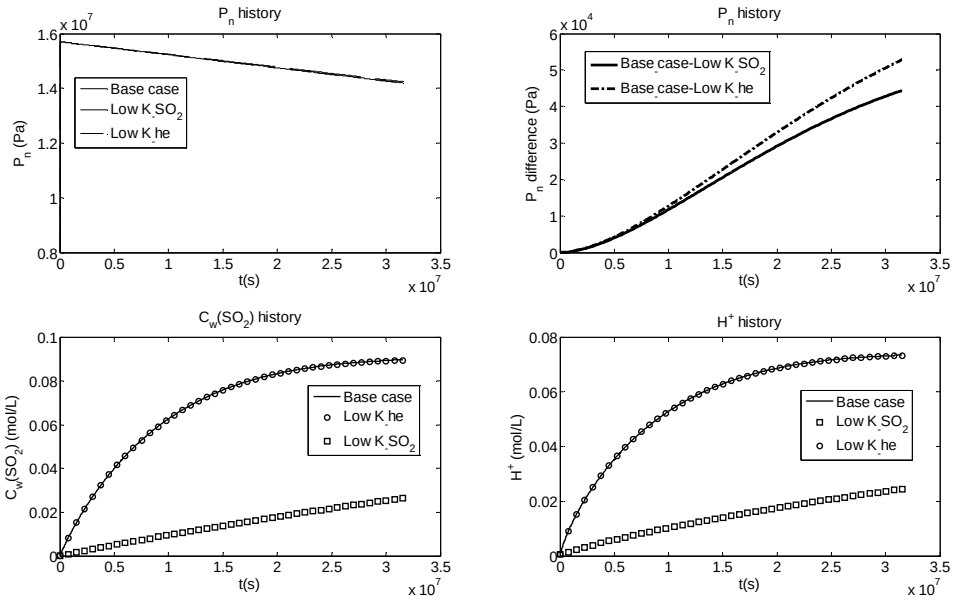

Figure 4.12 Comparison of the evolution for selected variables @ Node 1 for sensitivity analysis

From Figure 4.12, we can find that a decrease in SO_2 and hematite dissolution rate would result in a decrease in CO_2 pressure (the TR graph), compared to the base case, and the latter one would have a larger magnitude of decrease. This is due to the fact that hematite dissolution rate has a direct impact on the dissolution of hematite and the precipitation of pyrite, whose results are the induced changes in porosity and permeability and CO_2 pressure. However, for SO_2 and H^+ concentration in the aqueous phase, since SO_2 dissolution rate has a more direct impact on the dissolved SO_2 and H^+ in the water, it reduces SO_2 and H^+ concentration a lot while hematite dissolution rate have no notable effects, as can be seen in the LL and LR graphs.

The dissolution of hematite and precipitation of pyrite depend on hematite dissolution rate directly. The impact of SO_2 dissolution rate and H^+ is less direct. Therefore, the changes in the abundance for hematite and pyrite induced by the changes in hematite dissolution rate would expect a larger difference from the base case, as is shown in the TL and TR graphs in Figure 4.13. Since the porosity and permeability are changed due to the changes of hematite and pyrite, their alteration pattern is similar to that for hematite and pyrite, shown in the LL and LR graphs.

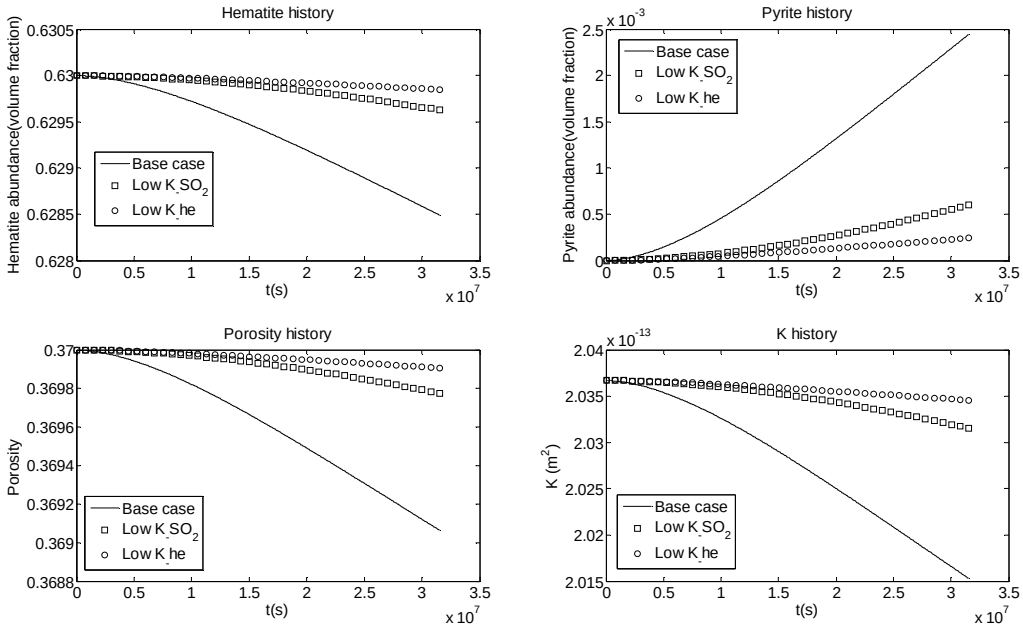

Figure 4.13 Comparison of the evolution for selected variables @ Node 1 for sensitivity analysis

To evaluate the impact due to variation of a parameter ϕ on the reaction that occurs during the simulation, we can define the following sensitivity indicator:

$$I_{\phi}^{x} = \frac{dx}{d\phi} = \frac{x - x_0}{x_0} \frac{\phi_0}{\phi - \phi_0} \tag{16}$$

where dx represents the percentage change of a variable x under estimation, $d\phi$ is the percentage change of a parameter ϕ with respect to the reference value ϕ_0. From the indicator, we can find that a positive indicator indicates increasing the parameter results in increasing variable while a negative indicator suggests that increasing the parameter results in decreasing variable, and a zero indicator shows no influence of the parameter on the variable.

The sensitivity indicator for selected important variables with respect to changes in hematite and SO_2 dissolution rate at the end of one year is summarized in Table 4.5. One important point needed to emphasize is that the change percentage for CO_2 pressure, hematite, porosity and permeability is very small (<1% for most cases). Therefore, the sensitivity indicator for these variables is very small (<0.01 in general), although the two parameters (K_he and K_SO_2) do have significant impact on these variables, as is

analyzed above and shown in Figure 4.12 and 4.13. As for SO_2 and H^+ aqueous concentration, K_SO_2 does have significant positive impact while K_he has a less significant effect.

Table 4.5 Sensitivity indicator with respect to changes in K_he and K_SO_2 at one year

I_ϕ^x	P_n	$C_w(SO_2)$	H^+	Hematite	Pyrite	Porosity	K
K_he	0.0041	0.0023	0.0021	-0.0024	0.9962	-0.0025	-0.0106
K_SO_2	0.0035	0.7836	0.7404	-0.0020	0.8384	-0.0021	-0.0089

4.5 Model limitations

The simulations presented in this study provide valuable insights with respect to the brine acidification and induced porosity and permeability changes of co-injecting SO_2 with CO_2 into deep saline aquifers. The results are, however, constrained by the limitations of current fluid flow, mass transport and geochemical models. Of all the complex physical, hydrological and geochemical processes which are expected to occur, some have not been incorporated in the models. Some simplifications can be justified, because they would not contribute significantly to the final outcomes; others, while important, would require a more thorough and detailed comprehension and quantification of relevant physical, kinetic, and thermodynamic processes than are currently available. In other words, more experimental studies and further model and code development are needed to fill the gaps in our knowledge. In this section, we prefer to devote some efforts to discuss some of the principal simplifications and how they might affect the findings presented in this paper.

The current model is limited in that the initial mineral composition of the formation is 100 wt% of hematite (Fe_2O_3). No other minerals are considered because of the computational demand required by the solving of the fluid flow and mass transport equations and iterative process required by the coupling between the fluid flow and porosity and permeability changes. The simplification may seems to be not that realistic, but it would not affect the findings in this study a lot since the objectives of this paper is to investigate the effects of kinetic versus equilibrium mass transfer of SO_2 and the coupling versus non-coupling between the fluid flow and porosity and permeability changes by comparing different model scenarios. However, since only one mineral is

considered, the pH buffering capacity of the minerals is underestimated and thus the estimated H^+ concentration is the maximal possible ones. Therefore, the results for a single scenario can only be interpreted as the 'worst-case scenario' if the results are to be compared to those in other studies.

Although this study incorporates the kinetic mass transfer of SO_2 from $scCO_2$ to the water phase, the kinetic reaction rate for the homogeneous disproportionation of SO_2 (given in Table 4.1) in the aqueous phase is not included due to lack of experimental data. In the current model, disproportionation is assumed to be instantaneous, approximating the conditions in which sulfuric acid generation is observed in magmatic hydrothermal systems as confirmed by laboratory experiments (Kusakabe et al., 2000). If the data for the kinetic reaction rate for the homogeneous disproportionation of SO_2 were available and incorporated into the geochemical model, then the difference between the kinetic and equilibrium dissolution would be larger. This could be a major uncertainty to the findings in this paper and needs further experimental studies and numerical investigations.

4.6 Summary

We have developed a multiphase flow and contaminant transport model which incorporates the kinetic mass transfer of SO_2 and CO_2 into deep saline aquifers and the coupling between the fluid flow and the induced porosity and permeability changes caused by the brine acidification. We have performed six simulations (four for model comparison, the other two for sensitivity analysis) of acid-gas injection into a 1-D formation with typical hydro-geologic properties and simplified mineral compositions. Major findings and conclusions are as follows:

i. The co-injection of SO_2 with CO_2 results in a substantially acid zone near the injecting well. For the base case by the end of one year, the H^+ concentration in the injecting node is 0.073mol/L and the region with H^+ concentration larger than 0.04mol/L expands to a distance 100 meters from the injecting node. The reasons for the relatively fast expansion of the acid zone can be attributed to the fact that the simplified initial mineral composition does not have enough pH buffering capacity as other complex mineral composition does.

ii. It is not necessary to include the kinetic dissolution of CO_2 from the $scCO_2$ to the water phase into the simulation models since the CO_2 concentration would reach its solubility limit in a time scale of several days. Therefore, for simulations with a time scale larger than weeks, it is valid to assume equilibrium dissolution of CO_2 from the $scCO_2$ to the aqueous phase.

iii. It is important to include the kinetic dissolution of SO_2 from the $scCO_2$ to the water phase into the simulation models because the SO_2 concentration in the aqueous phase would not be close to its solubility limit for the first node until the end of one year. The accumulated effect of the difference between the actual SO_2 concentration in the aqueous phase and its solubility limit would be considerable and can not be neglected.

iv. The coupling between the fluid flow and the changes in porosity and permeability is critical to the CO_2 injection into deep saline aquifers in that the coupling would require significantly higher injection pressure and higher pressure all over the domain, although the coupling has no noticeable effects on the SO_2 concentration, H^+ concentration and the induced porosity and permeability changes.

v. The porosity experiences a maximal decrease percentage of 0.25 and 0.34 for the cases 'Ki' and 'Equi', respectively, while the maximal decrease percentage for the permeability is 1.05 and 1.43 for the cases 'Ki' and 'Equi', respectively, in the first node at 3.15e7 sec.

vi. The pressure difference between the coupling and non-coupling cases is in an order of 10^4 Pa and the pressure for coupling cases would experience an increase of more than 0.1% over the non-coupling cases for most of the simulation time. At the end of one year, the case 'Equi-cou' has a pressure increase of 78119 Pa (0.55%) over the non-coupling cases while the increase for the case 'Ki-cou' is 58669 Pa (0.41%). The case with the kinetic mass transfer of SO_2 can save energy and money for the pressure difference of 19450 Pa over the case with equilibrium assumption at the end of one year.

vii. The higher pressure required would first demand higher injection pressure which would cost more energy and money. More importantly, the higher

injection pressure (may increase as the injection continues) would expose the whole domain to a higher pressure by a difference of 10^4 Pa at least. Higher pressure exposure would increase the risk of fracturing the domain and CO_2 leakage into the atmosphere.

viii. The initial mineral composition is simplified and the important pH buffering capacity of complex mineral composition is not included in this study. Therefore, the results for a single scenario in this study can only be interpreted as the 'worst-case scenario'.

ix. A comprehensive cost-benefits analysis is needed for SO_2 disposal with CO_2 in deep saline aquifers. Possible benefits include the save for SO_2 treatment and disposal with other options and the save for the purification cost associated with more pure CO_2. However, the major cost comes from the cost associated with the increasing injecting pressure, the loss due to increasing pipeline erosion, and the loss related to the increasing risk of CO_2 and SO_2 leakage.

x. The hematite and SO_2 dissolution rates have significant impact on CO_2 pressure, hematite and pyrite abundance, porosity and permeability. As for SO_2 and H^+ aqueous concentration, K_SO_2 does have significant positive impact while K_he has a less significant effect.

The simulations of SO_2 co-injection with CO_2 presented in this paper are preliminary, as they are limited by model simplifications due to insufficient thermodynamic data, kinetic and physical data, and limited computational power. Further experimental studies and numerical investigations will be required, although the direction of such improvements will depend on future CO_2 sequestration programs. Sensitivity studies show that arbitrary changes in SO_2 dissolution rate, or the representation of more complex but more realistic mineral dissolution kinetics, can significantly modify the predicted brine acidification and induced porosity and permeability changes.

Chapter 5 Investigation of Darcy-Forchheimer flow and kinetic dissolution of SO_2 during SO_2 co-injection with CO_2

In this chapter, the method and models developed in Chapter 3 and 4 are used for the investigation of the transition behavior between Darcy and Forchheimer flows and the kinetic dissolution of SO_2 and its resultant brine acidification and induced porosity and permeability changes during SO_2 co-injection with CO_2 into a large 2-D deep saline aquifer.

5.1 Introduction

As is concluded in Chapter 3, it is important to incorporate Forchheimer effect into the numerical simulation of multiphase flow to properly characterize the additional friction caused by the high flow rate of carbon dioxide (CO_2) and the Forchheimer zone near the injection well has a higher displacement efficiency but with the price of higher injection pressure. In order to obtain more realistic recommendations on the field operation of CO_2 sequestration sites, it is necessary to conduct a thorough investigation which incorporates the transition between Darcy and Forchheimer flows on a larger domain (length scale: kilometers) for a longer time (time scale: tens of years), rather than a small spatial and time scale considered in Chapter 3. Therefore the procedure and methods developed in chapter 3 will be employed here to investigate the transition behavior between Darcy and Forchheimer flow during CO_2 injection into a larger saline aquifer for a longer period of time.

At the same time, the kinetic dissolution of sulfur dioxide (SO_2) and its resultant brine acidification and induced porosity and permeability changes during SO_2 co-injection with CO_2 will also be investigated by using the models developed in Chapter 4. Lessons learned from Chapter 3 and 4 will act as the guideline for the analysis in this chapter. For example, from Chapter 4, a conclusion is drawn that it is not necessary to include the kinetic dissolution of CO_2 from the supercritical CO_2 ($scCO_2$) to the water phase into the simulation models since the CO_2 concentration would reach its solubility limit in a time scale of several days. Therefore, for the simulation here, the equilibrium dissolution of CO_2 from the $scCO_2$ to the aqueous phase is assumed in order to eliminate

the transport equation for CO_2 and save some computation time. As for the SO_2 dissolution, since the accumulated effect of the difference between the actual SO_2 concentration in the aqueous phase and its solubility limit would be considerable, kinetic mechanism is assumed. The simulation is also with the coupling between the fluid flow and the changes in porosity and permeability because the coupling is critical to the CO_2 injection into deep saline aquifers in that the coupling would require significantly higher injection pressure and higher pressure all over the domain.

The goal of this chapter is to gain a more thorough understanding of the transition behavior between Darcy and Forchheimer flow and the kinetic dissolution of SO_2 and its resultant brine acidification and induced porosity and permeability changes during SO_2 co-injection with CO_2 in deep saline formations. With this goal, three model scenarios are studied. The base case describes sSO_2 mass transfer limitation from $scCO_2$ to the brine with the assumption of Darcy-Forchheimer flow while the second scenario is for Darcy flow only and kinetic dissolution of SO_2. For comparison, the third scenario is for the case of Darcy-Forchheimer flow and SO_2 phase equilibrium between the entire volumes of $scCO_2$ and brine.

5.2 Fluid flow and contaminant transport conditions

A two-dimensional uniform formation is considered in the present model (Figure 5.1). In all scenarios, a constant flow rate of CO_2 with 1% of SO_2 in mass (10^{-3} m^3/s per meter normal to the 2D domain) is continuously injected into the middle bottom (at the node with (x, z) equal to (2510, 10) of a deep saline aquifer which is originally saturated with water and with a depth of 1000 m at the bottom boundary. The injection rate is determined by considering that a standard size 1,000-MW coal-fired power plant produces CO_2 at a rate approximately 350 kg/s (Hitchon, 1996), equivalent to 0.73 m^3/s CO_2. The CO_2 emitted would require a field about 730 meters in width (10^{-3} m^3/s per meter x 730 m =0.73 m^3/s). The boundary conditions and parameter values used here are shown in Table 5.1 and 5.2.

5.3 Geochemical conditions

Since the multiphase flow and contaminant transport model proposed in this chapter involves solving two linear systems in two iterative processes (plus the iterative process for the coupling between fluid flow and porosity changes) in a large domain with a total of 5010 grid points, which are computationally demanding, we still simplify the geochemical model by assuming that the initial mineral composition of the formation is 100 wt% of hematite (Fe_2O_3) with a density of 5280 kg/m^3, the same with that in Chapter 4.

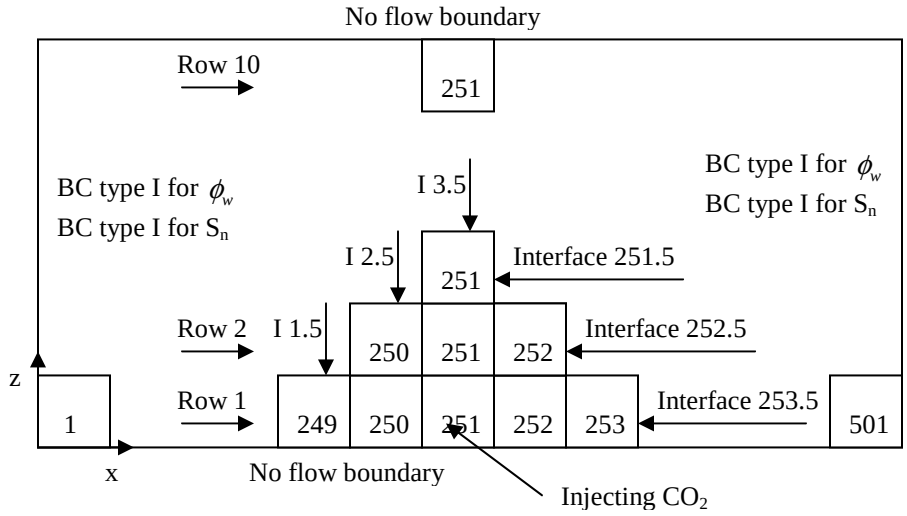

Figure 5.1 Model domain and boundary conditions (to represent a node, e.g., the injecting node (in Column 251 and Row 1) can be expressed as node (251, 1); for an interface, the east and north interfaces of the injecting node can be represented as (251.5, 1) and (251, 1.5), respectively)

Table 5.1 Parameters for fluid flow and contaminant transport

k	S_w^r	λ	ρ_w	μ_w	C_β	Aquifer temperature	Aquifer salinity	$D_{(CO_{2(aq)})}$	Droplet diameter (d)
m^2			kg/m^3	Pa s	(m)	°C	mol/L	m^2/s	m
2e-9	0.35	3.86	994	7.43e-4	1.52e-4	60	1	2.73e-9	0.05
θ	S_n^r	Pd	ρ_n	μ_n	Depth	$D_{(SO_{2(scCO_2)})}$	$D_{(SO_{2(aq)})}$	SO_2 mass ratio in scCO2 flow	
		Pa	kg/m^3	Pa s	m	m^2/s	m^2/s	percentage	
0.37	0.05	10000	479	3.95e-5	1000	2.49e-8	2.31e-9	1	

Table 5.2 Modeling parameters

Properties	*Values*	Comment
Boundary condition		
Water potential at x=5 m	ϕ_w = 10 M Pa, BC Type I	Left boundary
Water potential at x=5015 m	ϕ_w = 10 M Pa, BC Type I	Right boundary
Water potential at z=5 m	No flow boundary	Bottom boundary
Water potential at z=105 m	No flow boundary	Top boundary
SO_2 concentration at x=5 m	C = 0, BC Type I	Left boundary
SO_2 concentration at x=5015 m	C = 0, BC Type I	Right boundary
SO_2 concentration at z=5 m	No flow boundary	Bottom boundary
SO_2 concentration at z=105 m	No flow boundary	Top boundary
CO_2 saturation at x=5 m	S_n = 0.1, BC Type I	
CO_2 saturation at x=5015 m	S_n = 0.1, BC Type I	
CO_2 saturation at z=5 m	No flow boundary	
CO_2 saturation at z=105 m	No flow boundary	
CO_2 injecting rate @ (251,1)	$1*10^{-3}$ m^3/s	Per meter normal to the 2D domain
Initial condition		
Water saturation	S_w = 0.9	Saturated with water initially
NWP saturation	S_n = 0.1	
Water pressure	ϕ_w = 10 M Pa	

Space discretization		**Time discretization**	
Domain size, Length	L=5010 m	Simulation time	T= 180 day
Domain size, Depth	W=100 m	Time step size	dt=7200 s
Domain size, Width	1 m		
Space step size	dx =dz=10 m		

`

Where sediments contain ferric iron, it must be first reduced before precipitation as iron sulfide. The reduction of ferric iron by sulfide can be realized by the following reaction:

$$4Fe_2O_{3(s)} + HS^-_{(aq)} + 15H^+ \Leftrightarrow 8Fe^{2+} + SO_4^{2-} + 8H_2O \quad (5.1)$$

After the reduction of ferric iron to ferrous iron, ferrous iron can react with sulfide by the following reaction:

$$4Fe^{2+} + SO_4^{2-} + 7HS^-_{(aq)} + H^+ \Leftrightarrow 4FeS_{2(s)}(pyrite) + 4H_2O \quad (5.2)$$

After the formation of pyrite, it might begin to dissolve into the water phase, but the dissolution of pyrite needs the presence of Fe^{3+}, as is shown in Table 4.4. Furthermore, there would be few, if not at all, Fe^{3+} in the water phase in this study. Therefore, the dissolution of pyrite is negligible compared with the precipitation of pyrite.

Since the simulations considered herein are restricted to moderately to extremely acidic conditions, only the acid-catalyzed mechanism has a significant effect upon reaction rates, and the other two mechanisms are negligible in comparison and therefore are ignored herein. The mineral dissolution rate parameters are summarized in Table 4.4. Mineral precipitation rates were computed by dividing the dissolution rate by the equilibrium constant, based on the principle of microscopic reversibility (Lasaga, 1998).

5.4 Results and discussion

Three model scenarios are analyzed in this chapter, with the base case describing $scSO_2$ mass transfer limitation from $scCO_2$ to the brine with the assumption of Darcy-Forchheimer flow, and the second scenario for the case of Darcy flow and kinetic dissolution of SO_2, and the third scenario for the case of Darcy-Forchheimer flow and SO_2 phase equilibrium between the entire volumes of $scCO_2$ and brine. To simplify the notation, these three cases are denoted as 'F', 'D' and 'FE', respectively. This simplified notation will be used throughout the chapter.

In this section, the results for the base case with kinetic mass transfer and Darcy-Forchheimer flow will be presented and discussed first. Then a comparison among the three cases will be conducted. In addition, implications for CO_2 injection and storage in deep saline aquifers will be also discussed after that.

5.4.1 Base case (Case 'F')

Before presenting the results for the base case in 2D domain, it needs to be noted that there are four Forchheimer numbers noted as f_{wx} (for wetting phase in the x-axis direction), f_{nx} (for non-wetting phase in the x-axis direction), f_{wz} (for wetting phase in the z-axis direction) and f_{nz} (for non-wetting phase in the z-axis direction). Furthermore, it is important to note that all Forchheimer numbers and velocities are values evaluated at the individual interface between its two neighboring central nodes (vector quantity) while all

the other variables such as saturation and pressure are evaluated as values of central nodes (scalar quantity).

CO_2 saturation profiles are shown in Figure 5.2, from which it can be seen that the injected CO_2 at Node (251, 1) spread to the right and left hand side in a symmetric way. It is also easy to observe that, more CO_2 spread along the x direction than the vertical direction. For example, at Day 180 as is shown in the lower graph in Figure 5.2, the 0.16 saturation contour line has reached the points where x = 4800 m or 200 m with a travel distance of 2300 m while it has not hit the top boundary with a travel distance less than 100 m. In addition, a high-saturation profile is observed near the injecting node (251, 1). The high saturation contour line (e.g., 0.48) expands horizontally with time while it expands vertically from Day 45 (Top Middle (TM) graph) to Day 135 (Lower Middle (LM) graph), but stops expanding from Day 135 to time Day 180 (Lower graph).

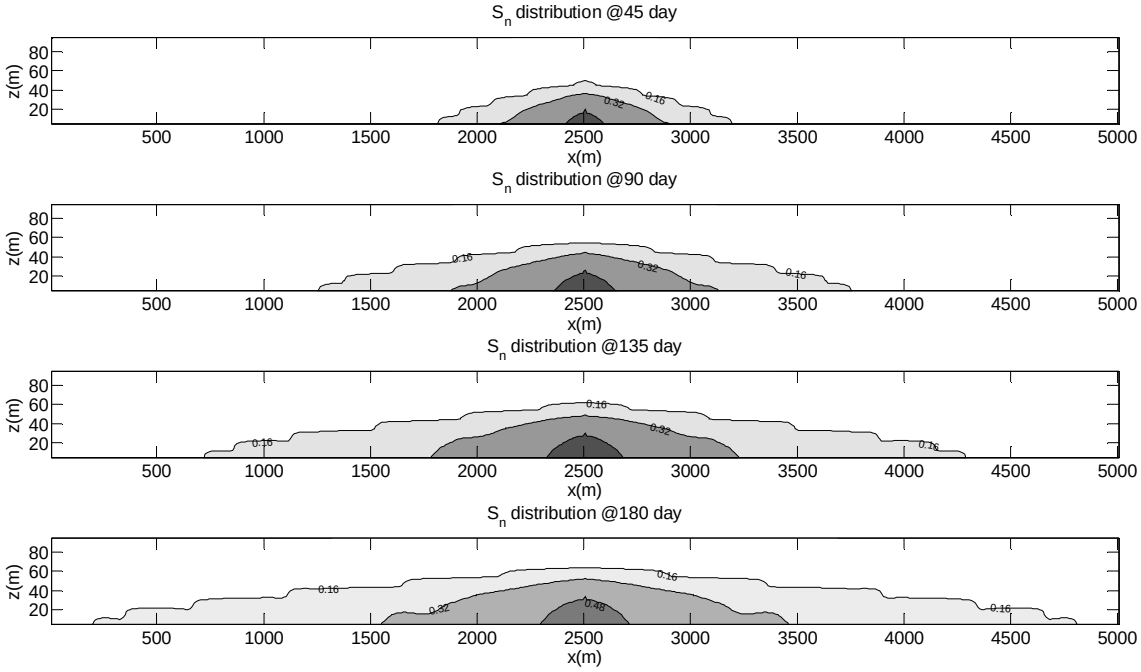

Figure 5.2 Spatial distribution of CO_2 saturation over time for Case 'F' (the Top, Top Middle (TM), Lower Middle (LM) and Lower graphs are for Day 45, 90, 135 and 180, respectively)

The reasons for the transport behavior of CO_2 as is shown in Figure 5.2 can be illustrated by a comparison among Figure 5.2, 5.3 and 5.4. Before that, the spatial distribution for the Forchheimer number in the x and z direction will be analyzed first.

Since f_{nx} is vector quantity evaluated at the interface between two neighboring nodes and the injecting node (Node (251, 1)) has two interfaces along the x direction, it can be observed from the Top Left (TL) graph in Figure 5.3 that Node (251, 1) has transitioned from Darcy flow to Forchheimer flow at its eastern and western interfaces at Day 3. In Darcy-Forchheimer flow as is defined in Section 3.3.5, a positive Forchheimer number indicates Forchheimer flow for the interface while a zero Forchheimer number suggests Darcy flow numerically. The Forchheimer region in the x direction expands to Node (251, 2) at Day 26 and further expands to Node (251, 3) at Day 104, but stops expanding from then on. Therefore, the Forchheimer number in the x direction expands vertically, but not horizontally. The reason for positive f_{nx} not expanding horizontally will be explained next.

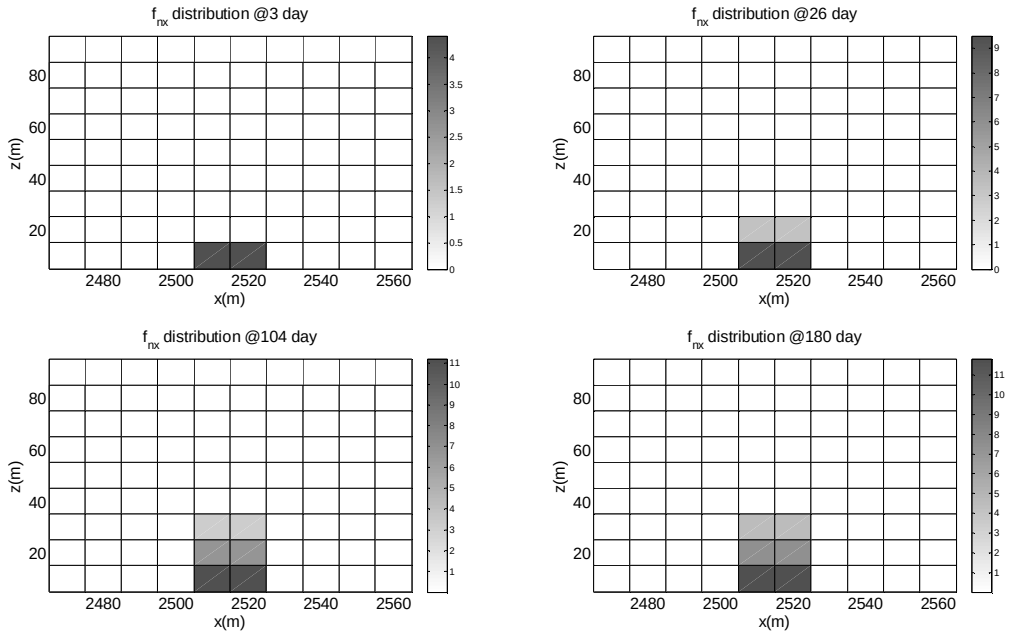

Figure 5.3 Spatial distribution of f_{nx} over time for Case 'F' (In the figure, white rectangles represent Darcy flow at the horizontal interface while grey rectangles stand for Forchheimer flow at the horizontal interface)

As for the spatial distribution for f_{nz}, the Forchheimer expansion is much faster than that for f_{nx}, as can be seen from Figure 5.4. Although positive f_{nx} only expands vertically to the third row @ Day 180, positive f_{nz} has already covered most of the lower half of the studied domain. As is pointed out by Wu (2001), Ahmadi et al. (2010) and Zhang et al. (submitted), the displacement of the water by CO_2 is inhibited by inertial effects in Forchheimer flow. Therefore both f_{nx} and f_{nz} will affect the transport of the injected CO2 at Node (251, 1) with f_{nx} inhibiting CO_2 from flowing horizontally and f_{nz} inhibiting CO_2 from flowing vertically and thus less CO_2 will flow out horizontally and vertically. Consequently, more and more CO_2 will be inhibited and accumulated in the region where f_{nx} and f_{nz} are positive (indicating Forchheimer flow) and the inhibition of CO_2 flow is both horizontal and vertical, as is shown in Figure 5.2 for the 0.48 saturation contour line whose evolution is consistent with the evolution of f_{nx} and f_{nz}. As for the other region with zero f_{nx}, the transport of CO_2 is majorly impacted by the evolution of f_{nz}. Actually, if one compares the profiles of CO_2 saturation in Figure 5.2 with f_{nz} distribution in Figure 5.4, the two profiles resemble each other strikingly.

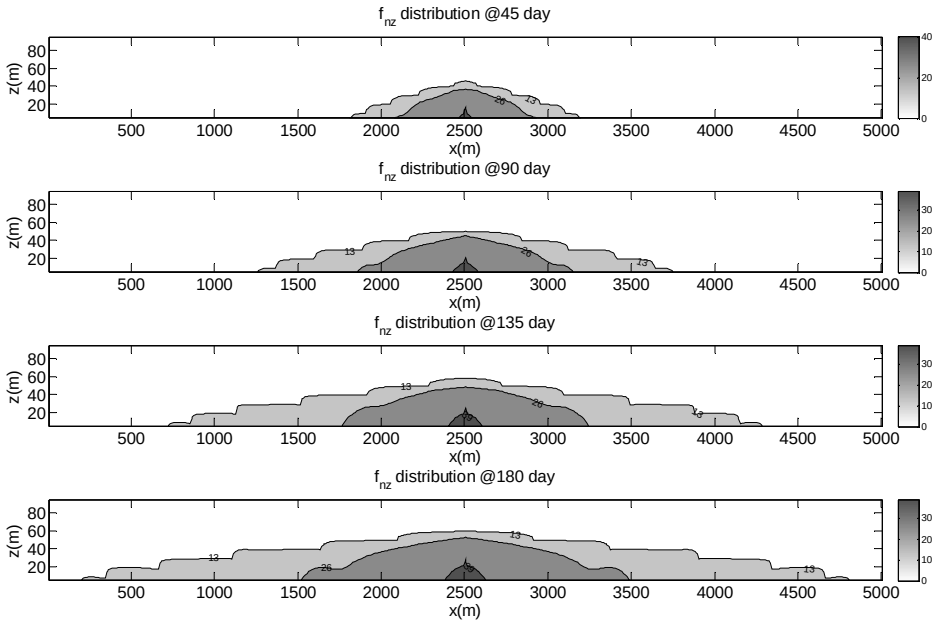

Figure 5.4 Spatial distribution of f_{nz} over time for Case 'F' (In the figure, white region represents Darcy flow at the vertical interface while grey region stands for Forchheimer flow at the vertical interface)

Since the profiles for f_{nz} share so much in common with those of CO_2, some may argue why the profiles of f_{nx} look so different from those of CO_2. The reason can be attributed to the reason why the Forchheimer expansion is much faster vertically than horizontally. When CO_2 is continuously injected to the middle bottom at Node (251, 1), the injected CO_2 will move preferentially upward over horizontally due to the buoyancy effects caused by the density and viscosity difference between the $scCO_2$ and the water phase and thus the vertical velocity is much higher than the horizontal one. The higher vertical velocity would cause a larger vertical Forchheimer number, indicating that the Forchheimer effect is much stronger vertically than horizontally. This point can be verified from Figure 5.5, which shows that both the vertical velocity and Forchheimer number are almost 4 times larger than the horizontal velocity and Forchheimer number, respectively. Therefore the stronger Forchheimer effect in the z direction caused by the buoyancy effects is the dominating factor which imposes on the migration of CO_2 while horizontal Forchheimer effects are only functional near the injecting well.

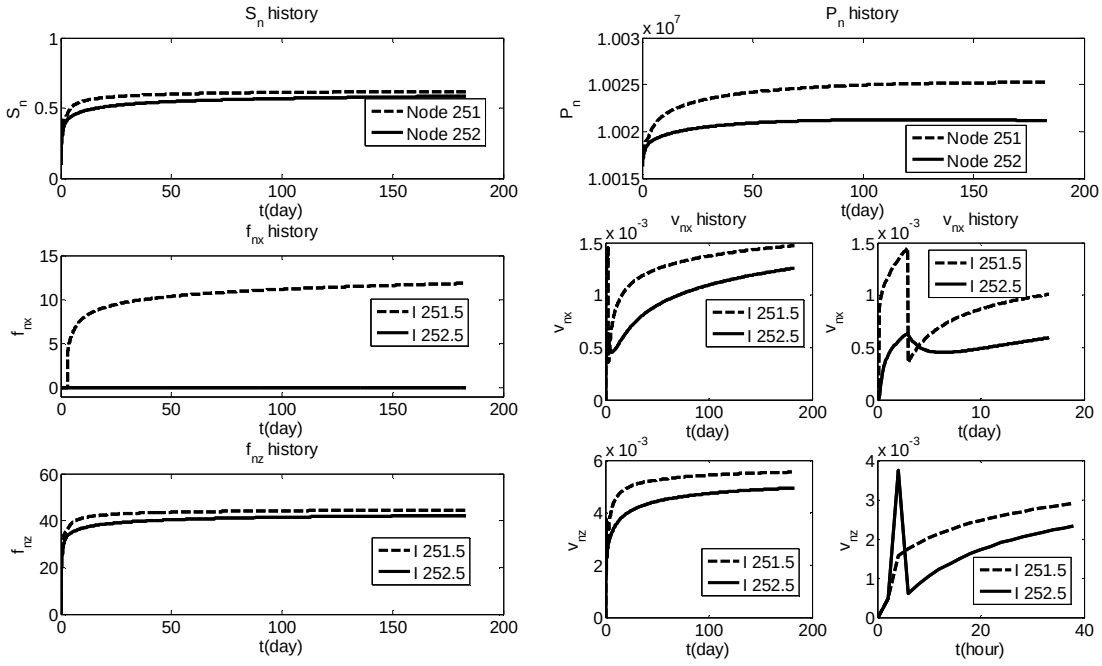

Figure 5.5 Temporal evolutions of important variables for Case 'F'in the first row

Since the vertical Forchheimer effect is much stronger vertically than horizontally, the inhibition of vertical flow of CO_2 will definitely take place where f_{nz} has the momentum to transition from Darcy flow to Forchheimer flow. This indicates that more

and more CO_2 will be accumulated in the node due to the vertical inhibition and the accumulation of CO_2 in the node would be more and more difficult with time progressing and some portion of the accumulated CO_2 will be pushed to move downstream and horizontally. Partially due to the much weaker horizontal Forchheimer effects which suggest less momentum for the transition, it would be more and more difficult for the horizontal interfaces to transition from Darcy flow to Forchheimer flow because the transition to Forchheimer flow indicates additional friction and less flow velocity which would otherwise cause more CO_2 to be accumulated in the node. Therefore, the weaker horizontal Forchheimer effects give way to the stronger vertical Forchheimer effects and thus positive f_{nx} do not expand horizontally, as is shown in Figure 5.3. Accordingly, it is clear that CO_2 spreading vertically is inhibited by the higher vertical resistance, leading to CO_2 spreading in favor of the x direction (shown in Figure 5.2).

As for the water phase, all the nodes' interfaces have a Forchheimer number less than the critical Forchheimer number (with all f_w set to be zero to account for the Darcian flow), which implies that water flow in the domain is Darcian with the specified injecting rate of CO_2. This could be attributed to the fact that water's movement is intrigued by the injection of CO_2 and the velocities of water are far less than those of CO_2 so that the Forchheimer number is smaller than the critical values.

Since the flow is symmetric in the x-direction, as is shown in Figure 5.2, it is enough to analyze the evolution of important variables for the right hand side. The evolution of CO_2 saturation (S_n), potential (P_n), Forchheimer number in the x direction (f_{nx}), horizontal velocity (v_{nx}), vertical Forchheimer number (f_{nz}) and vertical velocity (v_{nz}) for the bottom row is shown in Figure 5.5. Initially, CO_2 in all the nodes in the transport domain is in a Darcian manner with the injection of CO_2 at node (251, 1). Its east interface (251.5) waits until 72 hours (shown in the middle right graph in Figure 5.5) to transition to Forchheimer flow. The transition results in faster accumulation of CO_2 due to inertial effect and requires a higher pressure difference to overcome this additional friction. However, the east interface for node (252, 1) never realizes the transition because of the weaker horizontal Forchheimer effect yielding to the much stronger vertical Forchheimer effect. The transition for the upper interfaces of each node would require much less time when compared with the corresponding eastern and western

interfaces of the specified node due to the stronger Forchheimer effects resulted from the buoyancy effects. For example, the time required for the injecting node's upper interface to transition to Forchheimer flow is only 4 hours (shown in the lower right graph in Figure 5.5). Also, with the transition, there is a sharper increase in CO_2 saturation and pressure, as can be seen in the top left and top right graphs in Figure 5.5.

It is plausible from a first look at the v_{nx} and v_{nz} history in the middle right and lower right graphs in Figure 5.5 that the velocities are oscillating. However, a careful observation would refute the argument. The sharp decrease in the velocity history is due to the fact that the velocity before the transition is based on Darcy flow while the velocity after the transition is based on Forchheimer flow and the difference between the two regimes is by a factor of $(1+f_{nx})$ or $(1+f_{nz})$. If the velocity after the transition (e.g., 72 hours for v_{nx} of Interface 251.5) is depicted as Darcy flow by multiplying a factor of $(1+f_{nx})$ with the f_{nx} larger than 10, then there would not be a sharp decrease in the absolute value of velocity. In this discussion the analysis on water phase is skipped because the change in water phase is induced by the change in CO_2 and a complete analysis on CO_2 is adequate.

As to SO_2 concentration in the $scCO_2$, a constant mass ratio (one percent of SO_2 in the $scCO_2$) is assumed in the injecting well since SO_2 together with $scCO_2$ is continuously injected into Node (251, 1) and the mass transfer for SO_2 from the $scCO_2$ to the water phase has proven not to be fast enough to deplete the SO_2 in the $scCO_2$ in the injecting node. As is shown in Figure 5.6, SO_2 in the $scCO_2$ expands horizontally and vertically with time. It needs to be noted that it seems that the region beyond the most outside contour line in Figure 5.6 has zero concentration of SO_2, however this region does have very small concentration, for which the figure can not display them completely since the values are very small (close to zero). Figure 5.7 and Figure 5.8 have similar problems.

The SO_2 solubility in the water (shown in Figure 5.7) has a direct relationship with SO_2 concentration in the $scCO_2$, as is ruled by Henry's Law, so the profiles of SO_2 solubility in the water are similar to those for SO_2 concentration in the $scCO_2$. SO_2 concentration in the water (shown in Figure 5.8) has a time lag compared with the profiles of SO_2 solubility because of the mass transfer limitations. In addition, the actual SO_2 concentration in the water is a little smaller than the SO_2 equilibrium concentration

in the water because the buffering capacity of the mineral (in terms of sulfur and acidity consumption) keeps SO_2 concentration in the water from reaching its solubility limit.

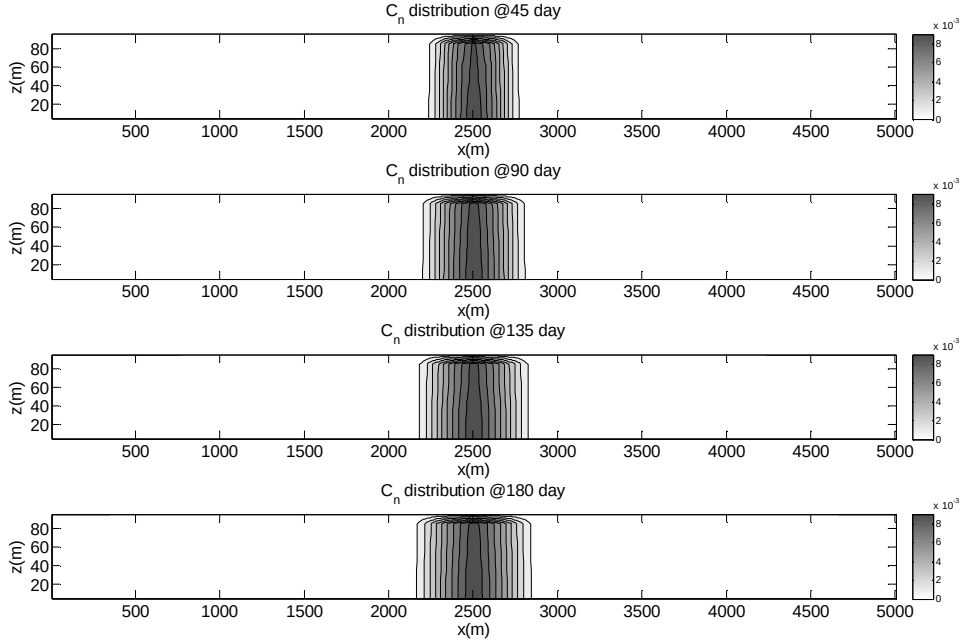

Figure 5.6 Spatial distribution of SO_2 mass ratio in the $scCO_2$ over time for Case 'F'

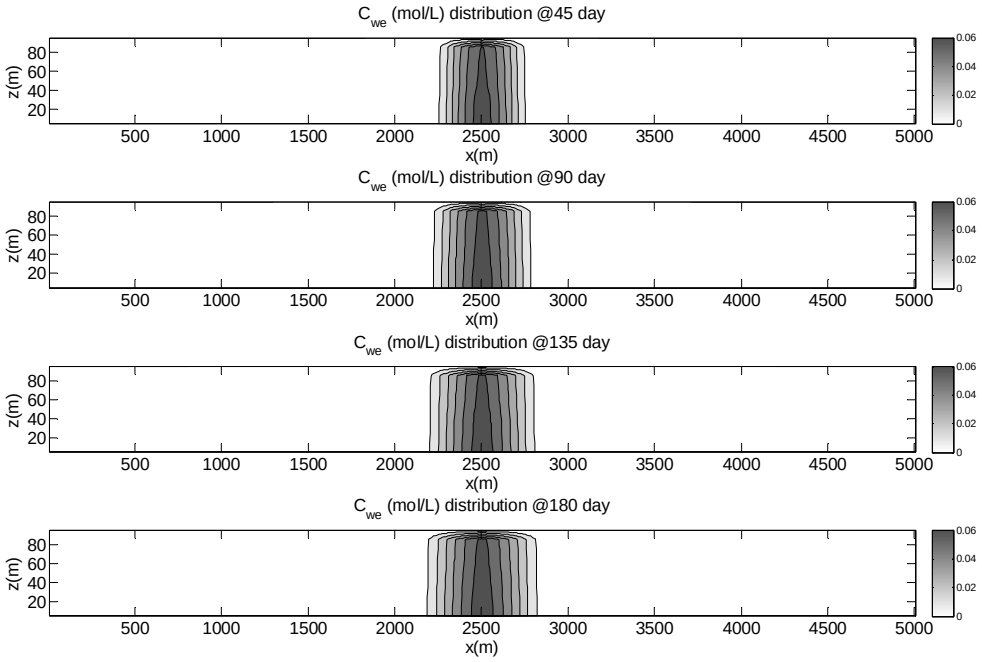

Figure 5.7 Spatial distribution of SO_2 equilibrium concentration over time for Case 'F'

It is more obvious to observe (in the middle right and lower right graphs in Figure 5.9) the time lag between SO_2 concentration in the water and SO_2 solubility in the water due to the mass transfer limitations from the $scCO_2$ to the water phase and small concentration difference between the two because of the mineral's buffering capacity. As is expected, SO_2 concentration in the $scCO_2$ and SO_2 solubility in the water share almost the same profiles in the top two and middle two graphs because of Henry's Law. As for the difference among the three nodes in the first row for SO_2 concentration in the $scCO_2$, SO_2 solubility and SO_2 concentration in the water, there is marginal difference since the advection and diffusion effects are strong compared to the simulation time in this study.

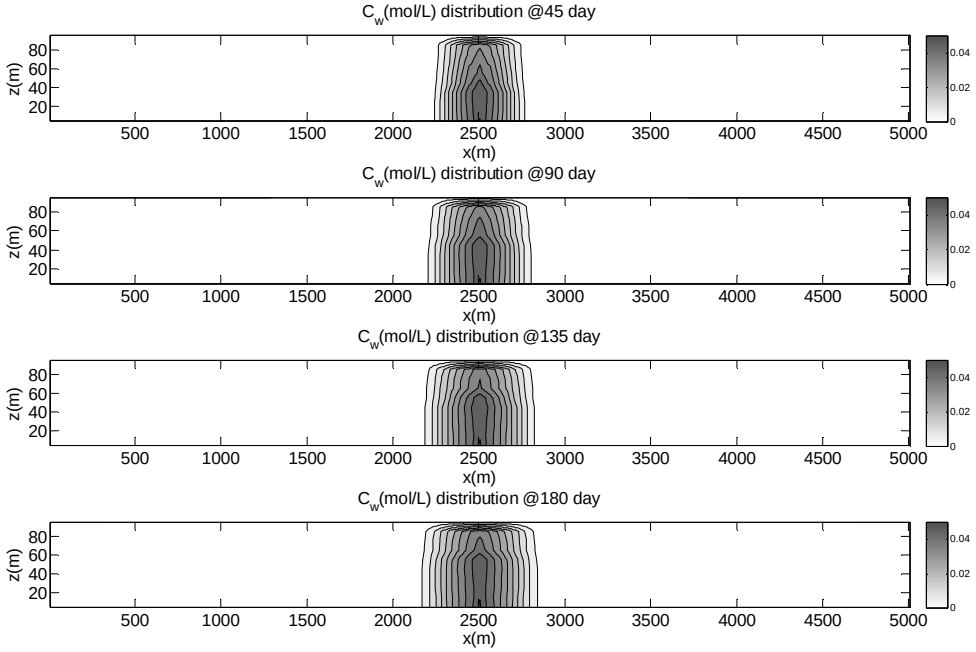

Figure 5.8 Spatial distribution of SO_2 aquatic concentration over time for Case 'F'

A comparison between Figure 5.8 and 5.10 can conclude that the profiles of H^+ have similar profiles with those for SO_2 concentration in the water since the concentration of H^+ is highly dependent of SO_2 concentration in the water.

As we can see from Equation (5.1) and (5.2), the kinetic reactions for both the dissolution of hematite and the precipitation of pyrite can be accelerated by the presence of H^+ (the more of H^+, the faster for the reactions). Therefore, the changes in the porosity and permeability (shown in Figure 5.11) induced by the mineral dissolution and

precipitation share similar profiles with those for H^+. The porosity experiences a maximal decrease percentage of 0.103 while the maximal decrease percentage for the permeability is 0.427 in the injecting node at Day 180. It needs to be noted that it seems that the region beyond the most outside contour line in Figure 5.10 has zero concentration of H^+, however this region does have very small concentration of H^+, for which the figure can not display them completely since the values are very small (close to zero). This small concentration does contribute to the dissolution of hematite and the precipitation of pyrite and the accumulated contributions become noticeable and thus the profiles for porosity in the x direction are wider than those for H^+ if one compares Figure 5.10 to Figure 5.11. The profiles for absolute permeability are similar with those for porosity and are not displayed here due to the fact that the change of permeability is based on the change in porosity according to Equation (4.13).

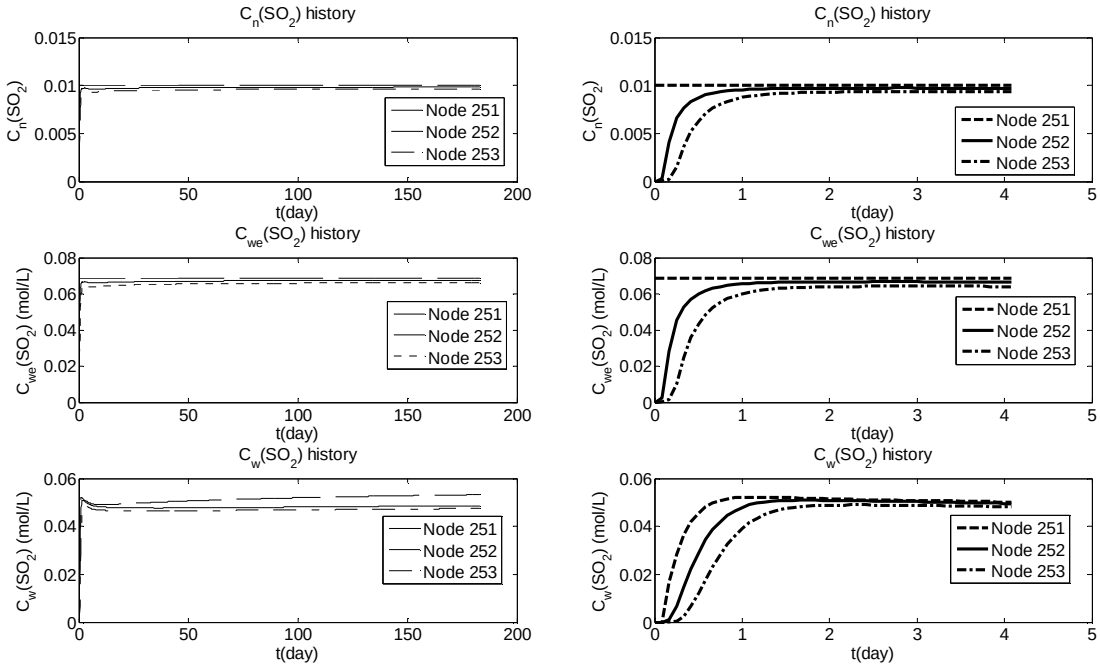

Figure 5.9 Temporal evolutions of important variables for Case 'F' in the first row

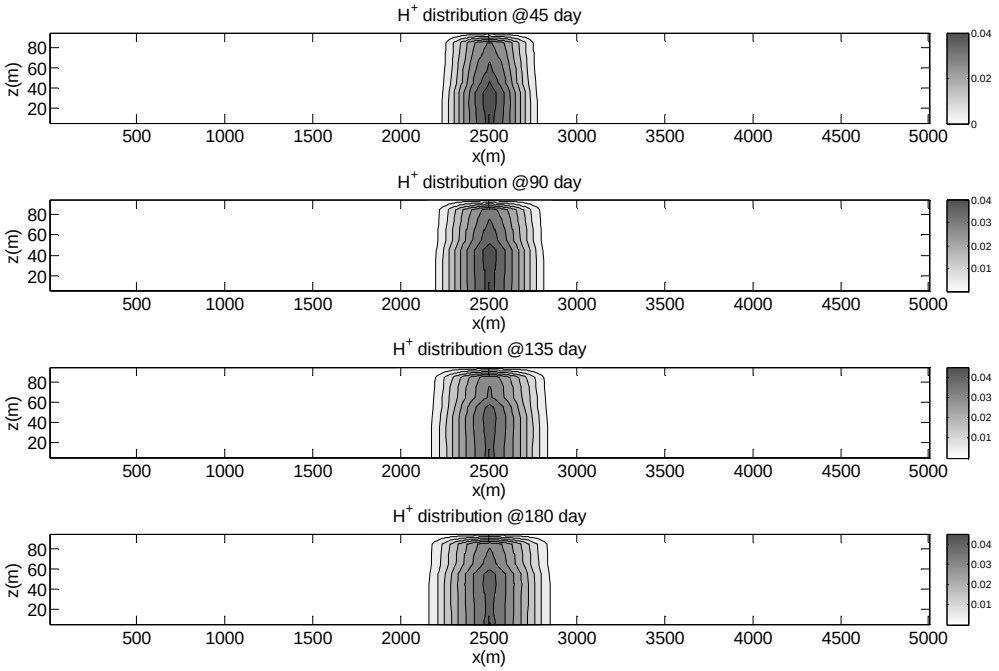

Figure 5.10 Spatial distribution of H^+ over time for Case 'F'

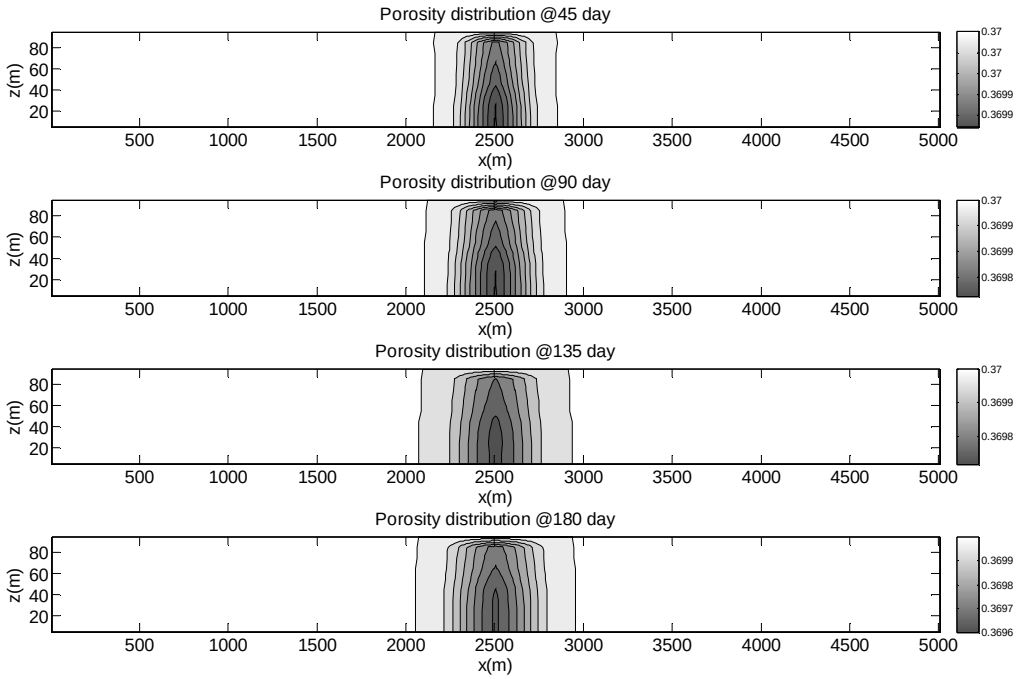

Figure 5.11 Spatial distribution of porosity over time for Case 'F'

As for the evolution for H^+ concentration in the top left graph in Figure 5.12, similar profiles can be found for SO_2 concentration in the water phase in the LL graph in Figure 5.9 because the concentration of H^+ is highly dependent of SO_2 concentration in the water. At the end of one half year, the porosity experiences a decrease percentage of 0.103, 0.096, and 0.094 for Node 251, 252, and 253 in the first row, respectively, as is shown in the middle left graph in Figure 5.12. This magnitude in the changes of porosity would have corresponding decrease percentage for the permeability (LL graph in Figure 5.12) of 0.427, 0.401, and 0.392 for Node 251, 252, and 253 in the first row, separately. The magnitude of the change might not be as significant as someone might expect, but the changes are for a simulation time of half a year only. The changes would be much more significant if an injection period of more than 30 years is considered. In addition, the combination of these minor changes in the porosity and permeability would have a collective impact that might be much more important than expected and therefore needs further investigations, especially on the water and CO_2 pressure because the pressures are very sensitive to the change of porosity and permeability and these pressures are very important operating parameters during CO_2 injection and storage.

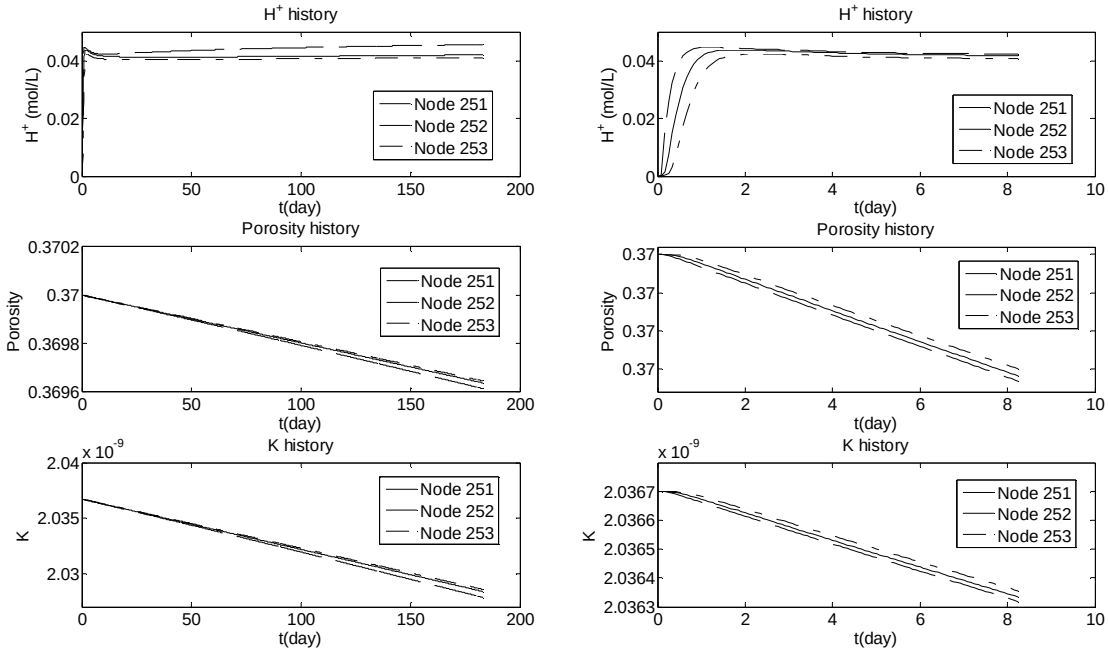

Figure 5.12 Temporal evolutions of important variables for Case 'F' in the first row

5.4.2 Model comparison

To observe the contrast between the solutions, the application presented above is simulated again with the same parameter values except that all four Forchheimer numbers are set to be zero to account for the complete Darcy flow condition in the domain, noted as Case 'D'. Another scenario is noted as Case 'FE' to represent Darcy-Forchheimer flow and SO_2 phase equilibrium between the entire volumes of $scCO_2$ and brine. The discussion here will focus mostly on the results with obvious difference among the three cases.

The CO_2 profiles for Case 'D' are shown in Figure 5.13. From a comparison between Figure 5.2 and 5.13, we can find that CO_2 spread in a more evenly way in Darcy flow when compared to Darcy-Forchheimer flow and a high-saturation profile in the Forchheimer region is observed and can be attributed to the additional friction caused by the inertial effect near the injecting node.

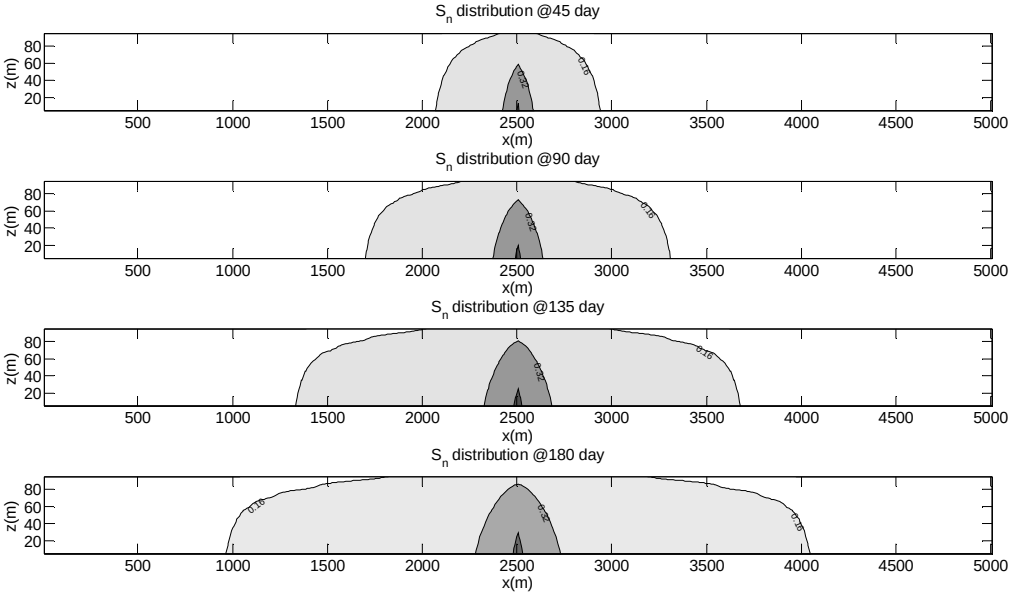

Figure 5.13 Spatial distribution of CO_2 saturation over time for Case 'D'

In addition, it is obvious that CO_2 flow preferentially along the x direction and most of the injected CO_2 are kept in the lower half of the studied domain for Darcy-Forchheimer flow whereas CO_2 flow preferentially along the vertical direction and the injected CO_2 are more evenly distributed near the injected well for complete Darcy flow.

The major difference in the CO_2 migration can be attributed to the much stronger Forchheimer effects as a result of the buoyancy effects due to the smaller density and viscosity of CO_2 compared with the brine.

As for the comparison for the flow pattern for Case 'FE' and 'F', no noticeable difference can be observed, as can be seen from the left half of Figure 5.14. For Case 'FE', CO_2 saturation, pressure and velocity for the two nodes in the first row overlay those for Case 'F', which indicates that the impact on the flow pattern of the difference between SO_2 kinetic dissolution and equilibrium assumption is minor under the conditions of the simulation in this chapter.

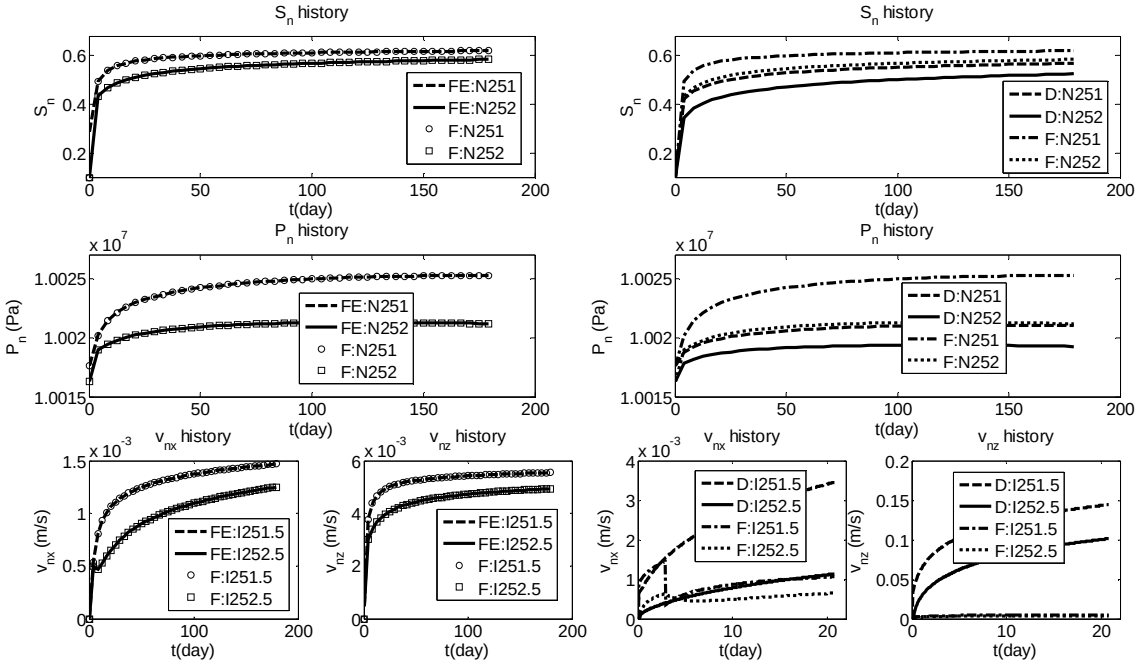

Figure 5.14 Comparison of the evolution for CO_2 saturation, pressure and velocity for nodes in the first row

It is clear that Forchheimer flow can result in higher CO_2 saturation near the injecting nodes, suggesting higher displacement efficiency, as is illustrated in the top right graph in Figure 5.14. But this higher displacement efficiency would require a higher pressure, which can be verified by comparing the pressure results of Darcy flow and Darcy-Forchheimer flow in the middle right graph in Figure 5.14. As for the velocity, the velocity after the transition is based on Forchheimer flow for Darcy-Forchheimer flow, so

its actual velocity is much larger than that of Darcy flow. One can easily conclude that Forchheimer effect can improve displacement efficiency but at the expense of a higher injection pressure and the stronger vertical Forchheimer effects as a result of the buoyancy effects can help keep more CO_2 horizontally at a larger distance to the overlying cap-rock. It is important to consider the inertial effect in near-wellbore area otherwise significant errors can be introduced to the modeling.

The profiles for SO_2 aquatic concentration over time for Case 'D' are shown in Figure 5.15. A comparison between Figure 5.8 and 5.15 can lead to the fact that SO_2 concentration profiles for Case 'D' are more uniform vertically and horizontally and the transport speed of SO_2 along the x direction is slower than that for Case 'F'. The underlying reason is the difference in the migration behavior of the injected CO_2. Due to the Forchheimer effect and the buoyancy effect, CO2 will migrate preferentially along the x direction over the vertical direction in Case 'F'; therefore, more SO_2 will be dissolved into the brine horizontally, resulting in a wider SO_2 aquatic concentration profiles in the x direction.

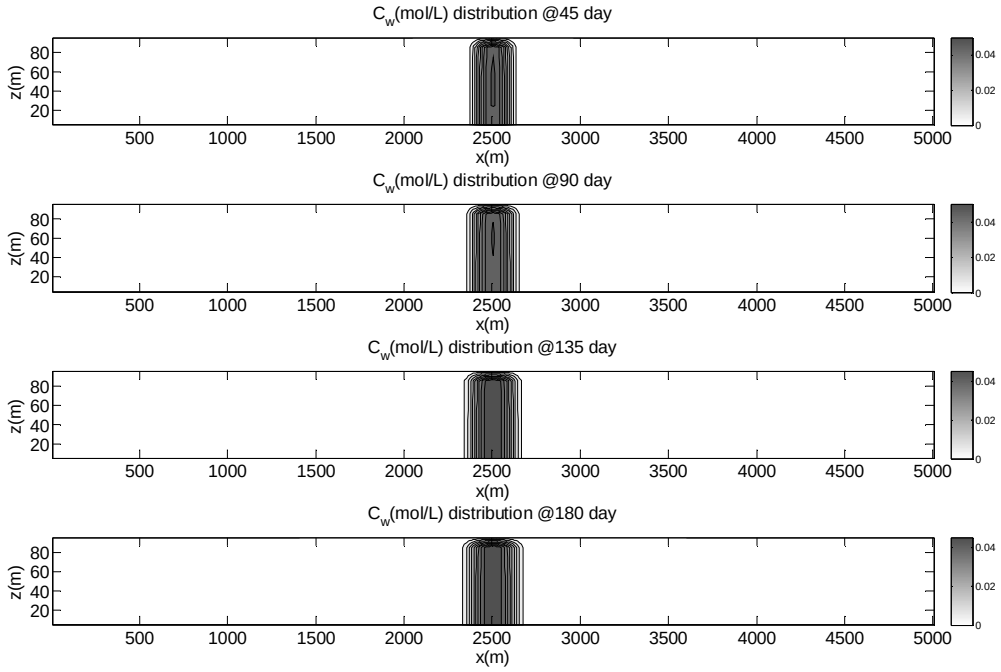

Figure 5.15 Spatial distribution of SO_2 aquatic concentration over time for Case 'D'

As is presented in Section 5.4.1, SO_2 equilibrium concentration and SO_2 concentration in the $scCO_2$ have similar profiles with those for SO_2 aquatic concentration; therefore, their profiles are not presented here.

Because the concentration of H^+ is highly dependent of SO_2 concentration in the water, the profiles of H^+ (shown in Figure 5.16) have similar profiles with those for SO_2 concentration in the water. Also, the changes in the porosity (shown in Figure 5.17) induced by the mineral dissolution and precipitation share similar profiles with those for H^+. Both H^+ and porosity have narrower profiles along the x direction if compared to those for Case 'F'.

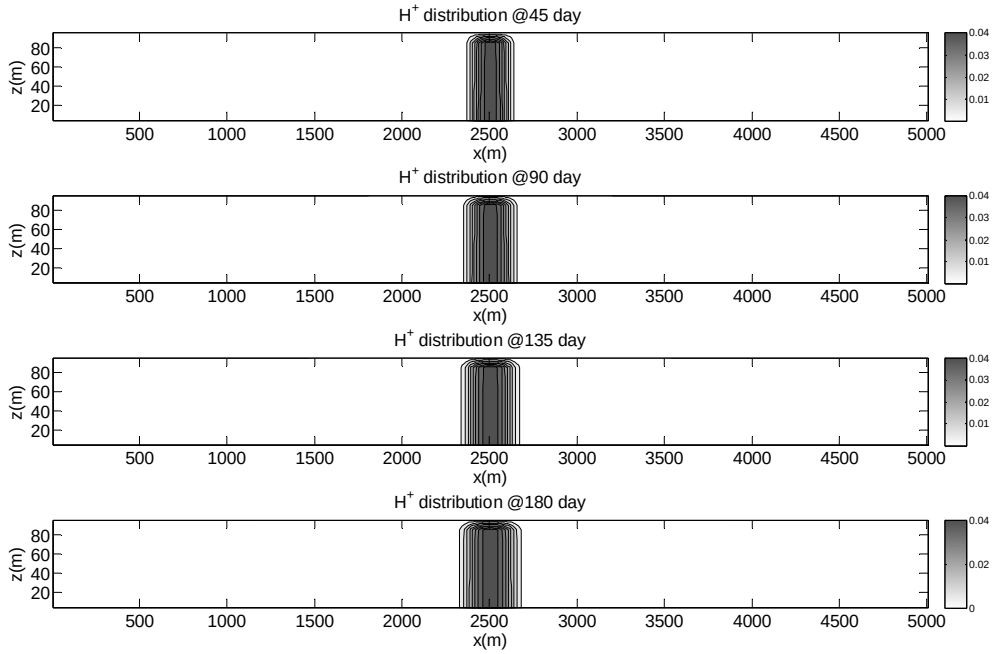

Figure 5.16 Spatial distribution of H^+ over time for Case 'D'

Since the region near the injecting node is very important to CO_2 injection and storage, the evolution of several important variables will be presented and compared among the three scenarios for nodes in the first row. As for SO_2 equilibrium concentration, SO_2 concentration in the $scCO_2$ and SO_2 aquatic concentration, only minor difference can be observed (shown in Figure 5.18) in the first few days for Node (251, 1) and Node (252,1) between Case 'F' and Case 'D'. Therefore, there is minor difference

for H^+, porosity and absolute permeability for the first few days between the two cases as well, as can be seen in the right half of Figure 5.19.

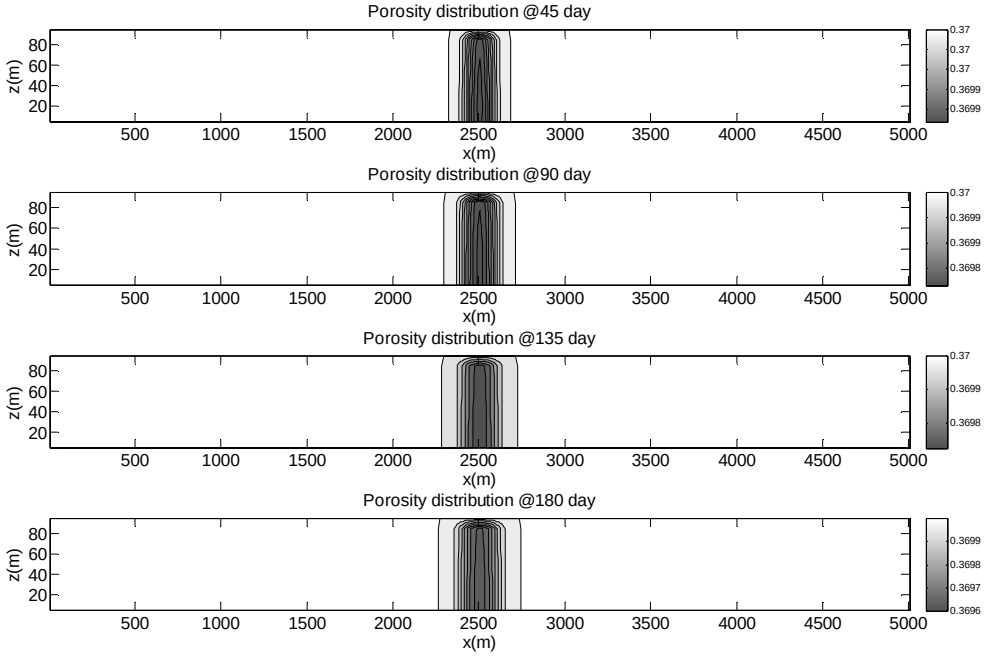

Figure 5.17 Spatial distribution of porosity over time for Case 'D'

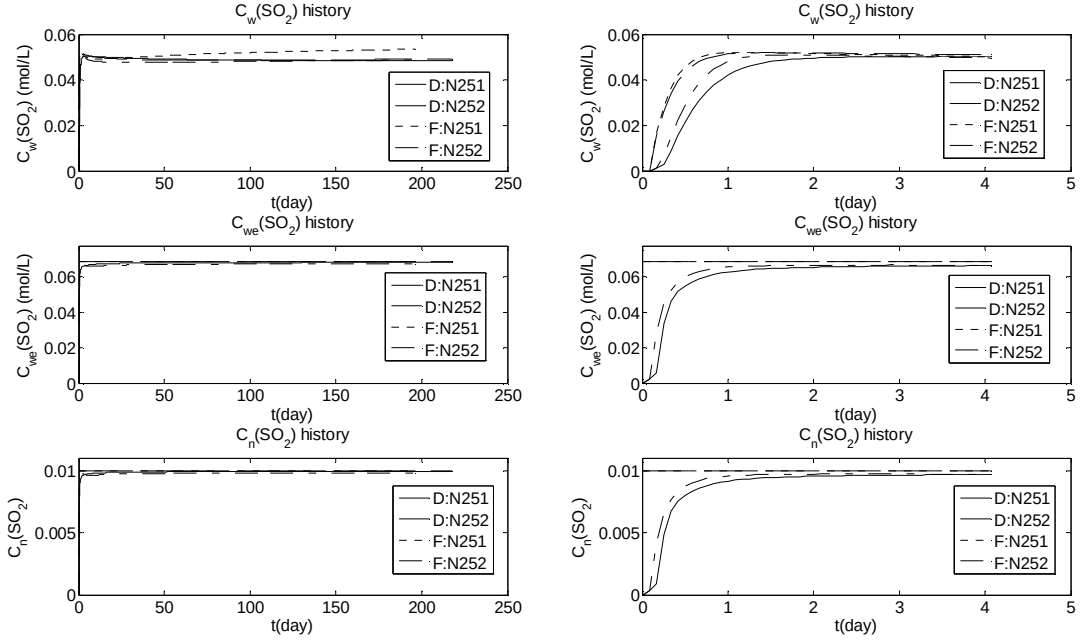

Figure 5.18 Comparison of the evolution for selected variables for nodes in the first row

As we can see from the top left graph in Figure 5.19, H^+ concentration is a little higher for Case 'FE' than Case 'E' because more SO_2 will be dissolved into the water for Case 'FE'. Since the kinetic reactions for both the dissolution of hematite and the precipitation of pyrite can be accelerated by the presence of H^+ (the more of H^+, the faster for the reactions), the magnitude for the changes in porosity and permeability for Case 'FE' would be a little larger than that for 'E', as can be observed in the middle left and lower left graphs in Figure 5.19. The porosity experiences a maximal decrease percentage of 0.103 and 0.133 for the cases 'F' and 'FE', respectively, while the maximal decrease percentage for the permeability is 0.427 and 0.554, in the injecting node at the end of one half year.

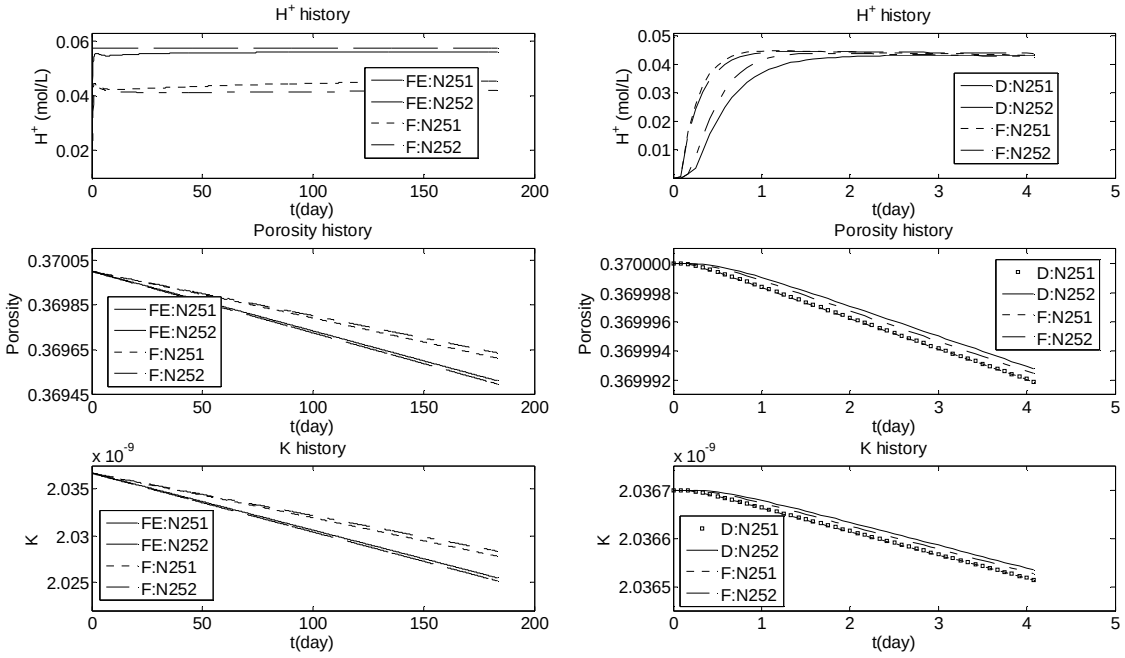

Figure 5.19 Comparison of the evolution for H^+, porosity and K for nodes in the first row

5.4.3 Implications

The results from the base case and the comparison with the other two scenarios have significant implications for CO_2 injection and storage in deep saline aquifers.

First of all, it is important to incorporate Forchheimer effect into the numerical simulation of multiphase flow to properly characterize the additional friction caused by the high flow velocity of CO_2. As is analyzed in Section 5.4.1 and 5.4.2, the inclusion of

Forchheimer effects into the multiphase flow models will change the flow pattern of CO_2 a lot near the wellbore area in terms of CO_2 spatial and temporal saturation profiles and pressure distribution. Neglecting the inertial effect would definitely introduce considerable errors to the simulation results.

Secondly, compounded by the buoyancy effects, the Forchheimer effect would lead to CO_2 migration preferentially along the horizontal directions over the vertical direction, indicating that more CO_2 will be stored in the lower half of the saline aquifer and less CO_2 will move upward to the lower boundary of the overlaying cap-rock. In other words, less pressure will be imposed on the cap-rock layer under Darcy-Forchheimer flow, which is a significant merit for safely storing CO_2 in saline aquifers. Traditionally, with the assumption of complete Darcy flow, the injected CO_2 will move upward favorably and quickly with the influence of the difference in density and viscosity between scCO_2 and the saline and accumulate below the lower boundary of the overlaying cap-rock and the pressure imposed on the cap-rock will increase with the accumulation of CO_2 (Hayek et al., 2009; Oldenburg et al., 2011), which will increase the possibility of fracturing the cap-rock and thus the leakage of CO_2 upward toward the ground and atmosphere. However, the introduction of Forchheimer effects, together with the buoyancy effects, will lead to more CO_2 accumulation in the lower half of the domain and less pressure imposed on the cap-rock. For example, Figure 5.20 shows the comparison of the temporal evolution for CO_2 saturation and potential for Node (251, 10), the node just below the cap-rock in the injecting column. From the top left graph, it is obvious that far less CO_2 would reach the upper boundary in Darcy-Forchheimer flow than Darcy flow. As a result, CO_2 potential for Darcy-Forchheimer flow would be lower than that for Darcy flow, with a difference of 2000 pa (0.02%) at the end of one half year.

Thirdly, the higher displacement efficiency by CO_2 is good news for CO_2 sequestration into deep saline aquifers. This means that for the same volume of porous media, more pore space can be occupied by CO_2 in Forchheimer flow than Darcy flow for the same injection rate and time. A comparison between Figure 5.2 and 5.13 would indicate that more CO_2 can be stored in Forchheimer regime than Darcy regime. When compared with Figure 5.13 where the saturation contour lines expand smoothly with time for Darcian flow, Figure 5.2 shows that higher CO_2 saturation would accumulate inside

the Forchheimer regime. In addition, as we can see from the comparison of Figure 5.2 and 5.4 that the region with high saturation matches well with the Forchheimer zone. A careful comparison of Figure 5.2 and 5.13 can show that the 0.48 saturation contour lines for Darcy flow lie inside the 0.48 saturation contour lines for Forchheimer flow at the same time. This means that more CO_2 can be stored in Forchheimer regime. This point can be verified by quantitative analysis as well. At Day 180, if we sum up all the CO_2 in all the nodes in the Forchheimer region (based on f_{nz}), the accumulated CO_2 in this area accounts for 91% of all the injected CO_2 up to Day 180 with 4.3% of the total CO_2 flowing away from the domain through the western and eastern boundaries. However, for the complete Darcy flow in Case 'D', the same region only stores 57% of all the injected CO_2 with the same percentage of CO_2 flowing out from the domain. This means that the displacement efficiency in Forchheimer flow is 59% higher than that for Darcy flow. This more thorough displacement of water by CO_2 in Forchheimer flow should be a significant merit if the cost associated with the screening and selection, injection well design and construction, and injection operation of a CO_2 sequestration site is considered, not to mention that the compounding of the Forchheimer effect and buoyancy effect will lead to less pressure imposing on the lower boundary of the cap-rock.

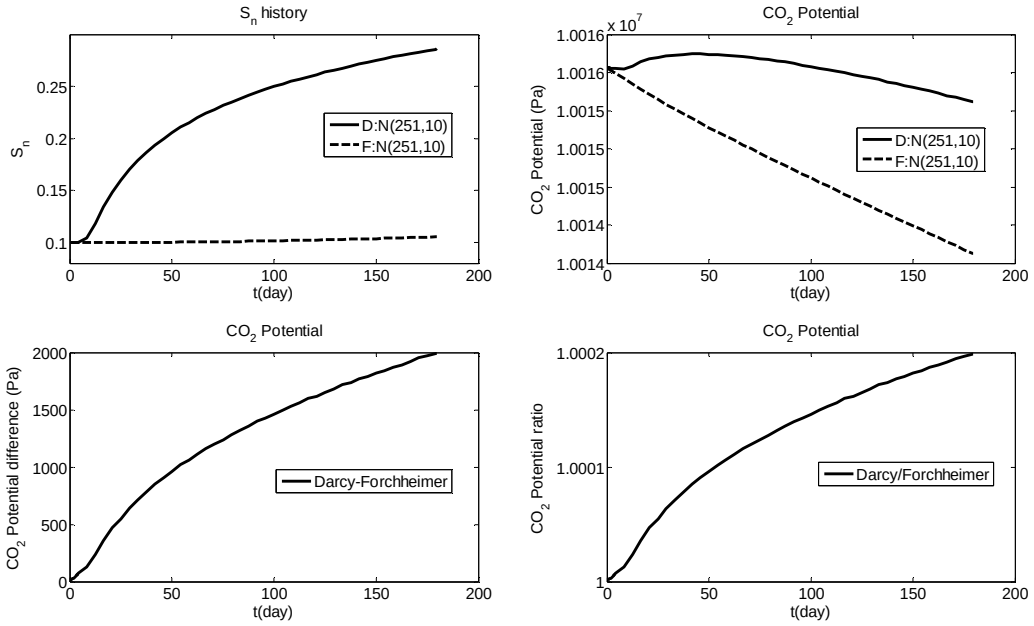

Figure 5.20 Comparison of the evolution of CO_2 saturation and potential for Node (251, 10)

Fourthly, we should also recognize that the higher injection pressure required in Forchheimer flow is problematic for CO_2 injection applications. Everything comes with a price. The price for higher displacement efficiency is a higher injection pressure. As is shown in Figure 5.21, the pressure required by Forchheimer flow in the injecting node is more than 0.04% higher (more than 4000 Pa) than that for Darcy flow at Day 180. Although the magnitude in the changes of porosity and permeability in the injecting node is a little larger in Case 'FE' than that for Case 'F', the CO_2 pressure in the node has no noticeable difference, as is seen in Figure 5.21. The higher pressure requirement would be more significant if one considers that the injection period would in general be more than 30 years. Higher pressure requirement would first entail more energy cost. What is more troublesome is that the pressure will continue to increase and might even exceed the litho-static stress, then there is an increasing risk for triggering fracturing or shear-slip at or near the injection point. Therefore, it is vital to monitor the hydro-mechanical behavior in the near-wellbore area while continuing the injection of CO_2. Furthermore, the tradeoff between the improved displacement efficiency and the increasing injection pressure should be well balanced in order to store as much CO_2 as possible while keeping the storage zone secure and safe. This point needs to be carefully analyzed for site specific cases especially for a more realistic injection domain and a larger time scales of injection period.

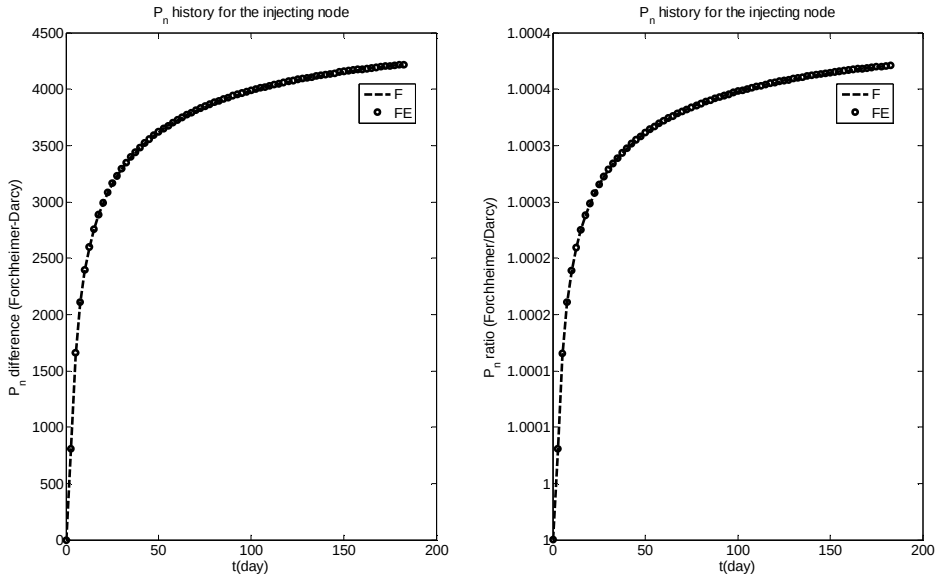

Figure 5.21 Comparison of the evolution of CO_2 pressure for Node (251, 1)

Fifth, since the Forchheimer effect has determinant impact on CO_2 migration and SO_2 transports together with $scCO_2$, the Forchheimer effect has important impact on the transport and fate of the co-injected SO_2 and thus on the profiles of the saline acidification and the induced changes in porosity and permeability changes. For example, in Case 'F', CO_2 moves in favor of the horizontal direction over the vertical direction while the movement of CO_2 is more evenly in Case 'D'. According, the transport of SO_2 is more along the x direction and less along the z direction, resulting in wider horizontal profiles of SO_2 aquatic concentration and the resultant H^+ concentration and porosity and permeability.

Last, but not least, the accumulated difference in the saline acidification and the induced porosity and permeability changes between kinetic and equilibrium dissolution of SO_2 is moderate. Although the SO_2 concentration increases fast for the first few days, it will never hit the SO_2 equilibrium concentration due to the buffering capacity of the mineral dissolution and precipitation. If more complex mineral composition is considered, the buffering capacity might be even stronger, leading to a larger difference between SO2 aquatic concentration and its solubility limit. Therefore, to simulate a field case, assuming equilibrium dissolution of SO_2 from $scCO_2$ to the saline would overestimate the brine acidity and its induced porosity and permeability changes and introduce even larger errors into the simulation results.

It is important to point out that the magnitude of the pressure difference between Darcy and Forchheimer flow in the injecting node is relatively small compared to the scale of CO_2 pressure (10 MPa) in this study. The first reason for the small pressure difference is that the CO_2 injecting rate is relatively small. The injecting rate specified in this study is chosen based on the emission rate of a standard size 1,000-MW coal-fired power and the disposal capacity of current pilot projects for CO_2 injection and storage. However, these are small by comparison with the size of projects required to store gigatonnes of CO_2 within a decade (Haszeldine, 2009). Full-scale projects are anticipated to be five-to-ten million tonnes or more per year per site. With that injection rate, the Forchheimer flow would be much stronger and the pressure difference between Darcy and Forchheimer flow would be significantly higher, which may intrigue more issues for CO_2 injection and storage.

The second reason for the small pressure difference is that the absolute permeability used in this chapter (selected based on the experimental results for water flooding experiments conducted by Sobieski and Trykozko (2012)) is relatively large compared to that for a candidate CO_2 storage site. That is also the reason for the almost no noticeable pressure difference between Case 'F' and Case 'FE', although the changes of porosity and permeability in Case 'FE' is almost one third larger than those for Case 'F', respectively.

5.5 Summary

The methods and the multiphase flow, contaminant transport and geochemical models developed in Chapter 3 and 4 are employed to analyze the Darcy-Forchheimer flow and the brine acidification and the induced changes in porosity and permeability due to SO_2 co-injection with CO_2. We have performed three simulations of acid-gas injection into a 2-D formation with typical hydro-geologic properties and simplified mineral compositions. Major findings and conclusions are as follows:

vii. It is important to incorporate Forchheimer effect into the numerical simulation of multiphase flow to properly characterize the additional friction caused by the high flow velocity of CO_2 because the inclusion of Forchheimer effects into the multiphase flow models will significantly change the flow pattern of CO_2.

viii. The high vertical velocity resulting from the buoyancy effects would lead to higher Forchheimer number and thus inhibit CO_2 from spreading vertically due to the stronger resistance in the vertical direction. Thus, more CO_2 would be accumulated in the lower half of the domain and lower pressure would be imposed on the lower boundary of the cap-rock.

ix. Compounded by the buoyancy effect, the Forchheimer effect would result in higher displacement efficiency in the Forchheimer regime. For example, the displacement efficiency in Forchheimer flow is 59% higher than that for Darcy flow at the end of one half year. The higher displacement efficiency increases the storage capacity for the same injection rate and volume of a site;

x. The higher injection pressure required in Forchheimer flow is problematic for CO_2 injection applications. The higher pressure required would entail more

energy and other costs. More importantly, the higher injection pressure (may increase as the injection continues) would expose the whole domain to a higher pressure by a difference of 10^3 Pa at least. Higher pressure exposure might increase the risk of fracturing the domain and CO_2 leakage into the atmosphere, especially for a field case where the absolute permeability is relatively small (with a magnitude of darcy even millidarcy).

xi. The tradeoff between the improved displacement efficiency and the increasing injection pressure should be well balanced in order to store as much CO_2 as possible while keeping the storage zone secure and safe. When the increase of injecting pressure may not cause major issues, larger injection rate of CO_2 can be injected to maximize the storage capacity; however, the increase in displacement efficiency should yield to the safety and security of CO_2 injection and operation when the magnitude in the increase of injecting pressure is relatively large and may significantly increase the possibility of fracturing the formations and leakage of CO_2 toward the ground and atmosphere.

xii. It is important to include the kinetic dissolution of SO_2 from the $scCO_2$ to the water phase into the simulation models because the SO_2 concentration in the aqueous phase would not be close to its solubility limit for the injecting node even at the end of one half year. The accumulated effect of the difference between the actual SO_2 concentration in the aqueous phase and its solubility limit would be considerable and can not be neglected, especially for complex mineral composition which has higher buffering capacity.

xiii. The co-injection of SO_2 with CO_2 results in a substantially acid zone near the injecting well. For the base case by the end of one half year, the H^+ concentration in the injecting node is 0.045mol/L and the region with H^+ concentration larger than 0.01mol/L expands to a distance 450 meters from the injecting node horizontally (to the top boundary vertically). The reasons for the relatively fast expansion of the acid zone can be attributed to the fact that the simplified initial mineral composition does not have enough pH buffering capacity as other complex mineral composition does and to the fact that the advection and diffusion effects are relatively strong in this study.

xiv. The porosity experiences a maximal decrease percentage of 0.103 and 0.133 for the cases ‘F’ and ‘FE’, respectively, while the maximal decrease percentage for the permeability is 0.427 and 0.554 for the cases ‘F’ and ‘FE’, respectively, in the injecting node at the end of one half year.

xv. Since the Forchheimer effect has determinant impact on CO_2 migration and SO_2 transports together with $scCO_2$, the Forchheimer effect has important impact on the transport and fate of the co-injected SO_2 and thus on the profiles of the saline acidification and the induced changes in porosity and permeability changes

xvi. The initial mineral composition is simplified and the important pH buffering capacity of complex mineral composition is not included in this study. Therefore, the results for a single scenario in this study can only be interpreted as the ‘worst-case scenario’.

These conclusions are only quantitatively dependent upon the choice of the capillary pressure curves and the Forchheimer coefficients that were determined here from experimental data provided in the literature. This study provides a useful tool for future analysis and comprehension of multiphase Darcy-Forchheimer flow and brine acidification of SO_2 co-injection with CO_2 into deep saline aquifers. However, the conclusions for the application problem are preliminary, as they are limited by model simplifications due to insufficient thermodynamic data, kinetic and physical data, and limited computational power. For example, since there are no CO_2 flooding experimental data found in the literature, the data for water flooding experiments are used to determine the critical Forchheimer number for CO_2, which may lead to some uncertainty. Therefore, further experimental studies and numerical investigations will be required, especially in terms of CO_2 flooding experiment for a field scale and the kinetic reaction of disproportionation of SO_2.

Chapter 6 Conclusions

The global climate change as a result of the emission of greenhouse gases (GHG) becomes more and more acknowledged within the scientific community. The most important GHG is carbon dioxide (CO_2), because it is emitted in very large quantities and may persist in the atmosphere for thousands of years (Archer, 2005). In the broad portfolio of strategies to reduce carbon emissions using methods such as carbon capture and sequestration, enhanced efficiency of power generation and use, use of low carbon fuels and renewable energy sources, storage of anthropogenic CO_2 within geologic reservoirs is one of the favorable methods of carbon sequestration (Bachu, 2002). Geologic sequestration represents an immediately available option for mitigating the global environmental impact of CO_2 by removing large amounts of the gas from the atmosphere. However, before the application of full-scale commercial projects become practical for geological carbon storage, the feasibility of applying this method to large quantities of CO_2 has to be investigated with all available scientific means.

One important aspect of CO_2 sequestration is the carbon dioxide flow and transport within the porous media used as a storage formation. Questions regarding the evolution of the CO_2 plume in the subsurface, its long-term behavior, geochemical reactions and the effects of its co-injected impurities have to be answered. Because of the complexity and the large time scale, the most efficient way of addressing these issues is the mathematical description of the processes that occur in the subsurface and the numerical solution of the resulting complex equations.

Therefore, numerical models for multiphase flow, contaminant transport and related geochemistry have been developed and used to investigate the transition behavior between Darcy flow and Forchheimer flow for multiphase cases, and to investigate the brine acidification and the induced porosity and permeability changes due to sulfur dioxide (SO_2) co-injection with supercritical CO_2 ($scCO_2$). In the following sections, general conclusions and directions for future study covered in this thesis are presented.

6.1 Summary and Conclusions

As far as the fluid flow is concerned, the numerical multiphase model developed in this thesis has been validated and shown good agreement with a semi-analytical solution inspired from the Buckley-Leverett model with inertial effects. Moreover, in order to analyze the transition behavior between Darcy and Forchheimer flow, the critical Forchheimer numbers for water and CO_2 have been determined with the method proposed in Section 3.2. Since both β_α and f_α are functions of saturation of α phase, there is a critical Forchheimer number for the transition for a specific saturation for each phase in multiphase flow system. From the analysis in terms of Darcy-Forchheimer flow during CO_2 injection into deep saline aquifers in Chapter 3 and 5, the following conclusions can be obtained.

i. It is important to incorporate Forchheimer effect into the numerical simulation of multiphase flow to properly characterize the additional friction caused by the high flow velocity of CO_2. As is analyzed in Section 5.4.1 and 5.4.2 (or Section 3.51 and 3.52), the inclusion of Forchheimer effects into the multiphase flow models will change the flow pattern of CO_2 a lot near the wellbore area in terms of CO_2 spatial and temporal saturation profiles and pressure distribution. Neglecting the inertial effect would definitely introduce considerable errors to the simulation results;

ii. The proper way to determine the critical Forchheimer number for the transition between Darcy flow and Forchheimer flow can crucially affect the extent to which Forchheimer effect can influence the transport of CO_2 in deep saline aquifers. It is for sure that Forchheimer effect can never impact the complete domain in a large CO_2 injection field (e.g., kilometers in width and length), but it is essential to find out the region for Forchheimer flow near the injection point by applying the critical values for the transition since unacceptable errors would be induced if we neglect the nonlinear terms near the injection region;

iii. Compounded by the buoyancy effects, the Forchheimer effect would lead to CO_2 migration preferentially along the horizontal directions over the vertical direction, more CO_2 accumulating in the lower half of the domain and lower pressure imposed on the cap-rock. For example, Figure 5.20 shows that, for

Node (251, 10), the node just below the cap-rock in the injecting column, far less CO_2 would reach the upper boundary in Darcy-Forchheimer flow than Darcy flow and CO_2 potential for Darcy-Forchheimer flow would be lower than that for Darcy flow, with a difference of 2000 pa (0.02%) at the end of one half year;

iv. The higher displacement efficiency by CO_2 is a significant merit for CO_2 sequestration into deep saline aquifers. This means that for the same volume of porous media, more pore space can be occupied by CO_2 in Forchheimer flow than Darcy flow for the same injection rate and time. For example, for the application in Chapter 5, at Day 180, the accumulated CO_2 in all the nodes in the Forchheimer region (based on f_{nz}) accounts for 91% of all the injected CO_2 up to Day 180 with 4.3% of the total CO_2 flowing away from the domain through the western and eastern boundaries. However, for the complete Darcy flow, the same region only stores 57% of all the injected CO_2 with the same percentage of CO_2 flowing out from the domain. The comparison suggests that the displacement efficiency in Forchheimer flow is 59% higher than that for Darcy flow at the end of one half year;

v. The higher injection pressure required in Forchheimer flow may be problematic for CO_2 injection applications. As is shown in Figure 5.21, the pressure required by Forchheimer flow in the injecting node is more than 0.04% higher (more than 4000 Pa) than that for Darcy flow at Day 180. The higher pressure requirement would be more significant if one considers an injection period generally more than 30 years, a higher injection rate, and lower absolute permeabilities in full-scale commercial projects;

vi. The tradeoff between the improved displacement efficiency and the increasing injection pressure should be well balanced in order to store as much CO_2 as possible while keeping the storage zone secure and safe. When the increase of injecting pressure may not cause major issues, larger injection rate of CO_2 can be injected to maximize the storage capacity and minimize the pressure imposed on the cap-rock; however, the increase in displacement efficiency should yield to the safety and security of CO_2 injection and operation when the magnitude in

the increase of injecting pressure is relatively large and may significantly increase the possibility of fracturing the formations and leakage of CO_2 toward the ground and atmosphere.

These conclusions are only quantitatively dependent upon the choice of the capillary pressure curves and the Forchheimer coefficients which were determined here from experimental data provided in the literature. This thesis provides a useful tool for future analysis and comprehension of multiphase Darcy-Forchheimer flow and Forchheimer effects of CO_2 injection into deep saline aquifers. However, the most uncertainty during the analysis is associated with the strength of the Forchheimer effect, which depends on CO_2 injection rate, the magnitude of absolute permeability, the magnitude of the critical Forchheimer number, the Forchheimer coefficient, and the properties of the injected CO_2. In addition to the direct impact on the Forchheimer number, the properties of CO_2 such as density and viscosity can play an important role by changing the strength of the buoyancy effects which would change the flow pattern of CO_2 combining with the Forchheimer effects. Therefore, for the methods and models proposed in this thesis to be applicable to analyze the Darcy-Forchheimer flow in field cases, more experimental and field studies will be needed before any analysis. These studies should include CO_2 and water flooding experiments, reservoir characterization and so on.

With regard to the effects of SO_2 co-injection with CO_2 into deep saline aquifers, the contaminant transport and simplified geochemical models have been developed and employed to investigate the brine acidification and induced porosity and permeability changes due to kinetic or equilibrium dissolution of SO_2 from $scCO_2$ to the aqueous phase. Based on the simulation results in Chapter 4 and 5, the major findings and conclusions are listed as follows.

i. It is important to include the kinetic dissolution of SO_2 from the $scCO_2$ to the water phase into the simulation models because the SO_2 concentration in the aqueous phase would not be close to its solubility limit for the injecting node even by the end of the simulation period. The accumulated effect of the difference between the actual aqueous SO_2 concentration and its solubility limit

would be considerable and can not be neglected, especially for complex mineral composition which has higher buffering capacity;

ii. It is not necessary to include the kinetic dissolution of CO_2 from the $scCO_2$ to the water phase into the simulation models since the CO_2 concentration would reach its solubility limit in a time scale of several days. Therefore, for simulations with a time scale larger than weeks, it is valid to assume equilibrium dissolution of CO_2 from the $scCO_2$ to the aqueous phase;

iii. The coupling between the fluid flow and the changes in porosity and permeability is critical to the CO_2 injection into deep saline aquifers in that the coupling would require significantly higher injection pressure and higher pressure all over the domain, as is shown in Chapter 4. The pressure difference between the coupling and non-coupling cases is in an order of 10^4 Pa and the pressure for coupling cases would experience an increase of more than 0.1% over the non-coupling cases for most of the simulation time. At the end of one year, the case 'Equi-cou' has a pressure increase of 78119 Pa (0.55%) over the non-coupling cases while the increase for the case 'Ki-cou' is 58669 Pa (0.41%). The case with the kinetic mass transfer of SO_2 can save energy and money for the pressure difference of 19450 Pa over the case with equilibrium assumption at the end of one year;

iv. The co-injection of SO_2 with CO_2 results in a substantially acid zone near the injecting well. For the base case in Chapter 5 by the end of one half year, the H^+ concentration in the injecting node is 0.045mol/L and the region with H^+ concentration larger than 0.01mol/L expands to a distance 450 meters from the injecting node horizontally (to the top boundary vertically). The reasons for the relatively fast expansion of the acid zone can be attributed to the fact that the simplified initial mineral composition does not have enough pH buffering capacity as other complex mineral composition does and to the fact that the advection and diffusion effects are relatively strong in this study;

v. Since the Forchheimer effect has determinant impact on CO_2 migration and SO_2 transports together with $scCO_2$, the Forchheimer effect has important impact on the transport and fate of the co-injected SO_2 and thus on the profiles of the

saline acidification and the induced changes in porosity and permeability changes. For example, for the base case in Chapter 5 , CO_2 moves in favor of the horizontal direction over the vertical direction while the movement of CO_2 is more evenly in Case 'D'. Accordingly, the transport of SO_2 is more along the x direction and less along the z direction, resulting in wider horizontal profiles of SO_2 aquatic concentration and the resultant H^+ concentration and porosity and permeability;

vi. The accumulated difference in the saline acidification and the induced porosity and permeability changes between kinetic and equilibrium dissolution of SO_2 is moderate. Although the SO_2 concentration increases fast for the first few days, it will never hit the SO_2 equilibrium concentration due to the buffering capacity of the mineral dissolution and precipitation. If more complex mineral composition is considered, the buffering capacity might be even stronger, leading to a larger difference between SO_2 aquatic concentration and its solubility limit. Therefore, to simulate a field case, assuming equilibrium dissolution of SO_2 from $scCO_2$ to the saline would overestimate the brine acidity and its induced porosity and permeability changes and introduce even larger errors into the simulation results;

vii. The initial mineral composition is simplified and the important pH buffering capacity of complex mineral composition is not included in this study. Therefore, the results in terms of brine acidification and induced porosity and permeability changes for a single scenario in this study can only be interpreted as the 'worst-case' scenario;

viii. From the sensitivity analysis in Chapter 4, it can be found that the hematite and SO_2 dissolution rates have significant impact on CO_2 pressure, hematite and pyrite abundance, porosity and permeability. As for SO_2 and H^+ aqueous concentration, K_SO_2 does have significant positive impact while K_he has a less significant effect.

The conclusions provide insightful recommendations for CO_2 injection and storage and numerical investigation on the impacts of the co-injected SO_2. However, the

applicability of these recommendations is limited by model simplifications due to insufficient thermodynamic data, kinetic and physical data, and limited computational power. The first uncertainty is related to the simplification of the initial mineral composition. Then the kinetic reaction of disproportionation of SO_2 can lead to considerable uncertainty, as is discussed in Section 4.5. Therefore, further experimental studies and numerical investigations will be required for successful implementation of these realistic simplified models to field cases.

To summarize, the conclusions and findings of this thesis have practical use for scientists and engineers concerned with the description of flow behavior, and transport and fate of SO_2 during SO_2 co-injection with CO_2 in deep saline aquifers. In spite of the simplifying assumptions, the analysis provides estimates of relevant processes and their effects regardless of the site-specific reservoirs. The results provide a better understanding of the flow behavior and the brine acidification in porous media and can be used to perform a more detailed further analysis such as three-dimensional field-scale modeling as well. However, successful implementation of these simplified models requires further test through a series of both field and laboratory experiments. The degree of matching will either confirm current simulations or indicate how the modeling should be adjusted with an ultimate goal to verify the key model assumptions by field and laboratory observations.

6.2 Future work

Numerical fluid flow and reactive transport modeling is a powerful tool that can be used to investigate the behavior of long term fluid flow, and reaction and solute transport which can not be readily studied at laboratory or field scale in short period of time. However, it is always critical to note that a numerical model is only a simplified representation of reality, which produces output that is only accurate to the same degree at most as the input data, and thus reflects only our understanding of a given system. Consequently, the greatest challenge in applying numeric models is, and always will be, to evaluate how well the conceptual model of a system is defined, based on real field observations, and how well that conceptual model can be manifested in the model. Hence, with regard to CO_2 geological storage, it is imperative to model any conceptualized

system or process based on appropriate CO_2 solubility model, realistic yet simple geometrical configuration, flow conditions, and thermodynamic and kinetic data set with improved data quality. For this, future work needs to include experimental and field observation pertinent to the intended purpose.

Based on the findings of the study presented in this thesis, the following research topics can be recommended as further research areas:

i. Experimental investigation of CO_2 and water flooding in candidate formations for CO_2 storage under realistic conditions to better determine the critical Forchheimer number;
ii. Numerical investigation on the geo-mechanical changes induced by the injection of CO_2, especially for Darcy-Forchheimer flow where the required injection pressure is higher than that for Darcy flow and thus the possibility for fracturing the porous media might increase significantly;
iii. Experimental studies on the kinetic reaction rate for the homogeneous disproportionation of SO_2;
iv. Numerical and experimental research on the potential effects of nitrogen oxides (NO_x) co-injection with scCO_2;
v. Investigation on the combing effects of impurities including NO_x and sulfur oxides (SO_x), hydrogen sulfide (H_2S), and so on. Whether the combing effect is of synergism or antagonism needs further study;
vi. Comprehensive cost-benefits analysis on SO_x (or NO_x, H_2S and other impurities) disposal with CO_2 in deep saline aquifers is required before co-injection of these impurities into field reservoirs.

REFERENCES

Abou-Kassem, J.H., Farouq Ali, S.M., & Islam, M.R. (2006). Petroleum Reservoir Simulation: A Basic Approach. Houston: Gulf Publishing Company.

Ahmadi, A., Arani, A. A. A., & Lasseux, D. (2010). Numerical simulation of two-phase inertial flow in heterogeneous porous media. Transport in porous media, 84(1), 177-200.

Ahmed, N., & Sunada, D. K. (1969). Nonlinear Flow in Porous Media. J. Hydraulics Div. ASCE, 95(HY6), 1847.

Andrade, J. A., Jr., Costa, U. M. S., Almeida, M. P., Makse, H. A. & Stanley, H. E. (1999). Inertial effects on fluid flow through disordered porous media. Phys. Rev. Let., 82(26), 5249–5252.

Archer, D. (2005). Fate of fossil fuel CO_2 in geologic time. Journal of Geophysical Research: Oceans (1978–2012), 110(C9).

Bachu, S. (2002). Sequestration of CO_2 in Geological Media in Response to Climate Change: Road Map for Site Selection using the Transform of the Geological Space into CO_2 Phase Space. Energy Convers. Mgmt., 43, 87-102.

Bachu, S. (2008). CO_2 storage in geological media: role, means, status and barriers to deployment. Prog. Energ. Combust., 34 (2), 254–273.

Bachu, S., & Bennion, D.B. (2009 a). Chromatographic partitioning of impurities contained in a CO_2 stream injected into a deep saline aquifer: Part 1. Effects of gas composition and in-situ conditions. International Journal of Greenhouse Gas Control, 3 (4), 464–473.

Bachu, S., & Gunter, W.D. (2004). Overview of acid-gas injection operations in western Canada. In: Proceedings of the 7th International Conference on Greenhouse Gas Control Technologies. Volume 1: Peer-Reviewed Papers and Plenary Presentations, Vancouver, BC, September 5–9, 2004.

Bachu, S., Gunter, W.D., & Perkins, E.H. (1994). Aquifer disposal of CO_2:hydrodynamic and mineral trapping. Energy Conversion and Management, 35(4), 269–279.

Bachu, S., Pooladi-Darvish, M., & Hong, H. (2009 b). Chromatographic partitioning of impurities (H_2S) contained in a CO_2 stream injected into a deep saline aquifer: Part

2. Effects of flow conditions. International Journal of Greenhouse Gas Control, 3 (4), 458–463.

Bacon, D.H., Sass, B.M., Bhargava, M., Sminchak, J., & Gupta, N. (2009). Reactive transport modeling of CO_2 and SO_2 injection into deep saline formations and their effect on the hydraulic properties of host rocks. Energy Procedia, 1 (1), 3283–3290.

Baes, C.F., Beall, S.E., Lee, D.W., & Marland, G. (1980): The collection, disposal and storage of carbon dioxide. In: Interaction of Energy and Climate, W. Bach, J. Pankrath and J. William (eds.), 495–519, D. Reidel Publishing Co.

Bahr, J.M., & Rubin, J. (1987). Direct comparison of kinetic and local equilibrium formulations for solute transport affected by surface reactions. Water Resources Research, 23, 438–452.

Baines, S.J., & Worden, R.H. (2004). The long-term fate of CO_2 in the subsurface: natural analogues for CO_2 storage. In: Baines, S.J., Worden, R.H. (Eds.), Geological Storage of Carbon Dioxide, vol. 233. Geological Society, London, Special Publications, 59–85.

Barree, R. D., & Conway, M. W. (2004, September). Beyond beta factors: a complete model for Darcy, Forchheimer, and trans-Forchheimer flow in porous media. In SPE Annual Technical Conference and Exhibition.

Barree, R. D., & Conway, M. W. (2005). Reply to discussion of 'Beyond beta factors: a complete model for Darcy, Forchheimer, and Trans-Forchheimer flow in porous media'. J. Pet. Tech, 57(8), 73-74.

Barree, R., & Conway, M. (2007, November). Multiphase non-Darcy flow in proppant packs. In SPE Annual Technical Conference and Exhibition.

Basak, P. (1977). Non-Darcy Flow and Its Implications to Seepage Problems, Journal of the Irrigation and Drainage Division, American Society of Civil Engineers, 103, 459.

Battistelli, A., Calore, C., & Pruess, K. (1997). The simulator TOUGH2/EWASG for modeling geothermal reservoirs with brines and non-condensible gas. Geothermics, 26(4),437–464

Bear, J. (1972).Dynamics of Fluids in Porous Media. Elsevier, Amsterdam.

Bear, J. (1988). Dynamics of fluids in porous media. Dover publications.

Belhaj, H.A., Agha, K.R., Nouri, A.M., Butt, S.D., & Islam, M.R. (2003). Numerical and Experimental Modeling of Non-Darcy Flow in Porous Media. Paper SPE 81097 prepared for presentation at the SPE Latin America and Caribbean Petroleum Engineering Conference held in Port-of-Spain, Trinidad, West Indies, 27-30 April.

Benezeth, P., Palmer, D. A., Anovitz, L. M., & Horita, J. (2007). Dawsonite synthesis and reevaluation of its thermodynamic properties from solubility measurements: implications for mineral trapping of CO_2. Geochimica et Cosmochimica Acta, 71, 4438–4455.

Bennethum, L. S., & Giorgi, T. (1997). Generalized Forchheimer equation for two-phase flow based on hybrid mixture theory. Transport in Porous Media, 26(3), 261-275.

Benson, S.M., & Cole, D.R. (2008). CO_2 sequestration in deep sedimentary formations. Elements, 4 (5), 325–331.

Bethke, C. M. (1996), Geochemical reaction modeling. University Press, New York.

Bird, R.B., Stewart W.E., & Lightfoot, E.N. (1960), Transport Phenomena.Wiley, New York.

Blatt, H. (1982). Sedimentary Petrology. W.H. Freeman and Company, San Francisco.

Blick, E. F., & Civan, F. (1988), Porous media momentum equation for highly accelerated flow,SPE Reserv. Engng.1048–1052.

Brewer, P.G., Friederich, G.E., Peltzer, E.T., & Orr, F.M. Jr. (May 7, 1999). Direct Experiments on the Ocean Disposal of Fossil Fuel CO_2.Science, 284, 943-945.

Bruant, R.G., Guswa, A.J., Celia, M.A., & Peters, C.A. (2002). Safe storage of CO2 in deep saline aquifers. Environ. Sci. Technol. 26 (11), 240a–245a.

Buckley, S.E., & Leverett, M.C. (1942). Mechanism of fluid displacement in sands. Trans. AIME., 146, 107-116.

Carey, J.W., Wigand, M., Chipera, S.J., WoldeGabriel, G., Pawar, R., Lichtner, P.C.,Wehner, S.C., Raines, M.A., & Guthrie, G.D. (2007). Analysis and performance of oil well cement with 30 years of CO_2 exposure from the SACROC Unit, West Texas,USA. Int. J. Greenhouse Gas Control, 1 (1). 75–85.

Chilton, T. H., & Colburn, A. P. (1931). Pressure drop in packed tubes. Ind. Eng. Chem., 23(8), 913–919.

Civan, F., & Evans, R. D. (1993). Relative permeability and capillary pressure data from non-Darcy flow of gas/brine systems in laboratory cores. InSPE Gas Technology Symposium.

Clauser, C. (Ed.) (2003). Numerical Simulations of Reactive Flow in Hot Aquifers: SHEMAT and Processing SHEMAT. Springer, Berlin, Germany.

Coles, M. E., & Hartman, K. J. (1998, March). Non-Darcy measurements in dry core and the effect of immobile liquid. In SPE Gas Technology Symposium.

Cooke, C.E. Jr. (1973). Conductivity of Fracture Proppants in Multiple Layers. Journal of Petroleum Technology, 1101-1107.

Cooper, J. W., Wang, X., & Mohanty, K. K. (1999). Non-Darcy-flow studies in anisotropic porous media. SPE Journal, 4(4), 334-341.

Cornell, D., & Katz, D.L. (1953). Flow of gases through consolidated porous media. Ind. Eng. Chem., 45, 2145–2152.

de Visser, E., Hendriks, C., Barrio, M., Młlnvik, M.J., de Koeijer, G., Liljemark, S., & Le Gallo, Y. (2008). Dynamis CO_2 quality recommendations. International Journal of Greenhouse Gas Control, 2 (4), 478–484.

de Visser, E., Hendriks, C., de Koeijer, G., Liljemark, S., Barrio, M., Austegard, A., & Brown, A. (2009). CO_2 quality recommendations. Dynamis-Hypogen project: Deliverable D 3.1.3

Dooley, J. J. (2006). Carbon Dioxide Capture Geologic Storage: A Core Element of a Global Energy Technology Strategy to Address Climate Change. Battelle, Joint Global Change Research Institute.

Dybbs, A., & Edwards, R. V. (1984). A new look at porous media fluid mechanics—Darcy to turbulent. In Fundamentals of transport phenomena in porous media, 199-256. Springer Netherlands.

Du Plessis, J. P., & Masliyah, J. H. (1988), Mathematical modeling of flow through consol-idated isotropic porous media, Transport Porous Media, 3, 145–161.

Duan, Z., & Sun, R. (2003). An improved model calculating CO_2 solubility in pure water and aqueous NaCl solutions from 273 to 533 K and from 0 to 2000 bar.Chemical Geology, 193, 257-271.

Duguid, A., Radonjic, M., & Scherer, G.W. (2007).The effect of carbonated brine on well cement used in geologic formations, paper TH4-10.2. ISBN 978-0-660-19695-4 In: Beaudoin, J.J., Makar, J.M., Raki, L. (Eds.), Proc. 12th ICCC, National Research Council of Canada, Montreal, Canada.

Ellis, B.R., Crandell, L.E., & Peters, C.A. (2010). Limitations for brine acidification due to SO_2 co-injection in geologic carbon sequestration. International Journal of Greenhouse Gas Control 4 (3), 575–582.

Ergun, S. (1952). Fluid Flow through Packed Columns. Chem. Eng. Prog., 48, 89-94.

Ergun, S., Orning, A.A. 1949. Fluid Flow through Randomly Packed Column and Fluidized Beds. Industrial and Engineering Chemistry, 41, (6), 1179-1184.

Evans, E. V., & Evans, R. D. (1988). Influence of an immobile or mobile saturation on non-Darcy compressible flow of real gases in propped fractures. J. Petrol. Technol., 40(10), 1343-1351.

Evans, R. D., Hudson, C. S., & Greenlee, J. E. (1987).The effect of an immobile liquid saturation on the non-Darcy flow coefficient in porous media. J. SPE Prod. Eng Trans. AIME, 283, 331-338.

Ewing, R. E., Lazarov, R. D., Lyons, S. L., Papavassiliou, D. V., Pasciak, J., & Qin, G. (1999). Numerical well model for non-Darcy flow through isotropic porous media. Computational Geosciences, 3(3), 185-204.

Fan, Y. (2010). Chemical reaction modeling in a subsurface flow simulator with application to in-situ upgrading and CO_2 mineralization. Doctoral dissertation, Stanford University.

Fancher, G. H., & Lewis, J. A. (1933). Flow of simple fluids through porous materials, Ind. Engng. Chem., 25(10), 1139–1147.

Faruk Civan, & Evans, R. D. (1993). Relative Permeability and Capillary Pressure Data From Non-Darcy Flow of Gas/Brine System in Laboratory Cores. SPE Gas Technology Symposium, 28-30 June 1993, Calgary, Alberta, Canada. 978-1-55563-485-8.

Firoozabadi, A., & Katz, D. L. (1979). An analysis of high-velocity gas flow through porous media. J. Petrol. Technol., 211–216.

Forchheimer, P. (1901).Wasserbewegung durch boden. Zeit. Ver. Deutsch. Ing., 45, 1781-1788.

Gaus, I., Audigane, P., Andre, L., Lions, J., Jacquemet, N., Durst, P., Czernichowski-Lauriol, I., & Azaroual, M. (2008). Geochemical and solute transport modelling for CO2 storage, what to expect from it? International Journal of Greenhouse Gas Control, 2, 605–625.

Gaus, I., Azaroual, M., & Czernichowski-Lauriol, I. (2003) Reactive transport modelling of dissolved CO_2 in the cap rock base during CO_2 sequestration (Sleipner site, North Sea). Second Annual Conference on Carbon Sequestration, may 5-8th, http://www.iku.sintef.no/projects/IK23430000/Publications/Gaus etal CarbonSeqIIConf.pdf.

Gaus, I., Azaroual, M., & Czernichowski-Lauriol, I. (2005). Reactive transport modelling of the impact of CO_2 injection on the clayey cap rock at Sleipner (North Sea). Chemical Geology, 217 (3–4), 319–337.

Geerstma, J. (1974). Estimating the Coefficient of Inertial Resistance in Fluid Flow through Porous Media. Paper SPE 4706 available from SPE, Richardson, Texas.

Gherardi, F., Xu, T., & Pruess, K. (2007). Numerical modeling of self-limiting and self-enhancing caprock alteration induced by CO_2 storage in a depleted gas reservoir. Chemical Geology, 244, 103–129.

Giammar, D.E., Bruant, R.G., & Peters, C.A. (2005). Fosterite dissolution and magnesite precipitation at conditions relevant for deep saline aquifer storage and sequestration of carbon dioxide. Chemical Geology, 217 (3–4), 257–276.

Graves, R. M. (1994, September). New correlations to predict non-Darcy flow coefficients at immobile and mobile water saturation. In SPE Annual Technical Conference and Exhibition.

Green, L. Jr., & Duwez, P. (1951). Fluid flow through porous metals. J. Appl. Mech., 39-45.

Grigg, R., & Hwang, M. (1998, March). High velocity gas flow effects in porous gas-water system. In SPE Gas Technology Symposium.

Gundogan, O., Mackay, E., & Todd, A. (2011). Comparison of numerical codes for geochemical modelling of CO_2 storage in target sandstone reservoirs. Chemical Engineering Research and Design, 89(9), 1805-1816.

Gunter, W.D., Perkins, E.H., & Hutcheon, I.(2000). Aquifer disposal of acid gases: modelling of water–rock reactions for trapping of acid wastes. Appl. Geochem., 15(8), 1085–1095.

Gunter, W.D., Perkins, E.H., & McCann, T.J. (1993): Aquifer disposal of CO_2-rich gases: reaction design for added capacity. Energy Conversion and Management, 34, 941–948.

Gunter, W.D., Bachu, S., Law, D.H.-S., Marwaha, V., Drysdale, D.L., Macdonald, D.L., & McCann, T.J. (1996). Technical and economic feasibility of CO_2 disposal in aquifers within the Alberta sedimentary basin, Canada. Energy Conversion and Management, 37, 1135-1142

Gunter, W. D., Wiwchar, B., & Perkins, E. H. (1997), Aquifer Disposal of CO_2-rich Greenhouse Gases: Extension of the time scale of experiment for CO_2- sequestering reactions by geochemical modeling. Mineralogy and Petrology, 59, 121-140.

Hassanizadeh, S. M., & Gray, W. G. (1987). High velocity flow in porous media. Transport in Porous Media, 2(6), 521-531.

Haszeldine, R.S. (2009). “Carbon Capture and Storage: How Green Can Black Be?”. Science, 325,1647-1655..

Hayek, M., Mouche, E., & Mügler, C. (2009). Modeling vertical stratification of CO_2 injected into a deep layered aquifer. Advances in Water Resources, 32(3), 450-462.

Hitchon, B. (ed) (1996). Aquifer disposal of carbon dioxide: Hydrodynamics and mineral trapping - proof of concept. Geoscience Publishing Ltd., Alberta, Canada.

Hoffert, M.I., Wey, Y.C., Callegari, A.J., & Broecker, W.S. (1979). Atmospheric response to deep-sea injections of fossil-fuel carbondioxide. Climatic Change, 2(1), 53-68.

Holditch, S. A., & Morse, R. A. (1976). The Effects of Non-Darcy Flow on the Behavior of Hydraulically Fractured Gas Wells (includes associated paper 6417). Journal of Petroleum Technology, 28(10), 1169-1179.

Holloway, S. (2001). Storage of fossil fuel-derived carbon dioxide beneath the surface of the earth. Annual Review of Energy and the Environment, 26(1), 145-166.

Holloway, S., & Savage, D. (1993). The potential for aquifer disposal of carbon dioxide in the UK. Energy Conversion and Management, 34(9–11), 925–932. Kaarstad, O., 1992: Emission-free fossil energy from Norway. Energy Conversion and Management, 33(5–8), 619–626.

IEAGHG. (2011). Effects of Impurities on Geological Storage of CO_2. IEA Greenhouse Gas R&D Programme (IEAGHG).

Jacquemet, N., Le Gallo, Y., Estublier, A., Lachet, V., von Dalwigk, I., Yan, J., Azaroual, M., & Audigane, P. (2009). CO_2 streams containing associated components-A review of the thermodynamic and geochemical properties and assessment of some reactive transport codes. Energy Procedia, 1 (1), 3739–3746.

Jamiolahmady, M., Danesh, A., Sohrabi, M., & Duncan, D.B. (2006). Flow around a rock perforation surrounded by crushed zone: Experiments vs. Theory. Journal of Petroleum Science and Engineering, 50, (2), 102-114.

Janicek, J. D., & Katz, D. L. V. (1955). Applications of unsteady state gas flow calculations. Proc.,U. of Michigan Research Conference.

Joekar-Niasar, V., Hassanizadeh, S.M., & Leijnse A.(2008). Insights into the relationships among capillary pressure, saturation, interfacial area and relative permeability using pore-network modeling.Transport in Porous Media, 74, 201–219.

Johnson, J. W., Nitao, J. J., Steefel, C. I., & Knauss, K. G. (2001). Reactive transport modeling of geologic CO_2 sequestration in saline aquifers: The influence of intra-aquifer shales and the relative effectiveness of structural, solubility, and mineral trapping during prograde and retrograde sequestration. AGU Meeting Washington DC.

Johnson, J. W., Nitao, J. J., & Knauss, K. G. (2004). Reactive transport modeling of CO_2 storage in saline aquifers to elucidate fundamental processes, trapping mechanisms, and sequestration partitioning. In: Baines, S. J., Worden, R. H. (Eds.), Geologic Storage of Carbon Dioxide. Vol. 233. Geological Society Special Publications, London, UK. 107–128.

Jones, S.C. (1987). Using the Inertial Coefficient β To Characterize Heterogeneity on Reservoir Rock. Paper SPE 16949 prepared for presentation at the 62nd Annual Technical Conference and Exhibition of the SPE held in Dallas, Texas, 27-30 September.

Karimi-Fard, M., & Firoozabadi, A. (2003). Numerical simulation of water injection in 2D fractured media using discrete-fracture model, SPE Reservoir Eval. Eng., 4, 117– 126.

Kaszuba, P.J., Janecky, R.D., & Snow, G.M. (2003), Carbon dioxide reaction processes in a model brine aquifer at 200° C and 200 bars: Implications for geologic sequestration of carbon. Applied Geochemistry 18, 1065-1080.

Kaszuba, J.P., Janecky, D.R., & Snow, M.G. (2005). Experimental evaluation of mixed fluid reactions between supercritical carbon dioxide and NaCl brine: relevance to the integrity of a geologic carbon repository. Chemical Geology, 217 (3–4), 277–293.

Kather, A. (2009). Presented at 2nd Working Group Meeting on CO_2 Quality and Other Relevant Issues (September 2009, Cottbus, Germany).

Katz, D. L. & Lee, R. L. (1990). Natural Gas Engineering, Production and Storage, Chemical Engineering Series. New York: McGraw-Hill.

Kharaka, Y.K., Cole, D.R., Hovorka, S.D., Gunter, W.D., Knauss, K.G., & Freifeld, B.M. (2006). Gas–water–rock interactions in Frio Formation following CO_2 injection: implications for the storage of greenhouse gases in sedimentary basins. Geology, 34 (7), 577–580.

Kharaka, Y.K., Gunter, W.D., Aggarwal, P.K., Perkins, E.H. & DeBraal, J.D. (1988 SOLMNEQ.88). A computer program for geochemical modelling of water-rock reactions. United States Geological Survey, Water-Resources Investigations Report 88-4227.

Kheshgi, H.S., Flannery, B.P., Hoffert, M.I., & Lapenis, A.G. (1994). The effectiveness of marine CO_2 disposal. Energy, 19(9),967-975.

Klusman, R.W. (2003). Evaluation of leakage potential from a carbon dioxide EOR/sequestration project, Energy Conversion and Management, 44, 1921-1940.

Knauss, K.G., Johnson, J.W., & Steefel, C.I. (2005). Evaluation of the impact of CO_2, cocontaminant gas, aqueous fluid and reservoir rock interactions on the geologic sequestration of CO_2. Chem. Geol., 217 (3–4), 339–350.

Koide, H.G., Tazaki, Y., Noguchi, Y., Nakayama, S., Iijima, M., Ito, K., & Shindo, Y. (1992). Subterranean containment and long-term storage of carbon dioxide in unused aquifers and in depleted natural gas reservoirs. Energy Conversion and Management, 33(5–8), 619–626.

Korbol, R., & Kaddour, A. (1994). Sleipner West CO_2 disposal: injection of removed CO2 into the Utsira formation. Energy Conversion and Management, 36(6–9), 509–512.

Kühn, M., & Clauser, C. (2006). Mineralische Bindung von CO_2 bei der Speicherung im Untergrund in geothermischen Reservoiren (Mineral trapping of CO_2 in underground storage in geothermal reservoirs). Chemie Ingenieur Technik Special Issue: Kohlendioxid und Klimaschutz, 78, 425– 434.

Kusakabe, M., Komoda, Y., Takano, B., & Abiko, T.(2000). Sulfur isotopic effects in the disproportionation reaction of sulfur dioxide in hydrothermal fluids: implications for theδ34S variations of dissolved bisulfate and elemental sulfur from active crater lakes. J. Volcanol. Geotherm. Res., 97, 287–307.

Kutasov, I. M. (1993). Equation predicts non-Darcy flow coefficient. Oil and Gas Journal. (United States)., 91(11).

Kutchko, B.G., Strazisar, B.R., Dzombak, D.A., Lowry, G.V., & Thaulow, N.(2007). Degradation of well cement by CO_2 under geologic sequestration conditions. Environ. Sci. Technol., 41 (13), 4787–4792.

Law, D.H.S., & Bachu, S. (1996). Hydrogeological & numerical analysis of CO_2 disposal in deep aquifers in the Alberta Sedimentary Basin. Energy Conversion and Management., 37, 1167-1174.

Lasaga, A.C. (1998). Kinetic Theory in the Earth Sciences. Princeton University Press, Princeton.

Lasaga, A.C., Soler, J.M., Ganor, J., Burch, T.E., & Nagy, K.L.(1994). Chemical weathering rate laws and global geochemical cycles. Geochim. Cosmochim. Acta, 58, 2361–2386.

Lasseux, D., Ahmadi, A., & Arani, A. A. A. (2008). Two-phase inertial flow in homogeneous porous media: A theoretical derivation of a macroscopic model.Transport in porous media, 75(3), 371-400.

Lee, R. L., Logan, R. W., & Tek, M. R. (1987).Effects of turbulence on transient flow of real gas through porous media. SPE Formation Evaluation, 108–120.

Le Gallo, Y., Bildstein, O., & Brosse, E. (1998). Coupled reaction-flow modeling of diagenetic changes in reservoir permeability, porosity, and mineral compositions. Journal of Hydrology, 209, 366–388.

Li, D., & Engler, T.W. (2001). Literature review on correlations of the non-Darcy coefficient. SPE paper 70015.

Li, L., Peters, C.A., & Celia, M.A.(2006). Upscaling geochemical reaction rates using porescale network modeling. Adv. Water Resour., 29, 1351–1370.

Lindeberg, E., & Wessel-Berg, D. (1997). Vertical convection in an aquifer under a gas cap of CO_2. Energy Conversion and Management, 38, 5229-5234.

Liu, X., Civian, F., & Evans, R.D. (1995). Correlation of the Non-Darcy Flow Coefficient. Journal of Canadian Petroleum Technology, 34, (10), 50-54.

Liu, L., Suto, Y., Bignall, G., Yamasaki, N., & Hashida, T. (2003). CO_2 injection to granite and sandstone in experimental rock/hot water systems. Energy Conversion and Management., 44, 1399-1410.

Lopez-Hernandez H.D., Valko P.P., & Pham T.T. (2004). Optimum Fracture Treatment Design Minimizes the Impact of Non-Darcy Flow Effects. 2004 SPE Annual Technical Conference and Exhibition, Houston.

Ma, H., & Ruth, D. W. (1993). The microscopic analysis of high Forchheimer number flow in porous media. Transport Porous Media, 13, 139–160.

Macdonald, I. F., El-Sayed, M. S., Mow, K., & Dullien, F. A. L. (1979). Flow through porous media-the Ergun equation revisited. Industrial & Engineering Chemistry Fundamentals. 18(3), 199-208.

Magro, G., & Pennisi, M. (1991). Light noble gases and nitrogen in the crater fluids at vulcano (Italy): special survey from June to September 1988. Acta Vulcanologica, 1, 215–218.

Marchetti, C. (1977). On Geoengineering and the CO_2 Problem.Climatic Change, 1, 59–68.

Martins, J. P., Milton-Tayler, D., & Leung, H. K. (1990, September). The effects of non-Darcy flow in propped hydraulic fractures. In SPE Annual Technical Conference and Exhibition.

Mazumder, S., Van Hemert, P., Bruining, J., Wolf, K. H., & Drabe, K. (2006). In situ CO2 coal reactions in view of carbon dioxide storage in deep unminable coal seams. Fuel, 85(12), 1904-1912.

McKinsey, & Company. (2008).Carbon Capture and Storage: Assessing the Economics. McKinsey Climate Change Initiative.

McPherson, B. J. O. L., & Cole, B. S. (2000). Multiphase CO_2 flow, transport and sequestration in the Powder River Basin, Wyoming, U.S.A., Journal of Geochemical Exploration, 69, 65-69.

McPherson, B. O. L. J., & Cole, B. S. (submitted for publication-2005). An equation-of state for multiphase flow of CO_2 and water in deep sedimentary basin conditions.

McPherson, B. J. O. L., & Lichtner, P. C. (2001). CO_2 sequestration in deep aquifers. In: Proceeding of the 1st National Conference on Carbon Sequestration, Washington DC, USA.

Metz, B., Davidson, O., De Coninck, H., Loos, M., & Meyer, L. (2005). IPCC special report on carbon dioxide capture and storage. Intergovernmental Panel on Climate Change, Geneva (Switzerland). Working Group III.

Mijic, A., & LaForce, T.C. (2010). Effects of Non-Darcy Flow in CO_2 Injection into Saline Aquifers.12 European Conference on the Mathematics of Oil Recovery, Sept.06.

Mito, S., Xue, Z., & Ohsumi, T. (2008). Case study of geochemical reactions at the Nagaoka CO_2 injection site, Japan. International Journal of Greenhouse Gas Control, 2, 309–318.

Nitao, J. J. (1995). Reference manual for the NUFT flow and transport code. Lawrence Livermore National Laboratory, Livermore, California, USA, 1st Edition, Report UCRL-ID-113520.

Nordbotten, J.M., Celia, M.A., Bachu, S., & Dahle, H.K.(2005). Semianalytical solution for CO_2 leakage through an abandoned well. Environ. Sci. Technol., 39, 602–611.

Okuyama, Y., Todaka, N., Sasaki, M., Ajima, S., & Akasaka, C. (2012). Reactive transport simulation study of geochemical CO_2 trapping on the Tokyo Bay model–with focus on the behavior of dawsonite. Applied Geochemistry.

Oldenburg, C. M., & Rinaldi, A. P. (2011). Buoyancy effects on upward brine displacement caused by CO_2 injection. Transport in porous media, 87(2), 525-540.

Oosterkamp, A., & Ramsen, J. (2008). State-of-the-art overview of CO_2 pipeline transport with relevance to offshore pipelines. Polytech Report No: POL-O-2007-138-A.

Palandri, J., & Kharaka, Y.K.(2004). A compilation of rate parameters of water–mineral interaction kinetics for application to geochemical modeling. US Geol. Surv. Open File Report 2004-1068. 64 .

Palandri, J.L., & Kharaka, Y.K. (2005). Ferric iron-bearing sediments as a mineral trap for CO_2 sequestration: Iron reduction using sulfur-bearing waste gas. Chemical Geology, 217 (3–4), 351–364.

Parfomak, P.W., & Folger, P. (2008). CRS Report for Congress: Carbon Dioxide (CO_2) Pipelines for Carbon Sequestration: Emerging Policy Issues. Congressional Research Service.

Parkhurst, D. L. (1995). User's guide to PHREEQC, a computermodel for speciation, reaction-path, advective-transport and inverse geochemical calculations. US Geological Survey Water-Resources Investigations Report 95–4227.

Pascal, H., Quillian, R.G., & Kingston, J. (1980). Analysis of Vertical Fracture Length and Non-Darcy Floe Coefficient Using Variable Rate Tests. Paper SPE 9438 presented at the SPE Annual Technical Conference and Exhibition, Dallas, September 21-24.

Peters, C.A. (2009). Accessibilities of reactive minerals in consolidated sedimentary rock: an imaging study of three sandstones. Chem. Geol., 265 (1–2), 198–208.

Polubarinova-Kochina, P.Y. (1952). Theory of Ground Water Motion, Goss. Izdat. Tekh.-Teoret. Lit., Moscow, 676.

Prausnitz, J. M., Lichtenthaler, R. N., & de Azevedo, E. G. (1986).Molecular Thermodynamics of Fluid-Phase Equilibria, 2nd ed.; Prentice-Hall, Inc.: Eaglewood Cliffs, NJ.

Pruess, K. (1991). TOUGH2: a general numerical for multiphase fluid and heat flow. Tech. Rep. LBL- 29400, Lawrence Berkeley Laboratory, Berkeley, California, USA.

Pruess, K. (2009). Formation dry-out from CO_2 injection into saline aquifers: 2. analytical model for salt precipitation. Water Resources Research, 45 (3), art. no. W03403.

Pruess, K., & Garcia, J. (2002). Multiphase flow dynamics during CO_2 disposal into saline aquifers, Environmental Geology, 42, 282-295.

Pruess, K., & Müller, N. (2009). Formation dry-out from CO_2 injection into saline aquifers: 1. effects of solids precipitation and their mitigation. Water Resources Research, 45 (3), art. no. W03402.

Ramey, H. J. (1965). Non-Darcy flow and wellbore storage effects in pressure build-up and drawdown of gas wells. Journal of Petroleum Technology, 17(2), 223-233.

Ranz, W. E., & Marshall, W. R. (1952). Evaporation from drops. Chem. Eng. Prog., 48(3), 141-146.

Rubin, J. (1983). Transport of reacting solutes in porousmedia, relationship between mathematical nature of problem formulation and chemical nature of reactions. Water Resources Research, 19, 1231–1252.

Saripalli, P., & McGrail, B.P. (2002). Semi-analytical approaches to modeling deep well injection of CO_2 for geological sequestration, Energy Conversion and Management, 43(2), 185-198.

Sass, B.M., Farzan, H., Prabhakar, R., Gerst, J., Sminchak, J., Bhargava, M., Nestleroth, B., & Figueroa, J. (2009). Considerations for treating impurities in oxy-combustion flue gas prior to sequestration. Energy Procedia, 1 (1), 535–542.

Scheidegger, A.E. (1953). Theoretical Models of Porous Matter, Producers Monthly, August, 17-23.

Scheidegger, A. E. (1972).The Physics of Flow through Porous Media. University of Toronto Press.

Scheidegger, A.E. ed. (1974). The Physics of Flow through Porous Media, University of Toronto Press.

Schmidt, W. (2004). Influence of Multidimensionality and Interfacial Friction on the Coolability of Fragmented Corium. PhD thesis, University of Stuttgart, May.

Seevam, P.N., Race, J.M., & Downie, M.J. (2007). Carbon dioxide pipelines for sequestration in the UK: An engineering gap analysis. Global Pipeline Monthly, 3 (6).

Seguin, D., Montillet, A., & Comiti, J. (1998). Experimental characterisation of flow regimes in various porous media—I: Limit of laminar flow regime. Chemical engineering science, 53(21), 3751-3761.

Seguin, D., Montillet, A., Comiti, J., & Huet, F. (1998). Experimental characterization of flow regimes in various porous media—II: Transition to turbulent regime. Chemical engineering science, 53(22), 3897-3909.

Shao, H., Ray, J. R., & Jun, Y. S. (2010). Dissolution and precipitation of clay minerals under geologic CO_2 sequestration conditions: CO_2-brine-phlogopite interactions. Environmental science & technology, 44(15), 5999-6005.

Shaw, J., & Bachu, S. (2002). Screening, evaluation, and ranking of oil reservoirs suitable for CO_2-flood EOR and carbon dioxide sequestration. Journal of Canadian Petroleum Technology, 41(9).

Shindo, Y., Fujioka, Y., Takeuchi, K., & Komiyama, H. (1995). Kinetics on the of CO_2 into water from the surface of CO_2 hydrate at high pressure.International journal of chemical kinetics, 27(6), 569-575.

Shukla, R., Ranjith, P., Haque, A., & Choi, X. (1961). “A review of studies on CO_2 sequestration and caprock integrity”. Fuel, 2010. 89(10): p. 2651-2664.

Smith, R. V. . 1565-G-Unsteady-State Gas Flow into Gas Wells. Journal of Petroleum Technology, 13(11), 1151-1159.

Smith, J.M. (1970). Chemical Engineering Kinetics, 2nd ed. McGraw-Hill, New York, 411-412.

Sobieski, W., & Trykozko, A. (2012).Darcy and Forchheimer laws in experimental and simulation studies of flow through porous media. Transport in Porous Media (submitted).

Spycher, N., Pruess, K., & Ennis-King, J. (2003), CO_2-H_2O Mixtures in the Geological Sequestration of CO_2. I. Assessment and Calculation of Mutual Solubilities from 12 to 100o C and up to 600 bar. Geochimica et Cosmochimica Acta, (67) 16, 3015-3031.

Spycher, N.F., & Reed, M.H. (1988) Fugacity coefficients of H_2, CO_2, CH_4, H_2O and of H_2O-CO_2-CH_4 mixtures: a virial equation treatment for moderate pressures and temperatures applicable to calculations of hydrothermal boiling. Geochim Cosmochim Acta, 52,739–749

Steefel, C.I., & Lasaga, A.C.(1994). A coupled model for transport of multiple chemical species and kinetic precipitation/ reactions with applications to reactive flow in single phase hydrothermal system. Am. J. Sci., 294, 529–592.

Su, H. (2004). A Three-Phase Non-Darcy Flow Formulation in Reservoir Simulation. In SPE Asia Pacific Oil and Gas Conference and Exhibition.

Swift, G. W., & Kiel, O. G. (1962). The prediction of gas-well performance including the effects of non-Darcy flow. J. Petrol. Technol. Trans. AIME, 222, 791–798.

Tarakad, R. R., & Danner, R. P. (1977). Improved corresponding states method for polar fluids – correlation of 2nd virial-coefficients. AIChE J., 23 (5), 685–695.

Tek, M. R., Coats, K. H., & Katz, D. L. (1962). The effects of turbulence on flow of natural gas through porous reservoirs. J. Petrol. Technol. Trans. AIME, 222, 799–806.

Thauvin, F., & Mohanty, K.K. (1998). Network Modeling of Non-Darcy Flow through Porous Media, Transport in Porous Media, 31, 19-37.

Thomas, M. W., Stewart, M., Trotz, M., & Cunningham, J. A. (2012). Geochemical modeling of CO_2 sequestration in deep, saline, dolomitic-limestone aquifers: Critical evaluation of thermodynamic sub-models.Chemical Geology, 306, 29-39.

Xu, T., Apps. J.A., & Pruess, K. (2003). Reactive geochemical transport simulation to study mineral trapping for CO_2 disposal in deep arenaceous formations. Journal of Geophysical Research, 108 B2, 2071.

Xu, T., Apps, J., & Pruess, K.(2004a). Numerical simulation of CO_2 disposal by mineral trapping in deep aquifers. Appl. Geochem., 19, 917–936.

Xu, T., Apps, J.A., Pruess, K., & Yamamoto, H. (2007). Numerical modeling of injection and mineral trapping of CO_2 with H_2S and SO_2 in a sandstone formation. Chemical Geology, 242 (3–4), 319–346.

Xu, T., & Pruess, K. (1998). Coupled modeling of non-isothermal multiphase flow, solute transport and reactive chemistry in porous and fractured media: 1. model development and validation. Tech. Rep. LBNL-42050, Lawrence Berkeley National Laboratory, Berkeley, California, USA.

Xu, T., & Pruess, K. (2001a). On fluid flow and mineral alteration in fractured caprock of magmatic hydrothermal systems. Journal of Geophysical Research, 106, 2121–2138.

Xu, T., Sonnenthal, E., Spycher, N., Pruess, K., Brimhall, G., & Apps, J. (2001b). Modeling multiphase non-isothermal fluid flow and reactive geochemical transport in variably saturated fractured rocks: 2. applications to supergene copper enrichment and hydrothermal flows, American Journal of Science, 301, 34–59.

Xu, T., Sonnenthal, E., Spycher, N., & Pruess, K. (2004b). TOUGHREACT user's guide: A simulation program for non-isothermal multiphase reactive geochemical transport in variably saturated geologic media. Earth Sciences Division, Lawrence Berkeley National Laboratory, University of California, Berkeley, CA

Yazdchi, K., Srivastava, S., & Luding, S. (2010). On the transition from creeping to inertial flow in arrays of cylinders.

USEPA. (2009). U.S. Environmental Protection Agency Acid Rain and Related Programs 2007 Progress Report. EPA: Washington, DC.

Wahyudi, I., Montillet, A., & Khalifa, A.O.A. (2000). Darcy and post-Darcy flows within different sands. J. Hydraul. Res., 40(4), 519–525

Welge, H. J. (1952).A simplified method for computing oil recovery by gas or water drive. Trans. Am. Inst. Min. Metall. Petrol. Eng., 195, 91–98

Wertz, F., Gherardi, F., Blanc, P., Bader, A. G., & Fabbri, A. (2012). Modeling CO_2-driven cement alteration at well-caprock interface. In Submitted to TOUGH Symposium.

White, S. P. (1995). Multiphase non-isothermal transport of systems of reacting chemicals. Water Resources Research, 31, 1761–1772.

Winter, E.M., & Bergman, P.D. (1993). Availability of depleted oil and gas reservoirs for disposal of carbon dioxide in the United States. Energy Conversion and Management, 34(9–11), 1177–1187.

White, S. P., Weir, G. J., & Kissling, W. M. (2001). Numerical simulation of CO_2 sequestration in natural CO_2 reservoirs on the Colorado plateau. In: Proceeding of the 1st National Conference on Carbon Sequestration, Washington DC, USA.

Whitney, D. D. (1988).Characterization of the non-Darcy flow coefficient in propped hydraulic fractures. Master's thesis, University of Oklahoma.

Wong, S. (1970). Effect of liquid saturation on turbulence factors for gas-liquid systems. Journal of Canadian Petroleum Technology, 9(4).

Worden, R. H. (2006). Dawsonite cement in the Triassic Lam formation, Shabwa basin, Yemen: a natural analogue for a potential mineral product of subsurface CO_2 storage for greenhouse gas reduction. Marine and Petroleum Geology, 23, 61–77.

Wu, Y. S. (2001). Non-Darcy displacement of immiscible fluids in porous media. Water Resources Research, 37(12), 2943–2950.

Wu, Y.S. (2002). Numerical simulation of single-phase and multiphase non-Darcy flow in porous and fractured reservoirs. Transport in Porous Media, 49, 209–240.

Wu, Y. S., Lai, B., Miskimins, J. L., Fakcharoenphol, P., & Di, Y. (2011). Analysis of multiphase non-Darcy flow in porous media. Transport in Porous Media, 88(2), 205-223.

Zeng, Z.W., & Grigg, R. (2006).A criterion for non-Darcy flow in porous media. Transport in Porous Media, 63, 57–69.

Zerai, B., Saylor, B. Z., & Matisoff, G. (2006). Computer simulation of CO_2 trapped through mineral precipitation in the Rose Run sandstone, Ohio. Applied Geochemistry 21, 223–240.

Zhang, A., & Aral, M. (2013). Effect of Two-phase Darcy-Forchheimer Flow Condition on CO_2 Injection into Deep Saline Aquifers. Journal of Contaminant Hydrology. (Submitted).

Zhang, J., & Xing, H. (2012).Numerical modeling of non-Darcy flow in near-well region of a geothermal reservoir. Geothermics, 42, 78-86.